Submillimeter Surveys of Galaxy Samples

Thesis by

Min Yang

In Partial Fulfillment of the Requirements
for the Degree of
Doctor of Philosophy

1891

California Institute of Technology
Pasadena, California

2006
(Defended July 31, 2006)

For my parents.

Acknowledgements

I would like to take this opportunity to express my deep gratitude for the influence and support from family, friends, colleagues and mentors. My special thanks go to Tom Phillips.

Abstract

This thesis aims to gain a better understanding of dusty galaxies by studying the thermal emission of interstellar dust at submillimeter (submm) wavelengths. We conduct 350 $\mu\mathrm{m}$ observations of two galaxy samples selected based on entirely different criteria, using the Submillimeter High Angular Resolution Camera II (SHARC-II, Dowell et al. 2003) at the 10.4 m Caltech Submillimeter Observatory (CSO).

The first galaxy sample consists of 18 luminous infrared galaxies (LIGs) in the local Universe ($0.003 \leq z \leq 0.042$). We estimate the global properties in this galaxy sample; dust temperature ($\mathrm{T_d} = 38.6 \pm 7.7\,\mathrm{K}$), emissivity index ($\beta = 1.6 \pm 0.3$), far-infrared (FIR) luminosity ($\mathrm{L_{fir}} = 10^{\,11.2\pm0.6}\,\mathrm{L_\odot}$) and dust mass ($\mathrm{M_d} = 10^{\,7.4\pm0.6}\,\mathrm{M_\odot}$). Guided by theoretical considerations and laboratory measurements, we derive a $\mathrm{T_d}$ -β inverse correlation for the local LIG sample; $\mathrm{T_d} = [5.03 \times 10^9]^{\,\frac{1}{4.46+\beta}}$.

The second galaxy sample consists of 36 ultraluminous infrared galaxies (ULIGs) at moderate redshifts ($0.1 < z < 1.0$), out of which 28 galaxies are detected. The newly acquired 350 $\mu\mathrm{m}$ data, in combination with the pre-existing IRAS 60 $\mu\mathrm{m}$ and 100 $\mu\mathrm{m}$ data, leads to meaningful estimates of the global properties in these galaxies for the first time; $\mathrm{T_d} = 40.9 \pm 6.9\,\mathrm{K}$, $\mathrm{L_{fir}} = 10^{\,12.2\pm0.5}\,\mathrm{L_\odot}$, $\mathrm{M_d} = 10^{\,8.3\pm0.3}\,\mathrm{M_\odot}$ and intense starburst activity ($\mathrm{SFR} = 10^{\,2.5\pm0.5}\,\mathrm{L_\odot\,yr^{-1}}$). There is strong circumstantial evidence that the $\mathrm{T_d}$ -β inverse correlation observed in the local LIG sample remains valid in ULIGs at moderate redshifts. We find that the FIR-radio correlation observed in local star-forming galaxies continues to hold for ULIGs over the redshift range of $0.1 < z < 1.0$ and dust heating originates predominantly from star formation. $\mathrm{L_{fir}}$ and $\mathrm{T_d}$ derived for dusty galaxy samples over a wide range of redshifts show significant scatter, due to differing selection biases and variations in dust mass and grain properties. We argue that the observed T_d, as a large-scale SED parameter, is linked to the global star formation efficiency (SFE) and the spatial extent characteristic of dominant star formation in a galaxy.

Contents

List of Figures

List of Tables

Chapter 1

Introduction

1.1 Scientific Motivation

Interstellar dust grains are small particles that sparsely populate throughout the interstellar medium (ISM). Although interstellar dust accounts for only a very small fraction of the total mass in a galaxy, it plays critical roles in galaxy formation and evolution. Dust grains absorb strongly in the ultraviolet (UV) and optical, leading to a significant fraction of stellar radiation within a galaxy being absorbed. The warm grains subsequently emit strongly in the FIR/submm, effectively down-converting the electromagnetic energy in various astrophysical environments.

The FIR luminosity $\mathrm{L_{fir}}$, integrated over the wavelength range 40 μm - 1000 μm , originates from dust heated by massive, short-lived stellar populations and is an indirect but natural candidate for tracing the instantaneous star formation rates (SFRs) in galaxies. Kennicutt (1998) has established the following conversion factor

$$\frac{\mathrm{SFR}}{\mathrm{M_\odot\ yr^{-1}}} = 1.7 \times \frac{\mathrm{L_{ir}}}{10^{10}\ \mathrm{L_\odot}}\,, \tag{1.1}$$

where $\mathrm{L_{ir}}$ is integrated over the full infrared (IR) and submm wavelength range of 8 μm - 1000 μm . The FIR emission complements the other two commonly used star formation tracers - UV continuum emission and optical/near-infrared (NIR) recombination line emission (e.g., Hα) - both of which are directly linked to photospheric emission of young stellar populations. All three of these star formation tracers are sensitive to the initial mass function (IMF), while the FIR luminosity as a probe of star formation activity has its own unique advantages and limitations.

One very attractive property of the FIR emission is that it suffers relatively modest extinction, a factor which often introduces the most significant uncertainties in SFRs derived using the other two techniques (Calzetti 2001). In fact, in regions of extremely high gas and dust densities and SFRs, where UV and optical emission is inconsequential, dust emission provides the only viable route. The other advantage is associated with the so-called "negative" K-correction at FIR/submm wavelengths when the increase in rest-frame flux density is enough to compensate for the dimming effect from increasing luminosity distance over a wide range of redshifts. The K-correction, defined as the difference in absolute magnitude in observed-frame versus that in the rest-frame for a source at redshift $z > 0$ (Hogg et al. 2002), is a function of wavelength and redshift, specific to the rest-frame spectral energy distribution (SED) shape. The effect of the K-correction at FIR/submm wavelengths makes FIR/submm observations unique and powerful in look-back studies of star formation in the distant universe.

However, ambiguities can arise when dust emission is used to infer SFRs. Older stars and/or active galactic nuclei (AGNs) can provide additional dust heating, thereby enhancing the FIR luminosity beyond that proportional to the ongoing SFR. However, observational evidence shows that the FIR luminosities in star-forming galaxies generally correlate very well with other SFR tracers except in some early-type galaxies and obvious AGN hosts (Kennicutt 1998). Perhaps the more impressive observational evidence, lending strong support to the general validity of FIR luminosity as a tracer of SFR, is the very tight FIR-radio correlation universally observed in local star forming galaxies (Condon 1992). Helou et al. (1985) define a logarithmic measure of the FIR/radio flux ratio - q - as

$$q \equiv \log\left(\frac{\mathrm{F_{fir}}}{3.75\times10^{12}\,\mathrm{W\,m^{-2}}}\right) - \log\left(\frac{\mathrm{S_{1.4GHz}}}{\mathrm{W\,m^{-2}\,Hz^{-1}}}\right), \tag{1.2}$$

where $\mathrm{F_{fir}}$ is the integrated flux over 40 μm - 120 μm , and q is found to be bounded within a narrow range with median $\langle q\rangle \sim 2.3$ and scatter $\sigma_q \leq 0.2$ for a large number of low-redshift galaxies spanning 4 orders of magnitude in FIR luminosity. This is explained by the fact that radio emission at $1.4\,\mathrm{GHz}$ is thought to arise mainly from nonthermal synchrotron emission of cosmic-ray particles that are released by supernovae explosions of massive young stars, thus radio emission is expected to be proportional to the present star formation rate, as is FIR emission.

The effectiveness of using dust emission as a tracer of SFR can be limited by the coarse angular resolution allowed by instrumentation currently working in the FIR/submm. This prevents detailed studies of star formation by the method of FIR/submm observation, hampers identification of weak FIR/submm sources, and limits the depth achievable in deep FIR/submm surveys due to "confusion noise". Chapman et al. (2004a), assuming the local FIR-radio correlation to be universally true across wide ranges in properties of luminous dusty galaxies and redshift, circumvent this challenge and take advantage of the sub-arcsec angular resolution available from radio interferometry. The discussion presented in this and the preceding paragraph, in turn, demonstrates that it is extremely important to test the FIR-radio correlation in galaxy populations with different global characteristics as well as at different redshifts.

LIGs ($\log(\mathrm{L_{ir}}/\mathrm{L_\odot}) \geq 11$) are objects that predominantly radiate in the IR. They are dust shrouded objects where extinction and re-radiation by dust lead to high IR-to-optical flux ratios. They were first discovered in large numbers in the local universe by the Infrared Astronomy Satellite (IRAS), launched in 1983. The all-sky IRAS surveys at $12\,\mu\mathrm{m}$, $25\,\mu\mathrm{m}$, $60\,\mu\mathrm{m}$ and $100\,\mu\mathrm{m}$ wavebands revealed the role of IR emission as an important contributor to energy budgets in many star forming galaxies (Soifer et al. 1986, Soifer et al. 1987).

Observations of IRAS-detected LIGs and ULIGs ($\log(\mathrm{L_{ir}}/\mathrm{L_\odot}) \geq 12$) have shown they tend to be associated with interacting or merging gas-rich disks; in fact, the fraction of strongly interacting/merging systems increases from $\sim 10\%$ at $\log(\mathrm{L_{ir}}/\mathrm{L_\odot}) = 10.5 - 11$ to $\sim\ 100\%$ for ULIGs (Sanders & Mirabel 1996). From Eq. (1.1), high FIR luminosities in the LIGs and ULIGs indicate extreme star formation activities in these objects, with implied SFRs ranging from $\sim 20\,\mathrm{M_\odot\,yr^{-1}}$ all the way up to $\sim 1000\,\mathrm{M_\odot\,yr^{-1}}$. Furthermore, high-resolution observations of nearby LIGs and ULIGs reveal that the bulk of the energy output and the molecular gas in these objects is concentrated in compact, central regions of a typical scale on the order of $0.1 \sim 1\,\mathrm{kpc}$ (Sanders & Mirabel 1996, Young & Scoville 1991). The collective observational information is no coincidence - the extreme concentration of gas and dust and the enormous gas fueling as physically required by such high SFRs, in the large-scale, can only be made possible by strong tidal interactions and mergers.

Numerous studies have also been carried out aiming to identify the nature of the dominant power source in LIGs and ULIGs - star formation or dust-shrouded AGNs. Genzel et al. (1998) have constructed diagnostic diagrams in the mid-infrared (MIR) to distinguish between these two possibilities. Such MIR diagnostic diagrams are inspired by the distinct MIR spectral characteristics for star-forming regions and AGNs - starbursts often show low-excitation fine-structure lines and prominent polycyclic aromatic hydrocarbon (PAH) features, while AGNs usually display high-excitation fine-structure lines with weak or no PAH features. MIR studies of large samples of IRAS selected LIGs and ULIGs (Genzel et al. 2000) have shown that local LIGs and ULIGs are composite objects, with star formation generally dominating the energy output, accounting for $\geq 70\%$ of the FIR luminosity. However, AGN contribution and dominance increases in more active galaxies that display warmer dust temperatures and higher FIR luminosities; in fact, the fraction of AGN-dominated galaxies increase from $\sim 15\%$ for ULIGs with $\mathrm{L_{IR}} = 2 \times 10^{12}\,\mathrm{L_\odot}$ to up to 50% at the highest FIR luminosity.

Although IRAS observations did not reach the high-redshift universe, its groundbreaking discoveries raised critical questions concerning evolution of the unique and often extreme LIG/ULIG galaxy population over cosmic time scales, and consequently motivated numerous follow-up observations of LIG/ULIG galaxy samples and cosmological surveys at multiple wavelengths, from the IR to the submm to the millimeter (mm).

The Cosmic IR Background (CIB), peaking at $150\,\mu\mathrm{m}$, is defined as the cosmic background (CB) at wavelengths longward of its minimum at $5\,\mu\mathrm{m}$. The first detection of CIB in 1996 using Cosmic Background Explorer (COBE) data (Puget et al. 1996, Hauser et al. 1998) and subsequent CIB observations have revealed that the CB emits power in the IR comparable to that in the optical, and the long-wavelength part of the CIB varies as $\mathrm{CIB}_\nu \propto \nu^{1.4}$, much flatter than the $\mathrm{S}_\nu \propto \nu^{2+\beta}$ slope in the FIR/submm spectra of individual dusty galaxies, where β is the FIR/submm emissivity index and is expected to have theoretical values of 1 or 2 (see § 2.3). Given that LIGs and ULIGs do not dominate the energy output in the local universe, the direct cosmological implications of the observed CIB spectral properties are startling - LIGs and ULIGs evolve much faster with redshift than optically selected galaxies and they increasingly dominate energy output at higher redshifts.

As can be expected, the dusty LIG/ULIG population can easily be missed by optical observations. On the other hand, a large number of high-redshift star forming galaxies have recently been detected based on optical observations, through applications of the so-called “Lyman Break” technique (Steidel et al. 1996). This technique detects the strong neutral atomic hydrogen absorption at rest-frame wavelength $912\,\mathrm{nm}$ as it passes through several broad-band filters in the optical. Many FIR/submm follow-up observations of these Lyman break galaxies (LBGs) have shown they are extremely weak IR sources. All this points to the conclusion that IR selected galaxies and optically selected galaxies are distinct populations. Studies of these two populations are therefore complementary and necessary for reaching a complete census of star formation activities in galaxies.

Blank field surveys at various IR/submm/mm wavelengths constitute an important component for investigating the cosmological evolution of the LIG/ULIG population. Such surveys conducted at distinct wavebands probe the production of IR energy in distinct redshift ranges, owing to the systematic shift in the K-correction with wavelength in the FIR/submm given a rest-frame SED. However, assumptions often have to be made about the rest-frame FIR/submm SED template in LIGs and ULIGs in order to interpret results from various single wavelength surveys, such as to infer the integrated IR luminosity and to investigate various selection biases that are often inherent to these surveys.

As important as it is, the question concerning FIR/submm SEDs remains open despite much work and progress in recent years (Blain et al. 2003). Adequate sampling of the SED at frequencies close to, below, and above the SED peak is essential for achieving accurate estimates of SED properties such as dust temperature T_d , emissivity index β and FIR luminosity L_{fir} . While all four IRAS wavebands are either near or above typical FIR/submm peak frequencies, photometric databases for the LIG/ULIG population at lower frequencies (in the submm/mm) remain relatively scarce and limited. Thanks to dedicated multi-wavelength observational efforts, a large number of LIGs and ULIGs now have sufficient frequency sampling in the FIR/submm. The subsequent SED modeling of these objects reveals that SEDs in the LIG/ULIG population are far from uniform, which in turn highlights the necessity of studying galaxy samples based on different selection criteria. This, as well as the determination of LIG/ULIG SEDs across distinct redshift ranges, are evidently of critical importance for building a complete inventory of SED templates for the LIG/ULIG population.

In summary, interstellar dust emission in the FIR/submm often constitutes an important, if not dominant, component of the total bolometric luminosity L_{bol} in many star forming galaxies. FIR emission is generally an effective tracer of star formation activities, and is particularly well suited for probing regions of high density and at great cosmological distance. LIGs and ULIGs, defined by their high IR luminosities, are dusty objects found to be in the phase of strong galaxy merging and interaction, accompanied by the induced coincidence of intense starbursts and AGNs. The LIG/ULIG population - naturally complementary to optically selected galaxies - is also known to exhibit very strong cosmological evolution, growing increasingly dominant in the distant Universe. In addition, observational evidence has led to speculations about possible evolutionary links between LIGs/ULIGs and other cosmologically interesting galaxies, such as giant ellipticals, LBGs, and quasi-stellar objects (QSOs). All this provides us with strong motivation to conduct detailed and extensive studies of this unique population, aiming to achieve unbiased understanding of their properties and gather useful insight concerning star formation, galaxy formation and evolution.

1.2 Technical Aspects

The technology required by observations at FIR and submm wavelengths developed relatively late as compared to other branches of astronomy. This is attributed to several technical challenges that are inherent to the FIR/submm spectral range.

First, the Earth's atmosphere emits and absorbs strongly at FIR/submm wavelengths, allowing very few open windows for FIR/submm ground observations and giving a background power which limits detector sensitivity. Space telescopes (e.g., IRAS, the Infrared Space Observatory - ISO, the Spitzer Space Telescope - Spitzer) offer the possibility of avoiding this problem but enormous effort is required in order to build and launch space telescopes with sufficiently large aperture sizes, and keep the detectors cooled at very low temperature for extended periods of time.

Second, semiconducting photo detectors, as used in the optical/NIR, are not suitable for detecting FIR/submm photons because the energy possessed by these photons is low compared to energy gaps in semiconductors. Instead, bolometer detectors with sensitivities near the atmospheric background limit (e.g., SHARC-II, SCUBA, MAMBO) have been adopted for FIR/submm flux measurements. Bolometers are devices that change temperatures when subject to incident radiation; in addition, their electrical resistances are temperature dependent. Incident radiation therefore induces changes in voltage when constant bias currents are applied. Such changes in voltage can subsequently be measured, recorded and converted to flux density of the incident field. The necessity of achieving extremely low intrinsic noise means that bolometer detectors have to be cooled to sub-Kelvin temperatures.

Third, long wavelengths work against angular resolution, given a fixed aperture size, as understood by the relation $\theta \sim 1.22\,\frac{\lambda}{\mathrm{D}}$. Even the state-of-the-art $10\,\mathrm{m}$ class telescopes (e.g., the $10.4\,\mathrm{m}$ CSO, the $15\,\mathrm{m}$ James Clerk Maxwell Telescope - JCMT, the $30\,\mathrm{m}$ IRAM telescope) are far from achieving the sub-arc resolution often enjoyed by optical and radio observations. Interferometers with $100\,\mathrm{m}$ baseline (e.g., the Submillimeter Array - SMA) can significantly improve the angular resolution, but the feasibility is limited by availability of compatible facilities. Related to the coarse angular resolution, "confusion noise" arises from emission from faint sources within the beam that can not be resolved individually.

1.3 Interstellar Dust Model

Interstellar dust grains are found in a wide range of astronomical environments, in circumstellar shells, novae and nebulae, HI and HII regions, molecular clouds and particularly in regions of active star formation. The existence of interstellar dust was first inferred by the attenuating and reddening effect it has on optical observations (Trumpler 1930), and the interaction of dust grains with starlight provided insight into their properties.

The wavelength dependence of interstellar extinction - "interstellar extinction curve" - shows that the dust grains preferentially absorb and scatter UV and optical radiation (Seaton 1979, Fitzpatrick 1986), suggesting significant presence of grains with $a \sim 0.1\,\mu\mathrm{m}$. The steep increase in extinction in the far-ultraviolet (FUV; $\lambda \sim 1000\,\mathrm{\AA}$) reveals the existence of very small grains with $a \sim 100\,\mathrm{\AA}$.

Non-spherical grains exert differential extinction on the different alignments of the incident electric vectors. Starlight can thereby be linearly polarized by non-spherical grains that are aligned by a number of plausible alignment mechanisms (Draine 2002). Polarization tends to peak at optical wavelengths ($\lambda \sim 5000\,\mathrm{\AA}$), indicating presence of grains with $a \sim 0.1\,\mu\mathrm{m}$ that are non-spherical and substantially aligned. The drop in polarization at the UV suggests that grains with $a \sim 100\,\mathrm{\AA}$ that dominate extinction at UV are either spherical or minimally aligned.

The extinction and polarization curves indicate a broad range of grain sizes, from tens of angstroms (the very small grains) to a few submicrons (the larger ”standard” grains). However, characteristics of extinction and polarization are insensitive to dust composition. Studies of rich spectroscopic features at NIR/MIR wavelengths as well as UV absorption lines are essential for deriving the chemical compositions in dust grains.

Spectroscopic studies of UV absorption lines in low density clouds have shown apparent depletions of cosmically abundant heavy elements (e.g., Si, Fe and Mg) in the gas phase of the ISM. Interstellar silicates are now known to be ubiquitous, as evidenced by the strong IR absorption features at 9.7 μm and 18 μm , which are attributed to the Si-O stretching and O-Si-O bending in silicates. Furthermore, the broad and featureless shape of the silicate absorption spectral lines suggest that the silicates are amorphous. IR emission lines ranging from 3 μm to 13 μm are generally attributed to vibrational modes of PAH molecules bathed in strong starlight radiation field. Various ice absorption features (e.g., H_2O, CO, CO_2, CH_3OH, NH_3, CH_4 and H_2CO) have been detected at NIR/MIR wavelengths, indicating the presence of icy mantles on dust grains in dense clouds. Another strong spectroscopic feature is the 2175 Å extinction hump, which is attributed to absorption by extremely small carbonaceous grains.

A number of grain models have been proposed based on astronomical observations and laboratory studies, among which one of the leading candidates is the silicate/graphite/PAH grain model by Li & Draine (2001), which consists of a mixture of amorphous silicate grains and carbonaceous grains, each with a broad size distribution. The carbonaceous grains are assumed to have PAH-like properties at very small sizes ($a \leq 50\,\text{Å}$), and properties of graphite spheres at larger sizes. This silicate/graphite/PAH grain model provides excellent agreement with the observed IR/submm spectral features from the diffuse ISM in the Galaxy and Small Magellanic Cloud. However, it does not include core-mantle grains which clearly exist in the ISM. This brings into focus the partially-successful nature of the existing dust models, which are often sufficient to explain many, but not all spectral features over the full electromagnetic spectrum.

1.4 Dust Thermal Emission: FIR/submm SED Model

Emission and absorption line features are generally small in the FIR/submm (Blain et al. 2003), leading to apparently smooth FIR/submm SEDs dominated by dust thermal continuum emission. However, modeling of the FIR/submm SEDs observed in astronomical objects is far from trivial, as the observed emission spectrum is a complex function of radiative transfer as well as distributions in grain properties, such as composition, size and shape, that affect the way dust absorbs and emits radiation.

In the simple case of a uniform grain population, dust thermal emission is well-approximated by a graybody (modified blackbody) function (Hildebrand 1983)

$$\mathrm{S}_\nu = \Omega\,\mathrm{B}_\nu(\mathrm{T_d})\,\mathrm{Q_{abs}}\,, \tag{1.3}$$

where Ω is a normalization factor having the dimension of the angular extension of the dust cloud, $\mathrm{B}_\nu(\mathrm{T_d})$ is the *Planck function* describing blackbody thermal radiation. $\mathrm{Q_{abs}}$ is the absorption coefficient, defined as $\mathrm{Q_{abs}} \equiv \frac{\mathrm{C_{abs}}}{\pi a_{\mathrm{eff}}^2}$, where $\mathrm{C_{abs}}$ is the absorption cross section and $a_{\mathrm{eff}} \equiv (\frac{3v}{4\pi})^{\frac{1}{3}}$ is the effective grain size (v is the volume of a single particle, and $a_{\mathrm{eff}} = a$ for a spherical grain). Eq. (1.3) implicitly incorporates *Kirchhoff's Law*, which ensures the equality between the emissivity e and the absorption coefficient $\mathrm{Q_{abs}}$ and at all frequencies. In the FIR/submm, $\mathrm{Q_{abs}} = \mathrm{Q_0}\,(\frac{\nu}{\nu_0})^\beta$ by definition of the emissivity index β , where $\mathrm{Q_0}$ is the absorption coefficient normalized at some reference frequency ν_0. The FIR luminosity and dust mass are calculated by

$$\mathrm{L_{fir}} = 4\pi\,\mathrm{D_L^2} \int_{40\,\mu\mathrm{m}}^{1000\,\mu\mathrm{m}} \mathrm{S}_\nu\,\mathrm{d}\nu \tag{1.4}$$

$$\mathrm{M_d} = \frac{\mathrm{S}_\nu\,\mathrm{D_L^2}}{\kappa\,\mathrm{B}_\nu(\mathrm{T_d})}\,, \tag{1.5}$$

where $\mathrm{D_L}$ is the luminosity distance, κ - defined as $\kappa \equiv \frac{3\,\mathrm{Q_{abs}}}{4\,\mathrm{a}\,\rho}$ - is the dust mass absorption coefficient and varies as $\kappa \propto \nu^\beta$. There is significant uncertainty associated with κ, due to the lack of accurate knowledge of interstellar dust properties. κ in the long wavelength limit is expected to be independent of size distribution for "standard" grains, but increase with decreasing grain size for very small amorphous grains which emit strongly at shorter wavelengths (see § 2.3 for detailed discussions). Therefore dust mass given by Eq. (1.5) is essentially an upper limit, especially for galaxies with higher observed dust temperatures. By contrast, FIR luminosity is tightly constrained whenever a satisfactory SED fitting is achieved.

There are other FIR/submm SED models more elaborate than Eq. (1.3) that attempt to account for multiple dust components and general optical depths. However, the applications of such complex models are impractical when the frequency sampling of the SED is limited. More importantly, Blain et al. (2003) show that the added complexity, even if feasible, generally does not lead to appreciable difference in constraining the observed FIR/submm SEDs. Throughout this thesis, we adopt the simple SED model prescribed by Eq. (1.3) and dust parameters assumed by Hildebrand (1983) - $\mathrm{Q}_{125\mu\mathrm{m}} = 7.5 \times 10^{-4}$, $\rho = 3.0\,\mathrm{g/cm^3}$ and $a = 0.1\,\mu\mathrm{m}$, which implies $\kappa_{125\mu m} = 1.875\,(\mathrm{kg/m^2})^{-1}$.

Note that the SED parameters estimated by adopting this simplified approach are only *"effective"* values, given that the observed FIR/submm emission inevitably comes from a mixture of dust grains that are non-uniform in temperature and properties. The observed FIR/submm dust emission spectrum is dominated by that of the warm dust component, as it emits much more efficiently due to the higher temperature as well as higher emissivity at shorter wavelengths. Therefore the observed dust temperature established from multiband FIR/submm photometric measurements is in fact an upper limit of dust temperatures along the line of sight. On the other hand, the observed emissivity index is a lower limit of the actual emissivity index of dust components along the line of sight. The cooler dust component emits predominantly at longer wavelengths, thus has the effect of broadening the spectrum and lowering the observed spectral index of the overall dust emission in the large scale. Scoville & Kwan (1976) show that temperature gradients along the line of sight, even if each grain population has the same spectral index, could easily lower the observed power index by 0.5 from the actual value.

Chapter 2

Dust Temperature and Long-wavelength Emissivity

As discussed in § 1.4, it is difficult, if not impossible, to uniquely disentangle and determine various factors concerning the true physical conditions in the ISM that are collectively responsible for the observed FIR/submm emission from a source. Hence, the dust temperature T_d and emissivity index β obtained from a SED fitting are merely *descriptive* parameters. Nonetheless, here we wish to investigate possible *intrinsic interdependence* between T_d and β , as *physical* parameters, which would provide motivation as well as explanations for potentially establishing an empirical T_d -β relation (see § 3.3).

2.1 Dust Temperature

The energy budget of interstellar dust, to the first order, consists of absorption of UV/optical photons and emission of IR/submm photons. There are, of course, other heating and cooling mechanisms having impact on interstellar dust, such as the CMB, collisions with cosmic rays and gas particles, molecule formation and destruction on grain surface and evaporation of extremely hot grain materials. However, the energy contribution from these mechanisms combined is generally modest. Hence temperatures of interstellar dust primarily depend on the strength of the incident radiation field, as well as on various grain properties that affect the efficiencies with which grains absorb and emit radiation. The lower limit of the dust temperature is set by the CMB at $2.7 \times (1+z)\,\mathrm{K}$ where z is the redshift, while the upper bound is set by the evaporation temperature of typical grain materials (roughly $\sim 2000\,\mathrm{K}$).

Dust temperature profiles vary significantly for grain populations with distinctly different radii (i.e., a few submicrons versus tens of angstroms). The very small grains ($a \leq 50\,\mathrm{Å}$) undergo temperature fluctuations, as they can be transiently heated into temperature spikes ($\mathrm{T_d} \geq 1000\,\mathrm{K}$) upon absorption of UV/optical photons, which are then followed by cooling periods (Sellgren et al. 1985). By contrast, the larger "standard" grains reach equilibrium temperatures, as determined by thermal equilibrium between absorption of UV/optical photons and emission of FIR/submm photons

$$\int_{\mathrm{UV/optical}} \mathrm{C_{abs}}\, c\, u_\nu\, d\nu = 4\pi \int_{\mathrm{FIR/submm}} \mathrm{B}_\nu(\mathrm{T_d})\, \pi a^2\, e\, d\nu\,, \tag{2.1}$$

where u_ν is the energy density of the incident radiation field. *Kirchhoff's Law* dictates $e = \mathrm{Q_{abs}}$ at all frequencies, thus

$$\int_{\mathrm{UV/optical}} \mathrm{Q_{abs}}\, c\, u_\nu\, d\nu = 4\pi \int_{\mathrm{FIR/submm}} \mathrm{B}_\nu(\mathrm{T_d})\, \mathrm{Q_{abs}}\, d\nu\,. \tag{2.2}$$

To derive the exact solution to Eq. (2.2), one would need to have accurate knowledge about the actual $\mathrm{Q_{abs}}$ values at all frequencies, information that is lacking at present. At optical wavelengths, we know $\mathrm{Q_{abs}}$ is relatively constant and near unity. It is generally assumed that on average $\mathrm{Q_{abs}}$ = 0.5 in the UV/optical in the numerical integration of the LHS of Eq. (2.2) (Martin 1978). On the other hand, $\mathrm{Q_{abs}}$ at FIR/submm wavelengths varies as $\mathrm{Q_{abs}} = \mathrm{Q_0}\,(\nu/\nu_0)^\beta$ (by the definition of emissivity index β). We thus have the approximate relation

$$\mathrm{T_d}^{[1]} \propto \left(\frac{\mathrm{F}}{a\,\kappa_0}\right)^{\frac{1}{4+\beta}}\,, \tag{2.3}$$

---

[1] $\mathrm{F} = \frac{8\,\pi\,\mathrm{h}\,\nu_0^4}{\mathrm{c}^2}\,\mathrm{Q_0}\,(\mathrm{k\,T_d/h}\,\nu_0)^{4+\beta}\,\Gamma(4+\beta)\,\zeta(4+\beta)$, where $\Gamma(\mathrm{z}) = \int_0^\infty \mathrm{t^{z-1}e^{-t}\,dt}$ and $\zeta(\mathrm{s}) = \frac{1}{\Gamma(\mathrm{s})}\int_0^\infty \frac{\mathrm{t^{s-1}}}{\mathrm{e^t}-1}\,\mathrm{dt}$ are the Gamma and Riemann ζ functions respectively.

for a uniform grain population. Here F is the integrated incident flux, defined as $\mathrm{F} \equiv \int c\, u_\nu\, d\nu$, characterizing the strength of the incident radiation field. $\kappa_0 = \frac{3\,\mathrm{Q}_0}{4\,a\,\rho}$ is the dust mass absorption coefficient normalized at some reference frequency ν_0, characterizing emissivity of grain material per unit mass in the FIR/submm, and is specific to grain material. Furthermore, in the long wavelength limit, κ is independent of grain size for crystalline, metallic or large amorphous grains, whereas $\kappa \propto a^{-1}$ for small amorphous grains with $a \leq 100\,\text{Å}$ (see detailed discussion in § 2.3).

Several very useful conclusions immediately follow from Eq. (2.3). First, the equilibrium dust temperature $\mathrm{T_d}$ is positively correlated to the strength of the radiation field, but is expected to generally fall within a narrow range, due to the very small power index of $\frac{1}{4+\beta}$. Greenberg (1971) has made extensive calculations of grain equilibrium temperatures for grains with various compositions and vastly different dimensions. The energy density of the diffuse interstellar radiation field (ISRF) can be approximated by that of blackbody emission with an effective temperature $\mathrm{T}_* = 1.0 \times 10^4\,\mathrm{K}$ and a dilution factor $\mathrm{W} = 1.0 \times 10^{-14}$ (Martin 1978). In the shielded interiors of dense clouds, the radiation field can be approximated by a reduced T_*, to account for attenuation of UV/optical radiation by the outer layers of grains, and an appropriate increase in W to keep the total energy density in line with that in the exterior. It is shown that interstellar dust with $a \sim 0.1\,\mu m$ reaches steady state temperatures ranging between 15 K and 20 K in normal interstellar HI regions as well as in dense shielded regions. Various refinements of the radiation field lead to only small changes in dust temperatures. Second, $\mathrm{T_d}$ inversely correlates with dust mass emissivity, i.e. more efficient emitters reach lower steady-state temperatures, in agreement with calculations by Li & Draine (2001) which show graphite grains reach higher temperatures than silicate grains given the same size and radiation field, due to lower mass emissivities in graphitic materials. Similarly, Seki & Yamamoto (1980) estimate metallic materials generally have κ values two orders of magnitude lower than those of dielectric materials, therefore metallic grains are expected to reach higher temperatures. Third, $\mathrm{T_d}$ is expected to negatively correlate with grain radius for crystalline, metallic or large amorphous grains, consistent with results presented by Greenberg (1971), Aannestad (1975) and Li & Draine (2001), while small amorphous grains ($a \leq 100\,\mathrm{\AA}$), if large enough to achieve equilibrium temperature ($a \geq 50\,\mathrm{\AA}$), reach $\mathrm{T_d}$ values independent of grain size. Last, $\mathrm{T_d}$ is expected to decrease as β increases. For instance, higher β values in the presence of ice mantles (Aannestad 1975) have the effect of shifting the grain thermal equilibrium in the direction of lower temperatures, which in turn reinforces formation of ice mantles, and also lead to smaller $\mathrm{T_d}$ gradients within a dusty region.

In summary, thermal emission from grain populations with distinct dimensional characteristics constitutes two well separated components of the overall dust thermal emission. The very small grains are expected to emit strongly at MIR wavelengths ($\lambda \leq 40\,\mu m$), whereas the "standard" grains ($a \sim 0.1\,\mu m$) emit strongly in the FIR/submm ($\lambda \geq 40\,\mu m$).

2.2 Dust Emissivity: Empirical Results

A blackbody has absorption coefficient $\mathrm{Q_{abs}}$ = 1 and emissivity index β = 0 at all frequencies. For other bodies, $\mathrm{Q_{abs}}$ is frequency dependent thus $\beta \neq 0$. $\mathrm{Q_{abs}}$ of interstellar dust is generally a complex function of various grain properties, such as chemical composition (graphite, silicate, ice), structure (crystalline, amorphous), physical nature (dielectric, metallic), and morphology (shape, dimension, clustering). The current estimates of interstellar dust $\mathrm{Q_{abs}}$ bear considerable uncertainties due to the lack of accurate understanding of interstellar grain properties. Similarly, the emissivity index β that characterizes the frequency dependence of the absorption coefficient $\mathrm{Q_{abs}}$ is a complex function of grain properties. Estimates of β offer insights into grain properties, such as grain structure and formation of ice mantles. In addition, reaching accurate estimates of β is crucial for determining important large-scale characteristics, such as dust temperature, dust mass and existence of multiple dust components. This, in turn, has direct implications for some very important topics in modern FIR/submm astrophysics, such as the extension of the FIR/radio correlation found in the local Universe to higher redshifts, and a relationship between the FIR luminosity and the dust temperature ($\mathrm{L_{fir}}$ -$\mathrm{T_d}$ relation) in dusty galaxies.

2.2.1 Astronomical Observations

Multiband flux measurements of dust thermal emission in the Rayleigh-Jeans tail, if available, provide the most accurate estimates of β values of dust grains without prior knowledge of dust temperatures, as flux ratios in the long wavelength limit are independent of $\mathrm{T_d}$. However, this approach is generally observationally challenging due to the usually weak dust emission at long wavelengths. Discussions presented in § 2.3 predict theoretical β values of 1 or 2 for interstellar dust in the long wavelength limit, but observations of astronomical objects in the FIR, submm and mm spectral regions have revealed a wide range of β values. Lower emissivity indices have been observed in active galactic environments, such as circumstellar disks and warm molecular clouds, as well as large-scale dust distributions in infrared luminous dusty galaxies (Knapp et al. 1993, Blake et al. 1996, Dunne et al. 2000). On the other hand, FIR emissivity that has a frequency dependence steeper than quadratic has also been observed in some galactic sources (Schwartz 1982, Lis et al. 1998). Dupac et al.(2003) reported multiband submillimeter observations of a large sample of molecular clouds. A wide range of $\mathrm{T_d}$ and β values were derived from the observed SED curves. In particular, the authors investigated the temperature dependence of β values. They found an inverse correlation between the observed $\mathrm{T_d}$ and β values in the broad observed $\mathrm{T_d}$ -β space, and the anticorrelation is best fitted by a hyperbolic function $\beta = \frac{1}{c_1+c_2\,\mathrm{T_d}}$ with the estimates of the free parameters c_1 and c_2 being 0.4 and 0.008 respectively (see Fig. 3.5).

2.2.2 Laboratory Measurements

Laboratory measurements of the absorption coefficient of interstellar grain analogs at submm/mm wavelengths (Agladze et al. 1996, Mennella et al. 1998) have revealed an intrinsic temperature dependence of grain Q_{abs} and β . In particular, a T_d -β inverse correlation has been observed in the submm/mm spectral range at dust temperatures above $10\,K$.

Agladze et al. (1996) measured absorption spectra of crystalline and amorphous grains at wavelengths ranging between $700\,\mu m$ and $2.9\,mm$ at temperatures between $1.2\,K$ and $30\,K$. The millimeter Q_{abs} , as well as its temperature dependence, was found to be sensitive to grain material and grain structure (Fig. 2.1). Q_{abs} was found to decrease with temperature below $20\,K$, but this trend reverses at higher temperatures. β was found to range between 1.2 and 2.5, and an inverse correlation between β and T_d was observed for amorphous grains at temperatures above $10\,K$. It is important to note that the observed T_d -β inverse correlation at submm/mm wavelengths might not be necessarily valid at FIR/submm wavelengths.

Mennella et al. (1998) measured absorption coefficients of crystalline and amorphous cosmic dust analog grains between $20\,\mu m$ and $2\,mm$ over the temperature range 24-295 K . The temperature and wavelength domains covered in this set of laboratory experiments are more relevant for understanding astronomical observations at FIR/submm wavelengths. Values of Q_{abs} and β , as well as their temperature dependence, were found to be sensitive to grain material and grain structure, and variations in Q_{abs} and β were found to be more prominent in amorphous grains than in crystalline grains. The authors found a monotonic increase of Q_{abs} with dust temperature in the measured temperature range, while β was found to range from 0.5 to 2.3 and decrease as the dust temperature increases (Fig. 2.2).

2.3 Dust Emissivity: Theory

2.3.1 Dipole Approximation and Mie Theory

In the studies of FIR/submm emission by interstellar dust, with sizes ranging from tens of angstroms to a few submicrons, we are concerned with solutions to the scattering and absorption problem in the long wavelength limit ($a \ll \lambda$), where the simple method of the *electrostatic dipole approximation* is applicable (Bohren & Huffman 1983). It treats a grain particle as an electric dipole induced by a uniform oscillating incident field, given by

$$\vec{\mathrm{p}} = 4\,\pi\,a^3\,\frac{\epsilon - 1}{\epsilon + 2}\,\varepsilon_0\,\vec{\mathrm{E}}_{\mathrm{i}}\,, \tag{2.4}$$

where $\vec{\mathrm{E}}_{\mathrm{i}}$ is the incident field and ϵ is the dielectric function. The scattered light is the subsequent electric dipole emission. The absorption coefficient is given by (see § B.1)

$$\begin{aligned} \mathrm{Q}_{\mathrm{abs}} &= 4\,x\,\mathrm{Im}\,(\frac{\epsilon - 1}{\epsilon + 2}) & (2.5) \\ &= \frac{24\pi a}{\lambda}\,\frac{\epsilon''}{(\epsilon' + 2)^2 + \epsilon''^2}\,, & (2.6) \end{aligned}$$

where x is the size parameter, defined as $x \equiv \frac{2\pi a}{\lambda}$. Additionally, scattering is negligible compared to absorption, i.e. $\mathrm{Q}_{\mathrm{scat}} \ll \mathrm{Q}_{\mathrm{abs}}$. This approximation method is justified in the long wavelength limit ($a \ll \lambda$) given that the incident field is essentially uniform over the region occupied by the particle.

There exists a much more general but computationally complex theory (*Mie Theory*, Mie 1908) which provide exact solutions to the scattering and absorption problem for spherical particles by a series expansion in powers of x. A rule of thumb is that retainment of $O(x)$ terms is sufficient to ensure convergence, therefore only the first-order term is retained in the long wavelength limit ($x \ll 1$). Not surprisingly, *Mie Theory* in the long wavelength limit (*Rayleigh Scattering*) yields the same results as the *electrostatic dipole approximation* (Bohren & Huffman 1983).

2.3.2 Crystalline and Metallic Grains

Dielectric functions ϵ of crystalline dielectric and conducting materials can be calculated by the *Lorenz oscillator* and *Drude* optical models respectively (Bohren & Huffman 1983). These models predict that, for crystalline dielectric as well as conducting materials, ϵ'' is very small and ϵ' approaches a constant ($\gg \epsilon''$) in the FIR/submm. The physical explanation behind such optical properties is that the energy possessed by FIR/submm photons is usually too low to excite phonon activities (thermal vibrations) in typical crystalline grain materials, which are allowed at a limited number of frequencies (resonance frequencies) in the MIR with wave numbers comparable to the reciprocal of the lattice spacing. In this scenario, FIR/submm absorption by crystalline materials is mainly permissible through the much weaker damping effects that are associated with the anharmonic terms in the inter-atomic potential.

Using the low-frequency approximations of ϵ (see § B.2), Eq. (2.6) gives

$$\mathrm{Q_{abs}} = \frac{48\pi^2 ac\gamma\omega_p^2}{\omega_0^4[\epsilon(0)+2]^2}\,\lambda^{-2} \propto a\,\lambda^{-2}\,, \tag{2.7}$$

for spherical crystalline grains, where $\gamma \equiv \frac{1}{\tau_0}$ (τ_0 is the damping time), ω_p is the plasma frequency, ω_0 is the resonant frequency, and $\epsilon(0)$ is the dielectric function at zero frequency. Also

$$\mathrm{Q_{abs}} = \frac{48\pi^2 ac\gamma}{\omega_p^2}\,\lambda^{-2} \propto a\,\lambda^{-2}\,, \tag{2.8}$$

for spherical metallic particles, where $\gamma \equiv \frac{1}{\tau_c}$ (τ_c is the the mean free time of conducting electrons), and ω_p is the electron plasma frequency.

Eqs. (2.7) and (2.8) immediately point to two very important properties that are shared by spherical grains made of both crystalline dielectric and conducting materials in the long wavelength limit. First, $\beta = 2$. Second, the mass absorption coefficient $\kappa_0 = \frac{3\,Q_0}{4a\,\rho}$ in Eq. (2.3) is independent of size, i.e. the size distribution does not affect FIR/submm emissivity per unit mass. Additionally, some intrinsic temperature dependence can in principle be expected for $\mathrm{Q_{abs}}$ of interstellar dust due to a combination of various temperature dependent factors. For instance, damping in a crystalline material tends to increase with temperature (Mitra 1969), caused by increased phonon activities at higher temperatures. On the other hand, the resonance frequency ω_0 generally decreases with temperature in a crystalline material due to increasing inter-atomic distance which results in a weaker coupling constant (Tielens & Allamandola 1987). All this leads to an increase in $\mathrm{Q_{abs}}$ with rising dust temperature.

Note that Eqs. (2.7) and (2.8) are only strictly valid for grain particles that are spherical in shape, small in size and with optical properties similar to those of the bulk material. For grains with more general properties, $\mathrm{Q_{abs}}$ can deviate from values calculated by Eqs. (2.7) and (2.8). Andriesse (1974) has shown that the quadratic frequency dependence of $\mathrm{Q_{abs}}$ in crystalline dielectric grains is approximately obeyed at $\lambda \geq 50\,\mu m$ and is accurate at $\lambda \geq 200\,\mu m$. Wright (1987) calculated long-wavelength absorption properties of random aggregates of conducting spheres and derived β values ranging between 0.6 and 1.4 for grains with different fractal dimensions. In addition, calculations of Aannestad (1975) have shown that $\mathrm{Q_{abs}}$ at wavelengths longer than $100\,\mu\mathrm{m}$ is sensitive to the presence of an ice mantle and predicted β values as high as 3.5 for silicate core grains covered with ice mantles.

2.3.3 Amorphous Grains

Optical properties of amorphous materials differ from those of crystalline materials due to the existence of various imperfections. Schlömann (1964) developed a model within the framework of lattice dynamics, which treats an amorphous solid as an ionic crystal with a random charge distribution. Physically, the randomness in charge distribution leads to relaxation of the selection rules governing resonance frequencies, and thus allow phonon activities at all energy levels. The absorption spectrum is therefore dominated by photon-to-phonon coupling at all frequencies, while the damping effects become negligible (effectively vanish).

Schlömann (1964) showed that an amorphous particle, under a time harmonic incident field with frequency ω, displays a complex dielectric function with an imaginary part

$$\epsilon''(\omega) \propto \sum_{\vec{k}} \frac{|q^{\vec{k}}|^2}{a^3\omega} \delta(\omega^{\vec{k}} - \omega)\,. \tag{2.9}$$

In Eq. 2.9, $\omega^{\vec{k}} = c|\vec{k}|$ is the frequency corresponding to a wave vector $\vec{k}$, and $q^{\vec{k}}$ is the Fourier component of the charge distribution $q^{\vec{r}}$, i.e.

$$\begin{aligned} q^{\vec{k}} &= \mathrm{N}^{-1/2} \sum_{\vec{r}} q^{\vec{r}} \exp(-i\vec{k}\cdot\vec{r}) && (2.10) \\ q^{\vec{r}} &= \mathrm{N}^{-1/2} \sum_{\vec{k}} q^{\vec{k}} \exp(i\vec{k}\cdot\vec{r})\,, && (2.11) \end{aligned}$$

where N is the number of lattice sites in the periodicity volume. In perfect crystals $q^{\vec{k}}$ vanishes except for some lattice frequencies, whereas in amorphous solids $q^{\vec{k}}$ is generally nonzero due to the random nature of charge distribution, leading to continuous absorption at all frequencies.

In the long wavelength limit, we replace the summation over $\vec{k}$ in Eq. 2.9 by an integration according to

$$\begin{aligned} \sum_{\vec{k}} &= \frac{a^3}{(2\pi)^3} \int d^3\vec{k} = \frac{a^3}{(2\pi)^3} \int 4\,\pi\,k^2\,dk && (2.12) \\ \sum_{\vec{k}} &= \frac{a^2}{(2\pi)^2} \int d^2\vec{k} = \frac{a^2}{(2\pi)^2} \int 2\,\pi\,k\,dk\,, && (2.13) \end{aligned}$$

for bulk modes in three-dimensional materials and surface modes in two-dimensional materials respectively (Kittel 1976). We thus have $\epsilon'' \propto \omega$ (but independent of a) and $\epsilon'' \propto a^{-1}$ (but independent of ω) for amorphous grains with dimensions of $\mathrm{D} = 3$ and $\mathrm{D} = 2$. Plugging the above results into Eq. (2.6), we have $\mathrm{Q}_{\mathrm{abs}} \propto a\omega^2$ ($\beta = 2$) and $\mathrm{Q}_{\mathrm{abs}} \propto \omega$ ($\beta = 1$) for bulk and surface modes.

In large amorphous grains, internal bulk modes clearly dominate. By contrast, in amorphous grains with high surface to volume ratios (e.g. carbon sheets, layered-lattice silicates, small amorphous grains, and chain-like aggregates of small amorphous particles), surface modes grow in dominance. Seki & Yamamoto (1980) demonstrated surface modes dominate in very small amorphous grains ($a \leq 0.01\,\mu m$). Similarly, Greenberg (1978) investigated a bimodal size distribution of interstellar grains with $a_{\rm l} \sim 0.1\,\mu m$ and with $a_{\rm s} \sim 0.01\,\mu m$, and concluded surface modes dominate if the number density of small amorphous grains dominates that of large grains by a factor of ~ 1000. Furthermore, we note that the mass absorption coefficient $\kappa = \frac{3\,{\rm Q_{abs}}}{4\,a\,\rho}$ of surface-mode-dominated amorphous grains displays a size dependence characterized by $\kappa \propto a^{-1}$, i.e. the smaller grains emit more efficiently per unit mass, whereas κ in bulk-mode-dominated amorphous grains is independent of grain size. In summary, the FIR/submm $\rm Q_{abs}$ of small amorphous interstellar dust has characteristics - $\beta = 1$ and $\kappa \propto a^{-1}$ - that are drastically different from those of crystalline, metallic and bulk-mode-dominated amorphous grains for which we expect $\beta = 2$ and κ is independent of a.

Of particular interest, we argue that considerations of the Schlömann (1964) model would point to general, qualitative expectations about the intrinsic temperature dependence of $\rm Q_{abs}$ and β . As temperature increases, the charge distribution in amorphous solids becomes more disordered, leading to a general increase in $|q^{\vec{k}}|$ and the subsequent enhancement of absorptivity. Additionally, if the effective grain dimension (D) [2] decreases as temperature increases (i.e., grain structure becomes more "open"), β decreases owing to the flatter frequency dependence of phonon density of modes (in fact, $\beta \sim {\rm D}-1$). We note that the positive temperature dependence of $\rm Q_{abs}$ and negative temperature dependence of β hereby proposed are in excellent agreement with laboratory measurements (Mennella et al. 1998).

Finally, we note that there are a number of other competing models/mechanisms that could also contribute to FIR/submm/mm absorption. For example, Agladze et al. (1996), in attempts to explain the experimentally measured temperature de-

---

[2] Here we adopt the concept of fractal dimension (Hausdorff dimension), defined as $\rm D \equiv log_{P/p}N$, where P/p is the size ratio of self-similar fractal objects and N is the number of smaller units that can fit into the larger unit. Structures with lower fractal dimension are more "open".

pendence of absorptivity of various grain materials in the submm/mm, attributed absorption of submm/mm radiation by amorphous solids at low temperatures to tunneling effects within two-level systems (Phillips 1987). They argued that tunneling initially decreases with temperature as temperature increases from $0\,\mathrm{K}$, due to increased population in the low-lying excited states, while the temperature dependence is reversed at higher temperatures as absorption to higher excited states becomes stronger. However, the process of two-level tunneling is expected to dominate only at the lowest temperatures ($\leq 10\,\mathrm{K}$, Fig. 2.1), and the underlying dynamics behind such states is not yet understood.

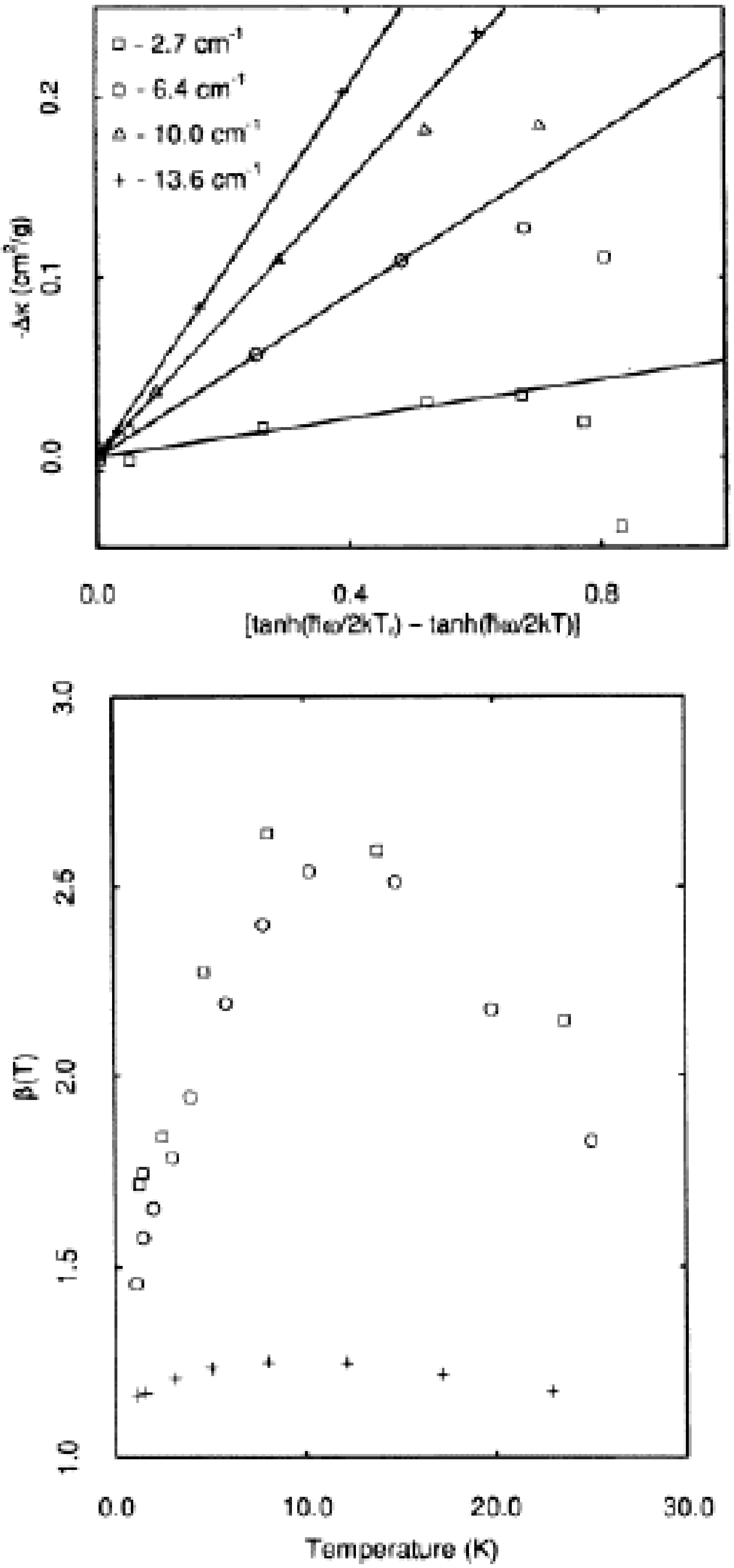

Figure 2.1 Laboratory measurements of: a) temperature dependence of κ in amorphous MgO·SiO$_2$ at T$_\mathrm{d}$ = 1.5, 2.5, 4.7, 8.1, 13.9 and 23.7 K , compared to values predicted by the two-level system model ($\mathrm{T_r} = 1.2\,\mathrm{K}$); b) temperature dependence of β (over the wavelength range of 1 mm to 3 mm) for different amorphous silicate powders (Agladze et al. 1996).

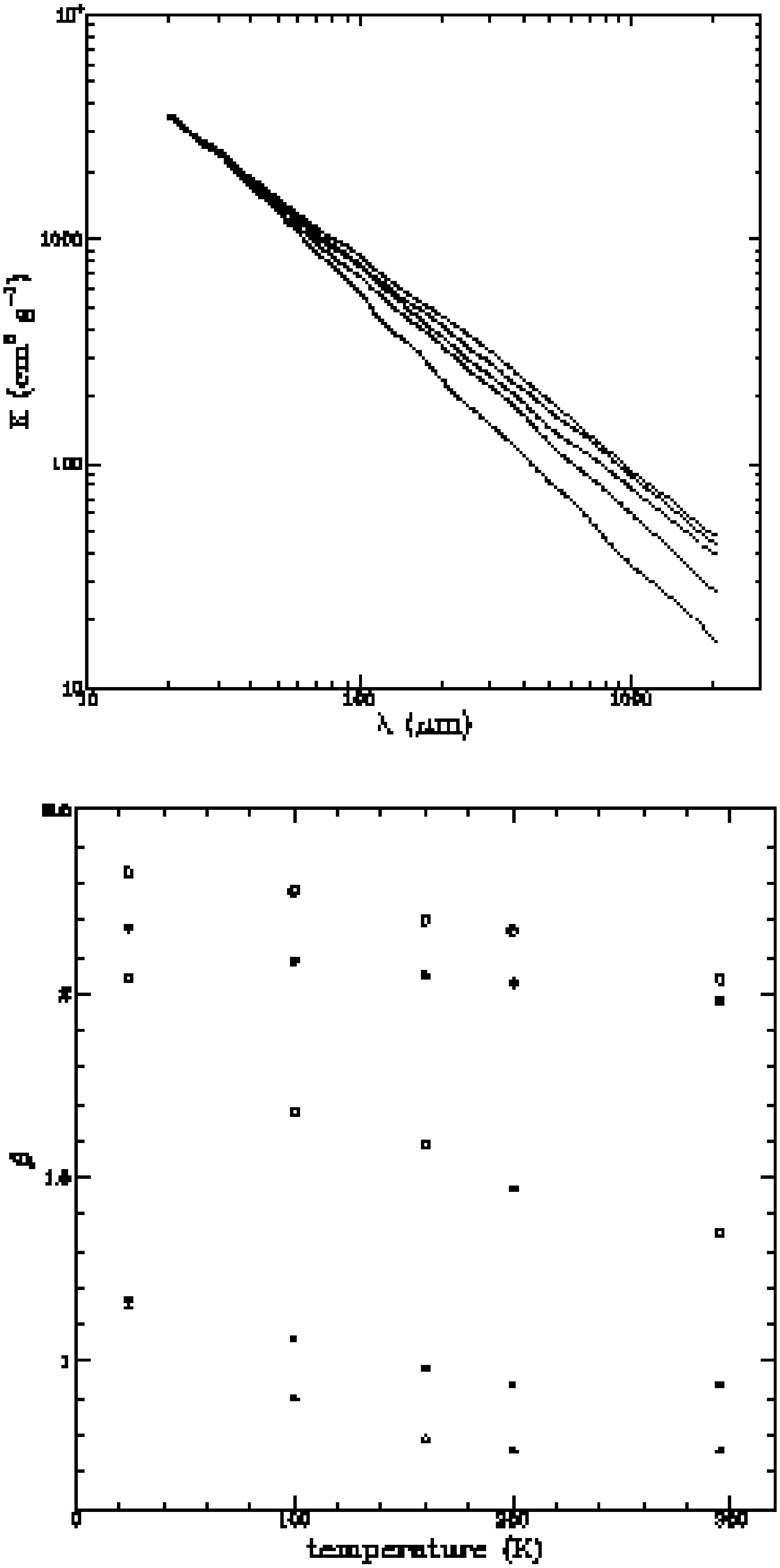

Figure 2.2 Laboratory measurements of: a) wavelength dependence of κ in amorphous carbon grains at T_d = 295, 200, 160, 100 and 24 K (from top to bottom); b) temperature dependence of β (over the wavelength range of 100 μm to 2 mm) for grain with different structures (Mennella et al. 1998).

Chapter 3

350 μm Observations of a Local LIG Sample

Here we present 350 μm observations of 18 LIGs in the local Universe ($0.003 \leq z \leq 0.042$) using the SHARC-II camera (Dowell et al. 2003).

3.1 Description of the Sample

Sources in this sample are mostly selected from the LIG sample presented by Wynn-William & Becklin (WWB, 1993). The WWB sample, not being a strictly defined complete sample, includes 19 sources that were selected from the IRAS Point Source Catalog (PSC), Version 2 (1998) for their high luminosities and high flux densities at 12 μm and 25 μm. We select 16 sources from the WWB sample by requiring $S_{100\,\mu\mathrm{m}} \geq 20\,\mathrm{Jy}$. In addition, 2 ULIGs - UGC 5101 and Mrk 231 - are added onto the list to better understand nearby infrared galaxies at the highest luminosity end. In total, our sample includes 18 nearby LIGs in the redshift range of $0.003 \leq z \leq 0.042$. This sample, with its selection based on high luminosity and high flux densities at the IRAS wavebands, is likely to have an enhanced fraction of galaxies that are more active and contain warmer dust as compared to the bulk of the submillimeter population in this redshift range. The expected high flux densities at 350 μm are very attractive based on observational considerations, as this sample is intended to serve as a backup (bad observing weather) project for SHARC-II observations of the FF sample (see § 4.1). More importantly, a wealth of photometry data at FIR/submm/mm wavelengths is available from the literature for a majority of the sources, which allows for meaningful estimates of both $\mathrm{T_d}$ and β in the SED fitting. We therefore can investigate possible correlations between these two quantities. Table 3.1 and Table 3.2 list the sample and the existing FIR/submm/mm photometric data.

3.2 Results

3.2.1 Observations and Data Reduction

The observations were made during a series of SHARC-II observing runs from 2003 January to 2004 September at the CSO under moderate weather conditions ($0.07 \leq \tau_{225\,\mathrm{GHz}} \leq 0.10$). Integration time varied from source to source, depending on the brightness of each source at 350 μm, atmospheric opacity and sky variability. On average, 0.5 hours of integration time was spent on each source. All measurements were made by scanning the array in a Lissajous pattern centered on each source; scans were taken in full-power mode, i.e. without chopping the secondary. Pointing and calibration scans were taken on an hourly basis on strong submillimeter sources. The absolute calibration was found to be accurate within 20% error margin. Raw data were reduced using the software package CRUSH (Kovács 2006, version 1.50), with the "-faint" option, to obtain a 350 $\mu\mathrm{m}$ map and flux density for each source. All of the 18 sources were clearly detected at levels of $\mathrm{S/N} \geq 10$, and Fig. 3.1 shows the SHARC-II 350 $\mu\mathrm{m}$ maps clipped to have at least half of the maximum exposure. Table 3.3 lists the 350 $\mu\mathrm{m}$ flux densities and flux errors.

3.2.2 Spectral Fits and Derived Quantities

We adopt the single-temperature, optically-thin FIR/submm SED model as described in § 1.4 (Hildebrand 1983, Blain et al. 2003)

$$\mathrm{S}_\nu = \Omega\, \mathrm{B}_\nu(\mathrm{T_d})\, \mathrm{Q}_\nu\,, \tag{3.1}$$

where $\mathrm{Q}_\nu = \mathrm{Q}_0\, (\frac{\nu}{\nu_0})^\beta$. Uniform flux errors at 30% are assumed at each data point, and each flux measurement was weighted equally in the non-linear least squares fit. All but four galaxies (NGC 2388, NGC 4194, NGC 4818 and NGC 5135) in the sample have photometry data at FIR/summ/mm wavelengths other than 60 μm, 100 $\mu\mathrm{m}$ and 350 μm, thus the dust temperature $\mathrm{T_d}$ and emissivity index β can both be treated as free parameters. However, the SED fitting procedure introduces significant $\mathrm{T_d}$ -β degeneracy (Blain et al. 2003) - a problem that persists even when the frequency sampling of the FIR/submm SED is highly redundant (Fig. 3.2, e.g. Mrk 231 for which the SED sampling reaches the maximum within the sample). In the cases of NGC 2388, NGC 4194, NGC 4818 and NGC 5135 where frequency sampling of the SED is limited to three, the emissivity index β is fixed to 1.5 to achieve redundancy. FIR/submm SED fits of the local LIG sample are shown in Fig. 3.3. The best-fitting dust temperatures have the sample median and standard deviation $\mathrm{T_d} = 38.6 \pm 7.7\,\mathrm{K}$ and range within $29.8 \leq \mathrm{T_d} \leq 62.3\,\mathrm{K}$, with two galaxies (NGC 4418, Mrk 231) showing $\mathrm{T_d} \geq 50\,\mathrm{K}$. The emissivity index ranges within $0.9 \leq \beta \leq 2.3$, and have the sample median and standard deviation $\beta = 1.6 \pm 0.3$. Using Eqs. (1.4) and (1.5), FIR luminosity $\mathrm{L_{fir}}$ and dust mass $\mathrm{M_d}$ are found to be $\mathrm{L_{fir}} = 10^{11.2\pm0.6}\,\mathrm{L}_\odot$ and $\mathrm{M_d} = 10^{7.4\pm0.6}\,\mathrm{M}_\odot$ respectively, and range within $10^{9.9} \leq \mathrm{L_{fir}} \leq 10^{12.2}\ \mathrm{L}_\odot$ and $10^{6.2} \leq \mathrm{M_d} \leq 10^{8.3}\ \mathrm{M}_\odot$. Table 3.3 lists estimates of $\mathrm{T_d}$ and β , along with derived values of $\mathrm{L_{fir}}$ and $\mathrm{M_d}$; histograms of these quantities are shown in Fig. 3.4.

3.3 $\mathrm{T_d}$ -β Relation

One interesting objective for this project is to investigate a possible relationship between the dust temperature and the emissivity index ($\mathrm{T_d}$ -β relation).

3.3.1 Observed $\mathrm{T_d}$ -β Inverse Correlation

A negative correlation between estimates of $\mathrm{T_d}$ and β values clearly emerges from the $\mathrm{T_d}$ -β scatter plot (Fig. 3.5). Without prior knowledge of the true probability distribution function of $\mathrm{T_d}$ and β , the non-parametric (rank) correlation coefficient ρ_{np} between these two variables provides a more robust correlation test than the parametric correlation coefficient ρ_{p}. ρ_{np} and ρ_{p} are calculated as

$$\rho_{\mathrm{np}} = \frac{\sum_{\mathrm{i}}(\mathrm{R_i}-\overline{\mathrm{R}})(\mathrm{S_i}-\overline{\mathrm{S}})}{\sqrt{\sum_{\mathrm{i}}(\mathrm{R_i}-\overline{\mathrm{R}})^2}\sqrt{\sum_{\mathrm{i}}(\mathrm{S_i}-\overline{\mathrm{S}})^2}} \tag{3.2}$$

$$\rho_{\mathrm{p}} = \frac{\sum_{\mathrm{i}}(\mathrm{T_{d,i}}-\overline{\mathrm{T_d}})(\beta_{\mathrm{i}}-\overline{\beta})}{\sqrt{\sum_{\mathrm{i}}(\mathrm{T_{d,i}}-\overline{\mathrm{T_d}})^2}\sqrt{\sum_{\mathrm{i}}(\beta_{\mathrm{i}}-\overline{\beta})^2}}\,, \tag{3.3}$$

where $\mathrm{R_i}$ and $\mathrm{S_i}$ are respectively the ranks of $\mathrm{T_{d,i}}$ and β_{i} within the sample (*Numerical Recipes*). The ρ_{np} observed in the local LIG sample is calculated to be $\rho_{\mathrm{np}} = -0.80$, and it is non-zero at the significance level of $(1-\mathrm{p})$, where $\mathrm{p} \sim 6.27 \times 10^{-4}$. We thus conclude the $\mathrm{T_d}$ -β inverse correlation observed in the local LIG sample is statistically significant.

3.3.2 $\mathrm{T_d}$ -β Degeneracy in the SED Fitting and Simulation Methods

However, $\mathrm{T_d}$ and β values are simultaneously estimated from SED fitting procedures, in which a strong and negative $\mathrm{T_d}$ -β degeneracy is present and could potentially introduce an artificial $\mathrm{T_d}$ -β inverse correlation into the sample. We address this problem by repeatedly performing SED fittings on simulated photometric data, described as follows.

Two sets of uniformly distributed random numbers are generated within the ranges of $20 - 60$ and $1.0 - 2.5$, and they are taken to be the simulated values of $\mathrm{T_d}$ and β respectively for each source in the sample. Furthermore, we assume measurement errors to be normally distributed and at a constant level of 30%. We thus simulate noise to signal ratios with normally-distributed random numbers $\sim \mathrm{N}(0, 0.3)$ at all wavelengths. Using simulated values of $\mathrm{T_d}$, β and measurement errors, simulated photometric data are calculated at all FIR/submm wavelengths where observed data are available for each source in the sample. SED fitting of the simulated photometric data for each source follows, yielding fitted values of $\mathrm{T_d}$ and β . We calculate non-parametric correlation coefficients between the "real" (simulated) as well as the fitted values of $\mathrm{T_d}$ and β in the sample.

The above steps are repeated for many times ($\sim$ 10000), and the probability distribution functions of the non-parametric correlation coefficients are thereby established. As shown in Fig. 3.6, ρ_{np} of the simulated $\mathrm{T_d}$ -β show a distribution well approximated by a Gaussian function $\sim \mathrm{N}(-0.01, 0.29)$, as can be expected from the central limit theorem and the fact that the simulated $\mathrm{T_d}$ -β are independently drawn random numbers. By contrast, ρ_{np} of the fitted $\mathrm{T_d}$ -β roughly follows a Gaussian distribution $\sim \mathrm{N}(-0.29, 0.27)$, suggesting SED fitting typically introduces a non-parametric $\mathrm{T_d}$ -β correlation coefficient at the level of $\rho_{\mathrm{np}} \sim -0.29$ ($\mathrm{p} \sim 0.31$) when $\mathrm{T_d}$ and β are in fact uncorrelated, given the sample size and available frequency samplings of each source in the local LIG sample. Under the normal distribution $\sim \mathrm{N}(-0.29, 0.27)$, the observed $\mathrm{T_d}$ -β correlation coefficient, $\rho_{\mathrm{np}} = -0.80$, is significant at the level of $(1 - \mathrm{p})$, where $\mathrm{p} \sim 2.91 \times 10^{-2}$. Hence, we deem the negative $\mathrm{T_d}$ -β degeneracy in the SED fitting insufficient to explain the $\mathrm{T_d}$ -β inverse correlation observed in the local LIG sample and conclude that the observed $\mathrm{T_d}$ -β inverse correlation is real.

3.3.3 Functional Fitting

Based on physical considerations, particularly Eq. (2.3) , we fit the observed $\mathrm{T_d}$ -β inverse correlation using the function form

$$\mathrm{T_d} \;=\; c_1{}^{\frac{1}{c_2+\beta}} \,. \tag{3.4}$$

The best fit to Eq. (3.4) for the local LIG sample is

$$\mathrm{T_d} \;=\; [5.03\times 10^9]^{\frac{1}{4.46+\beta}} \,. \tag{3.5}$$

Eq. (3.5) provides a good fitting to ($\mathrm{T_d}$, β) observed in the local LIG sample, as shown in Fig. 3.5. We also try two alternative function forms in which β is a power or hyperbolic function of $\mathrm{T_d}$, i.e.

$$\beta \;=\; c_1\,\mathrm{T_d}{}^{c_2} \tag{3.6}$$

$$\beta \;=\; \frac{1}{c_1+c_2\,\mathrm{T_d}} \,. \tag{3.7}$$

The best fits to Eqs. (3.6) and (3.7) are, respectively, $\beta = [66.96]\,\mathrm{T_d}{}^{-1.01}$ and $\beta = [63.45]/\mathrm{T_d}$, and yield $\mathrm{T_d}$ -β curves nearly identical to Eq. (3.5). Hence we consider Eq. (3.5) as the best description of the $\mathrm{T_d}$ -β relation observed in the local LIG sample. We also test this $\mathrm{T_d}$ -β relation in the SED fittings of a ULIG sample at much greater cosmological distances (§ 4.2.2), and reach circumstantial confirmation of a $\mathrm{T_d}$ -β relation, as described by Eq. (3.5), in the more distant Universe.

We compare the $\mathrm{T_d}$ -β relation seen in the local LIG sample with that derived by Dupac et al. (2003) from multiband submillimeter observations of a large sample of molecular clouds in the Galaxy. SED fittings of these Galactic molecular clouds reveal a clear $\mathrm{T_d}$ -β inverse correlation that is best fitted by a hyperbolic function of the form

$$\beta = \frac{1}{0.40+0.008\,\mathrm{T_d}} \,. \tag{3.8}$$

Eq. (3.8) is overplotted in Fig. 3.5. Clearly, the $\mathrm{T_d}$ -β correlation seen in the Galactic molecular clouds is significantly different from, in fact much flatter than, that observed in the local LIGs, despite their agreement in the qualitative trend. The difference in the shape of the observed T_d -β correlations is intriguing. They are derived for astronomical samples of differing nature, scales and environments. We also note that the (T_d , β) estimates for the molecular clouds are based on SED fittings without flux measurements at wavelengths shortward of the SED peaks, which would otherwise greatly improve the accuracy of the T_d estimates. Dedicated observational, laboratory and theoretical efforts in the future would allow us to more precisely quantify the T_d -β relation, discover its full range, as well as investigate its evolution with grain properties and physical environments.

3.3.4 Explanations

We conclude the T_d -β inverse correlation observed in the local LIG sample is statistically significant and physically real. The best fitting functions is

$$T_d = [5.03 \times 10^9]^{\frac{1}{4.46+\beta}} .$$

Three explanations, in our opinion, are plausible for an empirical inverse correlation between T_d and β .

First, following discussions presented in § 2.1, particularly Eq. (2.3), we expect T_d to display monotonic negative dependence on β given any radiation field and grain material.

Second, following discussions presented in § 2.2.2, we expect β to exhibit intrinsic negative T_d dependence, due to the proposed inverse temperature dependence of the effective grain dimension.

Third, an inverse T_d -β relation can be caused by mixtures of non-uniform grain populations, particularly those involving grains covered with ice mantles and/or very small grains. As noted in § 2.3, high β values (as high as 3.5) can be expected for dust grains covered with ice mantles, whereas very small grains are expected to have low β values (~ 1). On the other hand, while low T_d values favor formation of ice mantles and lead to strong emission at longer wavelengths, high T_d values (or temperature fluctuations) in very small grains prohibit accretion of ice mantle and lead to strong emission at shorter wavelengths. As a result, (T_d , β) observed in the large-scale tend to move in the direction of low-T_d -high-β when the overall dust emission is dominated by that of cold dust possibly covered with ice mantle, and shift to high-T_d -low-β when very small grains dominate the overall emission.

3.3.5 Applications

A T_d -β relation, if valid over a wide range of LIG/ULIG populations, would be extremely useful for modeling their observed FIR/submm SEDs.

First, a T_d -β relation would effectively reduce the number of variables (therefore the number of required flux measurements) by one in the SED fittings. This effect is especially desirable for studying faint, distant submm sources, as well as interpreting results from single submm wavelength imaging and deep field surveys, given the considerable observational challenge typically faced by deep submm observations.

Second, for any given photometric dataset, a T_d -β relation would either allow estimates of one more variables in the SED fittings, or improve the uncertainties associated with the fitted variables. This effect is exemplified by SED fittings of a sample of ULIGs at moderate redshifts (§ 4.1, FF sample, $0.089 < z < 0.926$), for which the available frequency sampling in the FIR/submm is fairly limited (at 60 μm , 100 μm and 350 μm). By using the T_d -β relation observed in the local LIG sample, a full T_d -β analysis of the FF sample becomes feasible in which estimates of both variables - T_d and β - can be achieved (§ 4.2.2). This represents a major advance over the more conventional and commonly utilized SED modeling method, which, without the application of a T_d -β relation, would only allow meaningful estimates for one out of these two very important quantities.

Last, the understanding of a T_d -β relation has implications for questions related to interstellar grain models and physical conditions in the ISM. This is so because, in principal, various physical characteristics - such as the radiation field, grain properties and grain distributions - could all impact $\mathrm{T_d}$ and β , as well as how they relate to each other. However, we note that the task of disentangling the various factors at work is extremely difficult at present, due to the limited availability of detailed measurements that are currently achievable from astronomical observations and/or laboratory experiments.

3.4 Conclusion

We have observed and detected 18 local LIGs ($0.003 \leq z \leq 0.042$) at $350\,\mu\mathrm{m}$, using the SHARC-II camera at the CSO. The acquired $350\,\mu\mathrm{m}$ data, in combination with pre-existing FIR/submm/mm photometric data, lead to accurate estimates for SED properties of these galaxies - dust temperature ($\mathrm{T_d} = 38.6 \pm 7.7\,\mathrm{K}$), emissivity index ($\beta = 1.6 \pm 0.3$), FIR luminosity ($\mathrm{L_{fir}} = 10^{11.2\pm0.6}\,\mathrm{L_\odot}$) and dust mass ($\mathrm{M_d} = 10^{7.4\pm0.6}\,\mathrm{M_\odot}$). A $\mathrm{T_d}$ -β inverse correlation, best described by $\mathrm{T_d} = [5.03 \times 10^9]^{\frac{1}{4.46+\beta}}$, is derived for the local LIG sample. This effect is most likely caused by intrinsic interdependence between $\mathrm{T_d}$ and β as physical parameters, as well as inhomogeneity in grain properties in the ISM. The establishment of a $\mathrm{T_d}$ -β relation is extremely useful in the FIR/submm SED fittings of LIGs/ULIGs, as it serves to effectively reduce the number of free parameters by one in the SED function, which bears desirable consequences from a SED fitting point of view.

Table 3.1. The local LIG sample selected for SHARC-II observations

Source Name	RA J2000	Dec J2000	z	S_{60} Jy	S_{100} Jy
NGC 520	01h24m35.1s	+03d47m33s	0.007609	30.37	46.15
NGC 1614	04h33m59.8s	-08d34m44s	0.015938	33.02	34.35
NGC 2339	07h08m20.5s	+18d46m49s	0.007358	18.45	31.46
NGC 2388	07h28m53.4s	+33d49m09s	0.013790	17.03	25.33
NGC 2623	08h38m24.1s	+25d45m17s	0.018463	23.80	26.66
UGC 5101	09h35m51.6s	+61d21m11s	0.039390	12.24	20.25
NGC 4102	12h06m23.1s	+52d42m39s	0.002823	47.04	73.84
NGC 4194	12h14m09.6s	+54d31m36s	0.008359	24.09	26.06
NGC 4418	12h26m54.6s	-00d52m39s	0.007268	45.58	31.99
Mrk 231	12h56m14.2s	+56d52m25s	0.042170	33.28	30.29
NGC 4818	12h56m48.9s	-08d31m31s	0.003552	20.32	26.72
NGC 5135	13h25m44.0s	-29d50m01s	0.013716	16.93	30.72
Mrk 273	13h44m42.1s	+55d53m13s	0.037780	23.09	21.97
NGC 6000	15h49m49.5s	-29d23m13s	0.007315	36.48	51.76
NGC 6240	16h52m58.9s	+02d24m03s	0.024480	22.87	27.21
IC 5135	21h48m19.5s	-34d57m05s	0.016151	16.36	26.19
NGC 7469	23h03m15.6s	+08d52m26s	0.016317	26.49	36.15
Mrk 331	23h51m26.8s	+20d35m10s	0.018483	18.30	23.44

Note. — Given by NASA Extragalactic Database (NED).

Table 3.2. Other FIR/submm/mm photometric data available for the local LIG sample

Source Name	FIR/submm/mm Photometric Data[a] Jy
NGC 520	S_{850um}= 0.325, $S_{1.3mm}$= 0.050
NGC 1614	S_{850um}= 0.219, $S_{1.3mm}$= 0.011
NGC 2339	S_{450um}= 0.849, S_{800um}= 0.079, $S_{1.3mm}$= 0.019
NGC 2388	...
NGC 2623	S_{850um}= 0.091
UGC 5101	S_{450um}= 1.433, S_{800um}= 0.143, $S_{1.1mm}$= 0.068
NGC 4102	S_{450um}= 1.790, S_{800um}= 0.212, $S_{1.1mm}$= 0.055, $S_{1.3mm}$= 0.050
NGC 4194	...
NGC 4418	S_{450um}= 1.340, S_{800um}= 0.240, S_{850um}= 0.255, $S_{1.1mm}$= 0.085 $S_{1.3mm}$= 0.072
Mrk 231	S_{120um}= 24.32, S_{150um}= 14.74, S_{180um}= 9.75, S_{200um}= 6.88 S_{450um}= 0.513, S_{800um}= 0.085, $S_{1.1mm}$= 0.045, $S_{1.25mm}$=0.029 $S_{1.3mm}$= 0.038
NGC 4818	...
NGC 5135	...
Mrk 273	S_{120um}= 19.99, S_{150um}= 13.10, S_{180um}= 8.69, S_{200um}= 7.40 S_{450um}= 0.707, S_{800um}= 0.084, $S_{1.1mm}$= 0.051, $S_{1.3mm}$= 0.020
NGC 6000	S_{450um}= 1.460, S_{800um}= 0.115, $S_{1.1mm}$= 0.055, $S_{1.3mm}$= 0.018
NGC 6240	S_{120um}= 25.90, S_{150um}= 18.91, S_{180um}= 12.73, S_{200um}= 9.00, S_{450um}= 1.0, S_{800um}= 0.15, $S_{1.3mm}$= 0.021
IC 5135	$S_{1.3mm}$= 0.033
NGC 7469	S_{850um}= 0.192
Mrk 331	S_{850um}= 0.132

[a] Given by NED.

Table 3.3. 350 μm flux and derived properties for the local LIG sample

Source Name	S_{350} Jy	σ_{350} Jy	T_d K	$\sigma(T_d)$ K	β	$\sigma(\beta)$	$\log L_{fir}$ $L_\odot$	$\log M_d$ $M_\odot$
NGC 520	3.52	0.03	35.6	5.7	1.6	0.3	10.76	7.08
NGC 1614	1.34	0.05	38.6	6.7	2.0	0.3	11.36	7.41
NGC 2339	1.98	0.04	31.3	4.5	2.1	0.3	10.54	7.07
NGC 2388	1.92	0.10	37.7	3.2	1.5	-	11.02	7.22
NGC 2623	1.58	0.05	40.2	9.1	1.6	0.4	11.37	7.39
UGC 5101	2.15	0.10	34.3	5.5	1.6	0.3	11.85	8.25
NGC 4102	4.81	0.04	31.5	4.4	2.1	0.3	10.09	6.61
NGC 4194	1.32	0.03	44.2	4.5	1.5	-	10.68	6.53
NGC 4418	2.06	0.08	62.3	18.3	0.9	0.3	10.81	6.15
Mrk 231	1.76	0.07	51.3	8.4	1.4	0.2	12.24	7.80
NGC 4818	2.42	0.04	36.9	3.3	1.5	-	9.90	6.15
NGC 5135	3.35	0.06	33.8	2.6	1.5	-	11.08	7.53
Mrk 273	1.36	0.08	42.7	5.9	1.6	0.2	11.97	7.88
NGC 6000	3.67	0.10	29.8	3.9	2.3	0.3	10.80	7.43
NGC 6240	1.12	0.05	39.2	5.0	1.7	0.2	11.63	7.70
IC 5135	1.90	0.09	37.1	6.4	1.5	0.3	11.16	7.39
NGC 7469	2.49	0.30	40.3	9.2	1.4	0.4	11.34	7.41
Mrk 331	1.88	0.04	39.8	8.9	1.4	0.4	11.29	7.38

Note. — β =1.5 is assumed in the SED fitting for NGC 2388, NGC 4194, NGC 4818 and NGC 5135.

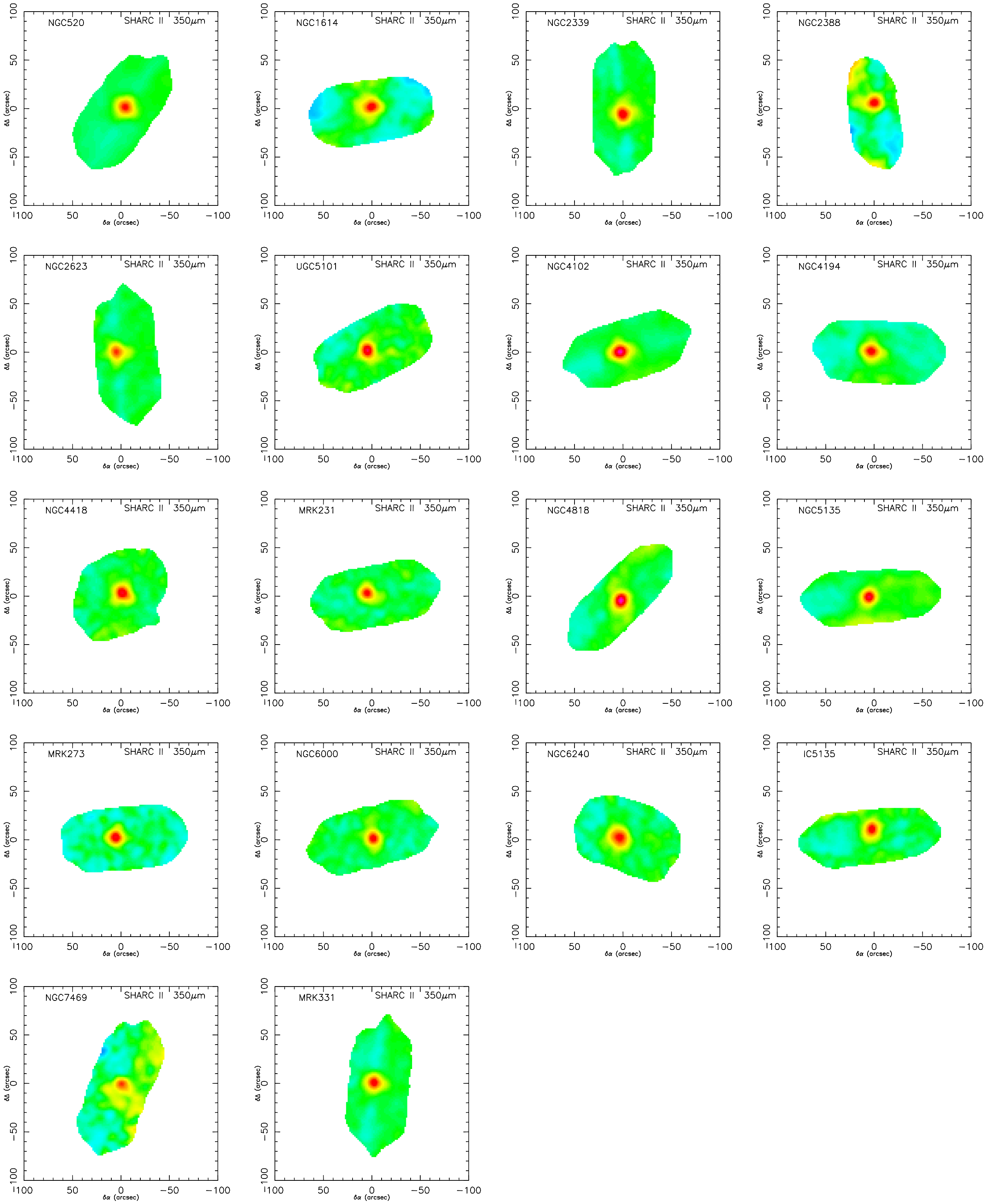

Figure 3.1 SHARC-II 350 μm maps of galaxies in the local LIG sample.

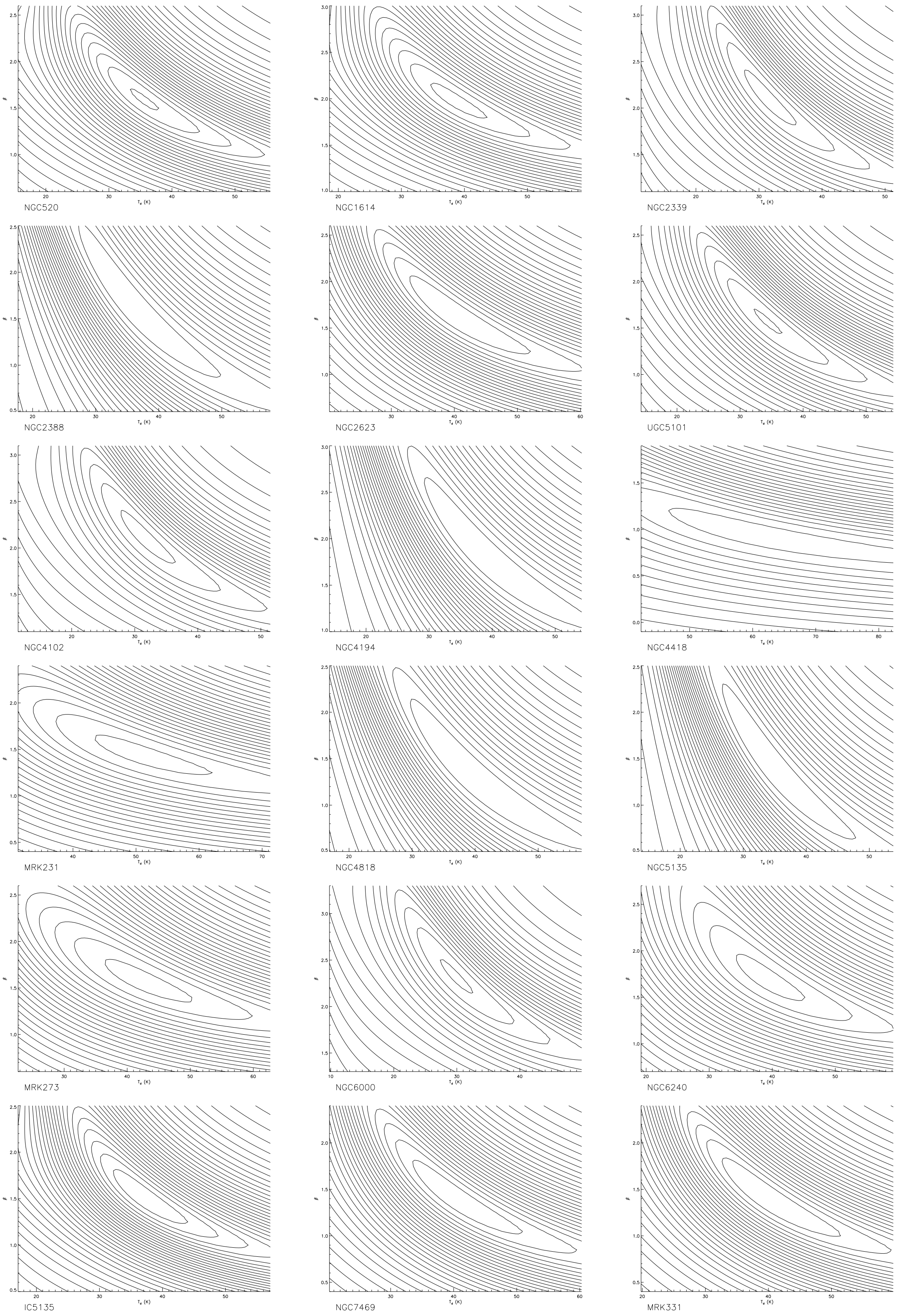

Figure 3.2 χ^2 contours for SED fits of the local LIG sample, plotted in the T_d -β space.

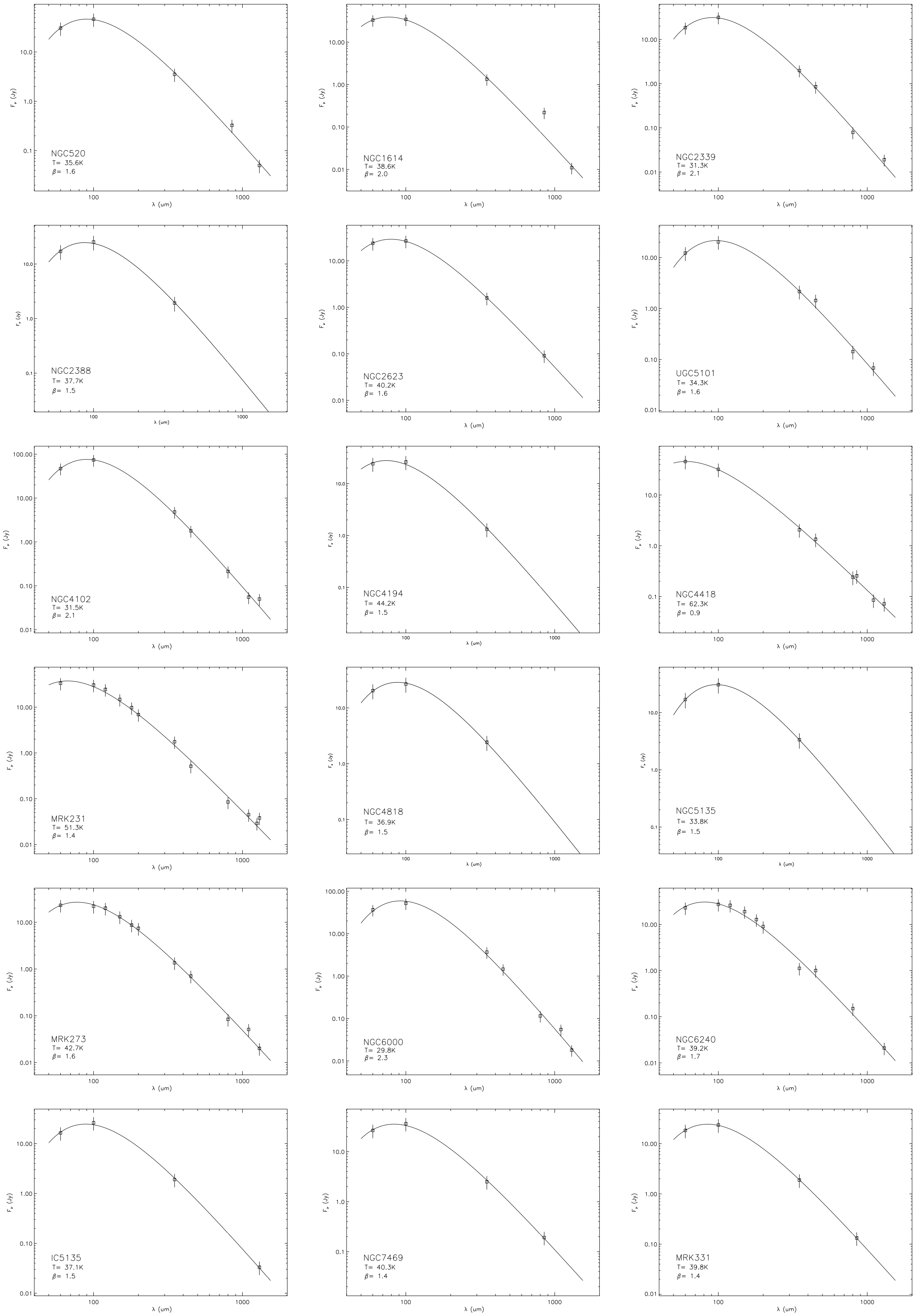

Figure 3.3 SED fits for galaxies in the local LIG sample.

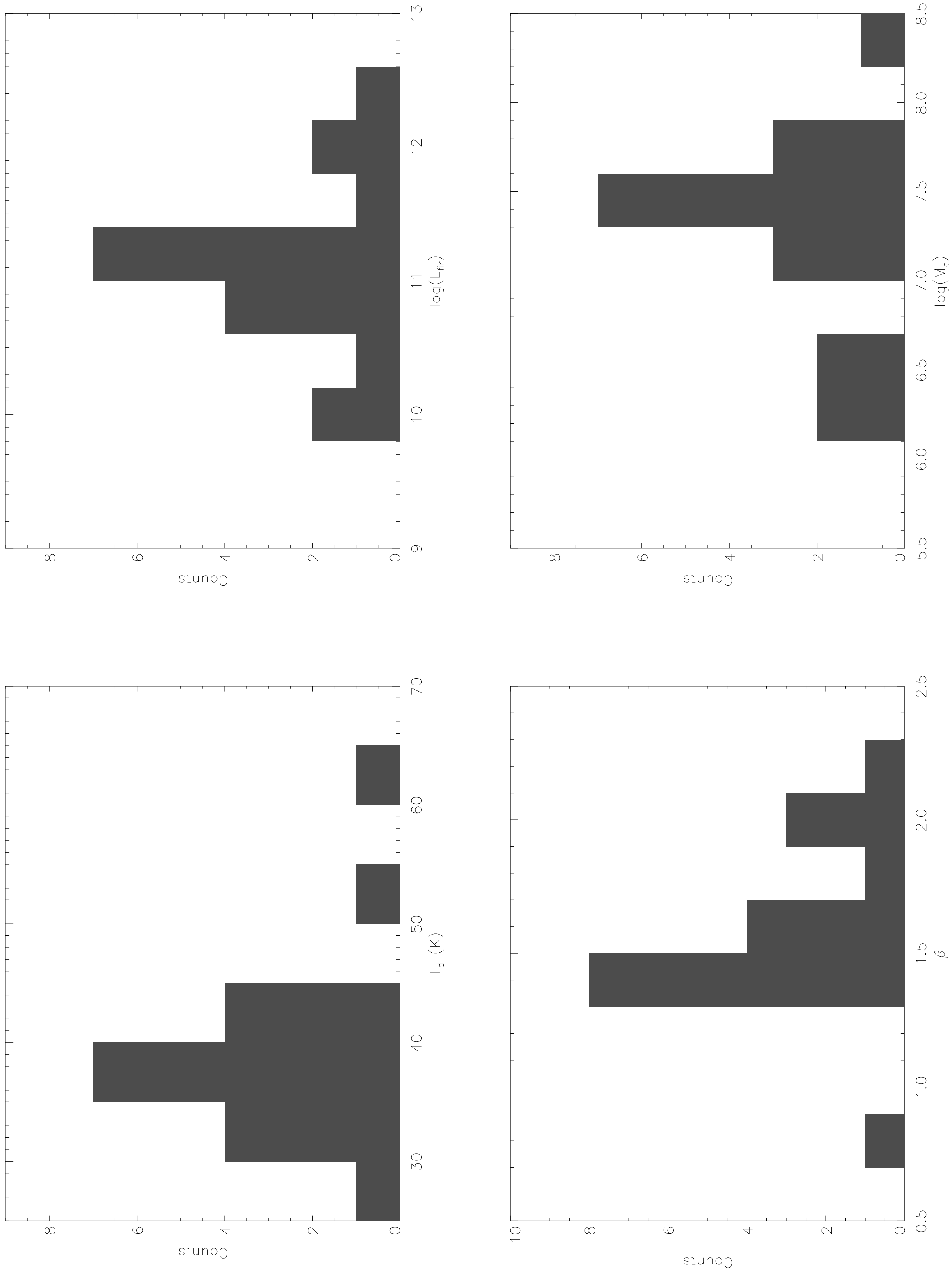

Figure 3.4 Histograms of T_d , β , L_{fir} and M_d values derived for the local LIG sample.

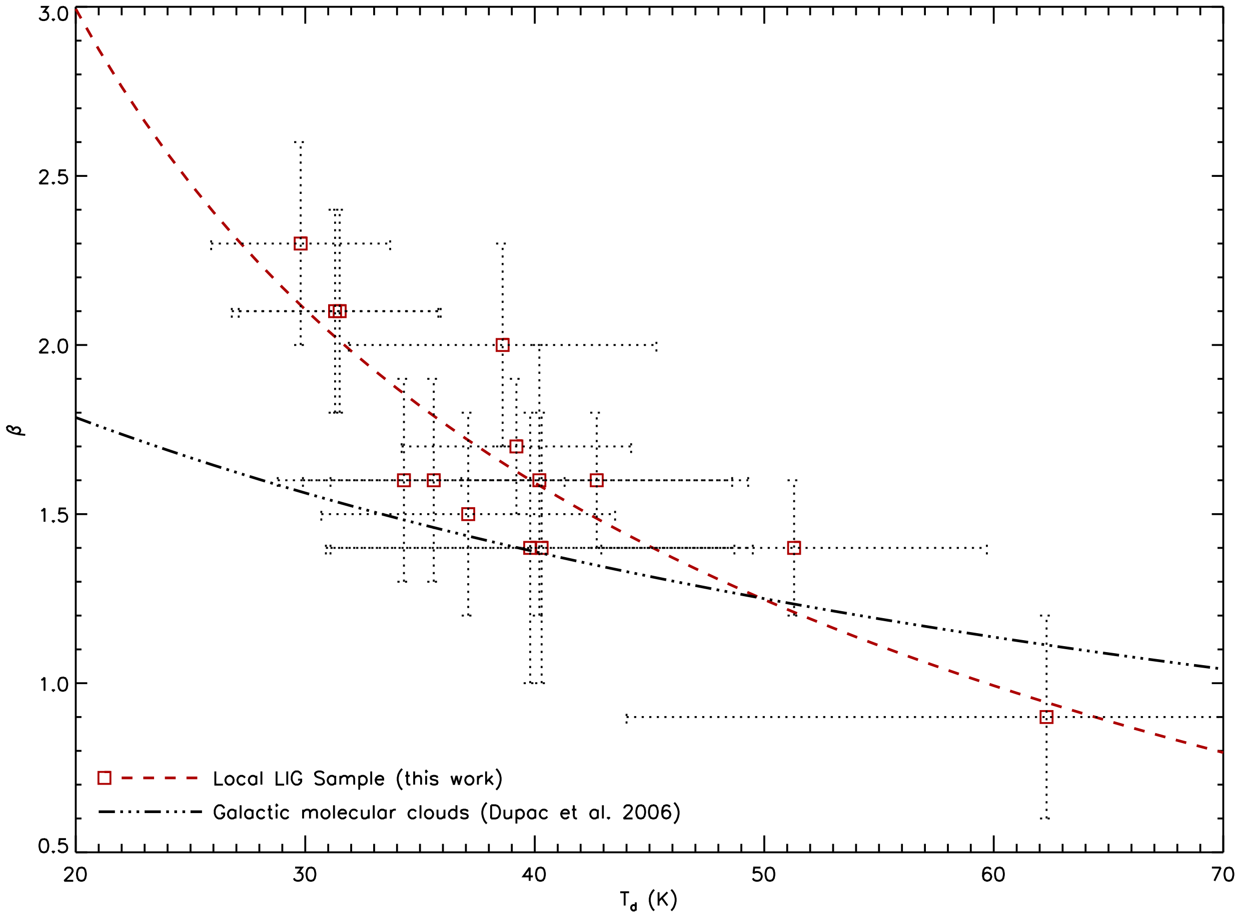

Figure 3.5 The T_d -β inverse correlation observed in the local LIG sample, as compared to that observed in a large sample of molecular clouds in the Galaxy.

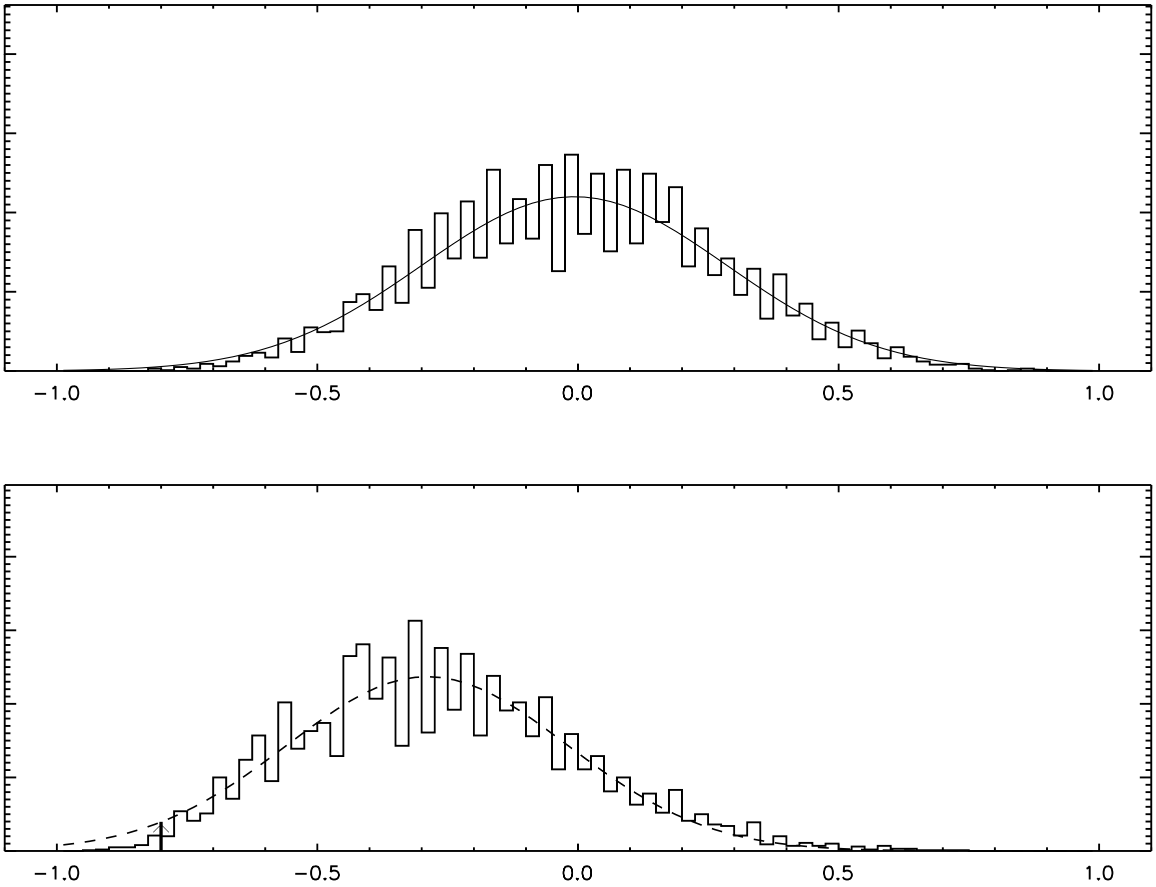

Figure 3.6 Distribution of the non-parametric correlation coefficient of the (uncorrelated) simulated $\mathrm{T_d}$ -β (upper panel, $\sim \mathrm{N}(-0.01, 0.29)$), as compared to that of the fitted $\mathrm{T_d}$ -β given by SED fittings of the simulated photometric data (lower panel, $\sim \mathrm{N}(-0.29, 0.27)$). The non-parametric correlation coefficient of the fitted $\mathrm{T_d}$ -β given by SED fittings of the observed photometric data (marked by the sticker) is clearly significant at a value of $\rho_{\mathrm{np}} = -0.80$.

Chapter 4

350 μm Observations of the FF Sample

Here we present 350 μm observations of 36 ULIGs at moderate redshifts ($0.089 < z < 0.926$) using the SHARC-II camera (Dowell et al. 2003).

4.1 Description of the Sample

This sample targeted for SHARC-II observations is a subset of the FSC-FIRST (FF) catalog presented by Stanford et al. (2000). It was compiled by cross-correlation between the IRAS Faint Source Catalog (FSC, Moshir et al. 1992) and the Faint Images of the Radio Sky at Twenty cm (FIRST, Becker et al. 1995). The limiting 60 μm flux density of the FSC is ~ 0.2 Jy with ~60″ resolution, and the cutoff in 20 cm brightness is ~ 1 mJy with 5″ resolution. Following optical imaging using the Digitized Sky Surveys, optically faint objects that were expected to be dusty luminous infrared galaxies were selected for optical spectroscopic observations and NIR imaging at the K-band. In total there are 108 objects in the FF catalog, for which spectroscopic redshift information and K-band imaging have been successfully obtained. Optical spectra for most of the sources show signs of star-formation. About two-thirds of the NIR morphologies of the catalog reveal signs of galaxy interactions.

There are a few selection biases possibly present in the FF catalog, as compared to the whole submillimeter population over the redshift range $0.1 < z < 1$. First, low-luminosity-high-redshift galaxies are potentially under-represented due to the adverse K-correction at 60 μm and 20 cm . Second, the selection function introduced by flux cutoff at 60 μm is temperature sensitive and acts against representation of infrared galaxies with low dust temperatures in the sample. Third, galaxies with enhanced AGN presence are probably over-represented in the sample, due to boost in FIR and/or radio luminosities expected from AGN accretion.

SHARC-II 350 μm observations of the FF catalog are motivated based on astrophysical as well as observational considerations. As discussed in § 1.1, studies of the IR/submm galaxy population over a wide redshift range is of great importance for understanding the formation and evolution of this population. However, studies of dusty galaxies have so far been mostly focused on the low-redshift and high-redshift Universe, while flux measurements of dusty galaxies at intermediate redshifts remain relatively scarce. Situated in the redshift range of $0.1 < z < 1$, observations of the FF sources nicely fill this void. IRAS observations provided us with valuable data points at 60 μm and 100 μm for the FF sources, but for this catalog virtually no other FIR/submm continuum data points exist, particularly on the low frequency side of the rest-frame SED peak. Our 350 μm flux measurements are thus extremely valuable for attaining meaningful estimates of the SEDs. Precise measurements of spectroscopic redshifts allow accurate estimates of characteristic dust temperatures from the observed SEDs. Finally, targeted observations at 350 μm are made possible due to the positional accuracy provided by radio observations. This is highly desirable for FIR/submm observations given the limited angular resolution currently available to telescopes working in this wavelength range.

We select sources in the FF catalog that have positive detections at both 60 μm and 100 μm for follow-up observations at 350 μm , with no cutoff employed at either waveband. In practice, sources were targeted for observations in real time based on their positions in the sky at the time of observation. In total we observed 36 sources in the FF catalog using SHARC-II, which constitutes a statistically significant sample of dusty galaxies in the redshift range of $0.1 < z < 1$. Table 4.1 lists FF sources targeted for SHARC-II observations, along with their redshifts, flux densities at 60 μm , 100 μm and 1.4 GHz. The redshift distribution for the SHARC-II detected sample, having a sample median of 0.366, is shown in Fig. 4.1. We adopt a cosmology with $\mathrm{H_0} = 70\,\mathrm{km\,s^{-1}\,Mpc^{-1}}$, $\Omega_\mathrm{m} = 0.30$ and $\Omega_\Lambda = 0.70$.

4.2 Results

4.2.1 Observations and Data Reduction

The observations were made during a series of SHARC-II observing runs from 2003 January to 2004 September at the CSO under excellent weather conditions ($\tau_{225\,\mathrm{GHz}} \leq 0.06$). Integration time varied from source to source, depending on the brightness of each source at 350 μm , atmospheric opacity and sky variability. On average, 1.5 hours of integration time was spent on each source. All measurements were made by scanning the array in a Lissajous pattern centered on each source. With the exception of FF 0738+2856, FF 0758+2851, and FF 0804+3919, scans were taken in full-power mode, i.e. without chopping the secondary mirror. Consistent calibrated flux measurements were found between these two observation modes. Pointing and calibration scans were taken on an hourly basis on strong submillimeter sources. The absolute calibration was found to be accurate within 20% error margin. Raw data were reduced using the software package CRUSH (Kovács 2006, version 1.51b), with the "-deep" option, to obtain a 350 μm map and flux density for each source.

In total, 28 out of 36 sources were detected with signal-to-noise ratios $\mathrm{S/N} \geq 3$. This high detection rate (~78%) demonstrates the effectiveness of SHARC-II for studying faint 350 μm sources at $50 \sim 100$ mJy level. Other than the IRAS data, the present results at 350 μm are the first reported detections of FF sources at wavelengths longward of 100 μm , except for FF 1532+3242 and FF 1614+3234 which were previously observed at 90 μm and 180 μm by Verma et al. (2002), and at 850 μm by Farrah et al. (2002) respectively. Tables 4.2 and 4.3 list the 350 μm flux measurements of the FF sources selected for SHARC-II observations; Figs. 4.2 and

4.3 plot their SHARC-II 350 μm maps clipped to have at least half of the maximum exposure and smoothed with a 9″ FWHM beam.

4.2.2 Spectral Fits and Derived Quantities

We adopt the single-temperature, optically-thin FIR/submm SED model as described in § 1.4 (Hildebrand 1983, Blain et al. 2003)

$$\mathrm{S}_\nu = \Omega\, \mathrm{B}_\nu(\mathrm{T_d})\, \mathrm{Q}_\nu\,, \tag{4.1}$$

where $\mathrm{Q}_\nu = \mathrm{Q}_0\,(\frac{\nu}{\nu_0})^\beta$. A flux error at a uniform 30% level is assumed at each data point, hence each flux measurement is weighted equally in the non-linear least squares fit. In contrast to the local LIG sample, a full $\mathrm{T_d}$ -β analysis of the FF sample is not possible due to the paucity of available data points. We fit three SED curves for each source in the SHARC-II detected FF sample, with β fixed to 1.0, 1.5 and 2.0, to achieve redundancy. The fitted SEDs for each source are overplotted (Fig. 4.4) whenever convergence can be achieved by the fitting procedure. β values favored by the observed photometric data points differ from source to source, suggesting real differences in emissivity index among the galaxies. Additionally, higher estimates of $\mathrm{T_d}$ are always associated with lower values assumed for β , which can be understood by the negative $\mathrm{T_d}$ -β degeneracy in the SED fitting procedures, as noted in § 3.2.2. The limited availability of FIR/submm photometric data points thus renders simultaneous estimates of $\mathrm{T_d}$ and β unreliable. We assume $\beta = 1.5$ - a value the most commonly assumed and observed - to estimate effective dust temperature $\mathrm{T_d}$ and derive physical quantities - $\mathrm{L_{fir}}$ and $\mathrm{M_d}$ - for later analysis and discussions (Table 4.2).

The best-fitting dust temperatures in the SHARC-II detected FF sample, with β assumed to be 1.5, are found to have the sample median and standard deviation $\mathrm{T_d} = 40.9 \pm 6.9\,\mathrm{K}$ and range within a wide band of $34 \leq \mathrm{T_d} \leq 60.8\,\mathrm{K}$. A histogram of $\mathrm{T_d}$ is shown in Fig. 4.6 (upper panel). All SHARC-II detected FF galaxies have $\mathrm{T_d}$ values in the range of 34 K to 50 K , except for 3 sources - FF 0050−0039

(z=0.727), FF 1106+3201 (z=0.900), FF 1532+3242 (z=0.926) - that have $\mathrm{T_d} \geq 50\,\mathrm{K}$. The apparent absence of low-$\mathrm{T_d}$ -high-z galaxies within the sample could at least in part be caused by the selection effects inherent to the FF catalog (see § 4.1), while the lack of high-$\mathrm{T_d}$ -low-z (effectively high-$\mathrm{T_d}$ -low-L) galaxies in the sample most likely reflects real properties of the LIG/ULIG population. In keeping with preceding discussions, $\mathrm{L_{fir}}$ and $\mathrm{M_d}$ are calculated by Eqs. (1.4) and(1.5), and found to be $\mathrm{L_{fir}} = 10^{12.2\pm0.5}\,\mathrm{L_\odot}$ and $\mathrm{M_d} = 10^{8.3\pm0.3}\,\mathrm{M_\odot}$. They respectively range within $10^{11.4} \leq \mathrm{L_{fir}} \leq 10^{13.1}\ \mathrm{L_\odot}$ and $10^{7.2} \leq \mathrm{M_d} \leq 10^{8.6}\ \mathrm{M_\odot}$.

Additionally, we wish to test the $\mathrm{T_d}$ -β inverse correlation derived for the local LIG sample (§ 3.3) in the more distant FF sample. The local $\mathrm{T_d}$ -β relation, $\mathrm{T_d} = [5.03 \times 10^9]^{\frac{1}{4.46+\beta}}$, is incorporated in the SED fittings of the FF sample, and the SED fits thereby obtained are plotted in Fig. 4.5. As shown in Fig. 4.5, the assumed $\mathrm{T_d}$ -β relation leads to reasonable SED fits for the vast majority of the SHARC-II detected FF sources, providing strong circumstantial support for a possible extension of the $\mathrm{T_d}$ -β relation derived for a sample of local LIGs/ULIGs to their counterparts in the more distant Universe.

4.3 Discussion

4.3.1 FIR-Radio Correlation

As discussed in § 1.1, a tight FIR-radio correlation is known to hold for a wide range of star-forming galaxies in the local Universe (Condon 1992). Also noted in § 1.1 is the importance of testing the validity of this FIR-radio correlation in galaxy populations with differing global characteristics and redshifts. This remains an open question at the present, due to the enormous observational efforts involved to compile the complete information - multiband FIR/submm fluxes, 1.4 GHz radio flux, and precise redshift measurement - for a large number of galaxies at intermediate and high redshifts. The SHARC-II detected FF sources, having the complete information listed above, constitute a statistically significant sample that is suitable for meaningful investigation of the FIR-radio correlation at moderate redshifts $0.1 < z < 1.0$.

The logarithmic FIR/radio flux ratio q (Helou et al. 1985, Eq. 1.2), is equivalent to

$$q = \log(\frac{\mathrm{L_{fir}}}{3.75 \times 10^{12}\mathrm{W}}) - \log(\frac{\mathrm{L_{1.4GHz}}}{\mathrm{WHz^{-1}}}) \,, \tag{4.2}$$

where $\mathrm{L_{1.4GHz}}$ is the 1.4GHz (rest-frame) radio luminosity. We assume the radio spectral index, defined by $\mathrm{S}_\nu \propto \nu^{-\alpha}$, to be $\alpha \sim 0.7$ in the spectral domain near 1.4GHz where synchrotron emission is dominant. Thus

$$\log(\frac{\mathrm{L_{1.4\,GHz}}}{\mathrm{W\,Hz^{-1}}}) = 17.08 + 2\log(\frac{\mathrm{D_M}}{\mathrm{Mpc}}) - 1.7\log(1+\mathrm{z}) + \log(\frac{\mathrm{S_{1.4\,GHz}}}{\mathrm{mJy}}) \,, \tag{4.3}$$

where $\mathrm{D_M}$ is the comoving distance, related to the luminosity distance $\mathrm{D_L}$ through the relation $\mathrm{D_M} = \frac{\mathrm{D_L}}{1+\mathrm{z}}$; $\mathrm{D_L}$ and $\mathrm{D_M}$ are calculated through formulas given by Hogg (1999).

q is known to have values $q \sim 2.3 \pm 0.2$ in local star forming galaxies (Condon 1992), with FIR luminosity integrated over the wavelength range of $40\,\mu\mathrm{m}$ - $120\,\mu\mathrm{m}$. We want to generalize the FIR-radio correlation to cover the full FIR/submm wavelength range of $40\,\mu\mathrm{m}$ - $1000\,\mu\mathrm{m}$. To that end, we adopt estimates given by Soifer & Neugebauer (1991)

$$\mathrm{L}_{8-40\,\mu\mathrm{m}} \sim 40\% \times \mathrm{L}_{40-1000\,\mu\mathrm{m}} \tag{4.4}$$

$$\mathrm{L}_{8-1000\,\mu\mathrm{m}} \sim (1\,+\,40\%) \times \mathrm{L}_{8-120\,\mu\mathrm{m}} \,. \tag{4.5}$$

It follows

$$\mathrm{L}_{40-1000\,\mu\mathrm{m}} \sim \frac{1}{1.4} \times \mathrm{L}_{8-1000\,\mu\mathrm{m}} \tag{4.6}$$

$$\mathrm{L}_{8-120\,\mu\mathrm{m}} \sim \frac{1}{1.4} \times \mathrm{L}_{8-1000\,\mu\mathrm{m}} \,. \tag{4.7}$$

Thus

$$\mathrm{L}_{40-1000\,\mu\mathrm{m}} \sim \frac{1}{0.6} \times \mathrm{L}_{40-120\,\mu\mathrm{m}} \sim 1.67 \times \mathrm{L}_{40-120\,\mu\mathrm{m}} \,. \tag{4.8}$$

The FIR-radio correlation can now be translated into q values that are bounded within a narrow range with median $\langle q\rangle \sim 2.3 + \log(1.67) \sim 2.52$ and scatter $\sigma_q \sim 0.2$, when the FIR luminosity is integrated to cover the wavelength range of 40 μm - 1000 μm .

Following Eqs. (4.2)-(4.3), and using rest-frame $L_{40-1000\,\mu\mathrm{m}}$, we find q in the SHARC-II detected FF sample to vary within a broad range $1.46 \leq q \leq 2.82$ and have the sample median and standard deviation $q = 2.44 \pm 0.39$ (Table 4.2); its distribution is shown in Fig. 4.6 (lower panel). The presence of radio-loud active galactic nuclei is obvious in galaxies where q values are unusually low. We therefore exclude such sources in the investigation of the FIR-radio correlation by setting a lower bound of $\langle q\rangle - \sigma = 2.05$. 22 out of 28 sources (∼79%) remain in the subset of the SHARC-II detected FF sample, for which we find $q = 2.60 \pm 0.20$, in good agreement with $q \sim 2.52 \pm 0.2$ established for local star-forming galaxies. This supports the notion that the FIR-radio correlation, widely observed in the local Universe, continues to exist at higher redshifts, at least over the redshift range of $0.1 < z < 1.0$. Furthermore, dust heating in these ULIGs at moderate redshifts originates predominantly from star formation activities, with modest contribution to the FIR luminosity from old stellar populations and AGNs. This is in good agreement with optical line emission features observed in the vast majority of the FF sample that are characteristic of star formation regions (Stanford et al. 2000).

4.3.2 Star Formation Rates

As noted in § 1.1, FIR luminosity generally provides an excellent measure of the instantaneous SFRs in galaxies, subject to uncertainties associated with additional dust heating by older stars and/or AGNs. We adopt the conversion factor calibrated by Kennicutt (1998)

$$\frac{\mathrm{SFR}}{\mathrm{M_\odot\ yr^{-1}}} = 1.7 \times \frac{\mathrm{L_{ir}}}{10^{10}\ \mathrm{L_\odot}}\,, \tag{4.9}$$

where $L_{\rm ir}$ is integrated over the full IR and submm wavelength range of $8\,\mu$m - $1000\,\mu$m . To account for possible additional dust heating by sources other than ongoing star formation, as well as variations in the FIR energy fraction, Eq. (4.9) takes on the more general form

$$\frac{\rm SFR}{\rm M_\odot\ yr^{-1}} = 1.7 \times \frac{\rm L_{fir}}{\rm 10^{10}\,L_\odot}\ {\rm f\,X}\,, \tag{4.10}$$

where $L_{\rm fir}$ is integrated over the FIR/submm wavelength range of $40\,\mu$m - $1000\,\mu$m . Here f, ranging over the range $0 \le {\rm f} \le 1$, characterizes the percentage energy contribution to FIR luminosity by massive young stars; and X, having values ≥ 1, is to correct for the flux shortward of $40\,\mu$m . X, in contrast with f, is expected to increase with increasing AGN activities, leading to relatively uniform values of f X to be expected across galaxy populations. As noted earlier, Soifer & Neugebauer (1991) estimated $X \sim 1.4$, thus we have

$$\frac{\rm SFR}{\rm M_\odot\ yr^{-1}} = 2.4 \times \frac{\rm L_{fir}}{\rm 10^{10}\,L_\odot}\ {\rm f}\,. \tag{4.11}$$

Following discussions in § 4.3.1, $f \sim 1$ is expected for majority of the FF galaxies, $L_{\rm fir}$ is thereby translated into SFRs in the SHARC-II detected FF sample with median and standard deviation ${\rm SFR} = 10^{\,2.5\pm0.5}\,{\rm L_\odot\,yr^{-1}}$. The implied SFRs are of a level that is $3-4$ orders magnitude and $4-40$ times, respectively, higher than the average and the maximum SFR observed in normal galaxies (Kennicutt 1998). As discussed in §1.1, such intense large-scale starburst activities are uniquely induced by strong tidal interactions, a scenario consistent with high-resolution radio and NIR observations of the FF catalog that reveal morphological features typical of strong interacting/merging systems for the majority of the sources (Stanford et al. 2000).

4.3.3 $\mathrm{L_{fir}}$ -$\mathrm{T_d}$ Relation

$\mathrm{L_{fir}}$ and $\mathrm{T_d}$ inferred for galaxies in the SHARC-II detected FF sample is shown in Fig. 4.7. For comparative purpose, we also plot $\mathrm{L_{fir}}$, $\mathrm{T_d}$ information compiled by Blain et al. (2004) for samples of luminous dusty galaxies at low (Dunne et al. 2000) and high redshifts (Chapman et al. 2003, Chapman et al. 2004b). In the case of the low-redshift sample, 60 μm , 100 μm and 850 μm data are available and utilized in the SED fitting. In contrast, $\mathrm{L_{fir}}$ and $\mathrm{T_d}$ values of the high-redshift sample are derived by assuming the FIR-radio correlation which has been subsequently confirmed through SHARC-II observations of a subset sample (Kovács et al. 2006).

There is a general positive trend between $\mathrm{L_{fir}}$ and $\mathrm{T_d}$, which can be understood by the approximate relation

$$\mathrm{L_{fir}}^{1} \propto \kappa_0\, \mathrm{M_d}\, \mathrm{T_d^{4+\beta}}\,, \tag{4.12}$$

where κ_0 is the dust mass absorption coefficient normalized at some reference frequency ν_0. Eq. (4.12) is a direct consequence of the single-$\mathrm{T_d}$ -low-opacity SED model - Eq. (1.3). However, there are clearly large dispersions in $\mathrm{T_d}$ at similar FIR luminosities, reflecting scatter in the $\mathrm{L_{fir}}$ -$\mathrm{T_d}$ relation due to variation in dust properties that affect its emissivity, as well as variation in the amount of dust in galaxies. Although significant scatter in $\mathrm{T_d}$ for a given $\mathrm{L_{fir}}$ exists for galaxies within each sample, Fig. 4.7 reveals significant shift in typical $\mathrm{T_d}$ values from sample to sample. In particular, the high-redshift galaxies appear considerably cooler than their counterparts at low and moderate redshifts. This is independently confirmed by recent Spitzer imaging of a sample of high-redshift submillimeter galaxies (SMGs) which reveals that the vast majority (80%∼90%) of the Spitzer detected SMGs have NIR/MIR spectra typical of cold, starburst-like ULIGs (Egami et al. 2004). This difference in characteristic dust temperature, at least in part, is caused by different selection biases introduced by selection criteria specific to each sample. On the

---

[1] $\mathrm{L_{fir}} = \frac{8\,\pi\,\mathrm{h}\,\nu_0^4}{\mathrm{c}^2}\,\kappa_0\,\mathrm{M_d}\,(\mathrm{k\,T_d/h}\,\nu_0)^{4+\beta}\,\Gamma(4+\beta)\,\zeta(4+\beta)$, where $\Gamma(\mathrm{z}) = \int_0^\infty \mathrm{t^{z-1}e^{-t}\,dt}$ and $\zeta(\mathrm{s}) = \frac{1}{\Gamma(\mathrm{s})}\int_0^\infty \frac{\mathrm{t^{s-1}}}{\mathrm{e^t-1}}\,\mathrm{dt}$ are the Gamma and Riemann ζ functions respectively.

other hand, given the distinct redshift ranges these samples represent, the difference in $\mathrm{T_d}$ possibly indicates real cosmological evolution of the LIG/ULIG population with redshift. In particular, we wish to interpret the observed difference in the sample $\mathrm{T_d}$ as an indication of the difference in the global SFE and the physical scale typical of dominant star formation in LIGs/ULIGs at distinct redshifts, following arguments presented in the next section.

4.3.4 $\mathrm{T_d}$, SFE and the Spatial Extent of Star Formation

Eq. (4.12) tells us that the observed $\mathrm{T_d}$ of a galaxy, as a *descriptive* parameter characterizing the large-scale SED, is determined by the total dust heating (and by implication the global star formation rate) per unit dust mass within the galaxy. As such, we expect the observed $\mathrm{T_d}$ to be directly related to the global SFE ($\mathrm{SFE = SFR/M_g}$, where $\mathrm{M_g}$ is the gas mass of the whole galaxy). On the other hand, SFE is known to be primarily regulated by the gas density in a star-forming region (Schmidt law), with the global SFE of a galaxy being the gas-mass-weighted average of SFEs of all star-forming regions. $\mathrm{T_d}$ can therefore be linked to the gas density which governs the dominant star formation in a galaxy; in fact, the observed $\mathrm{T_d}$ is expected to have higher values in galaxies in which star formation occurs over more concentrated regions. A general relationship between the observed $\mathrm{T_d}$ and the spatial extent of star formation is thereby expected.

Guided by the physical reasoning stated above, we derive various proportionalities. Following Eq. (4.10), the global SFE is given by

$$\mathrm{SFE} = \frac{\mathrm{L_{fir}\, f\, X}}{\mathrm{M_g}}\,. \tag{4.13}$$

Eqs. (4.12) and (4.13) lead to

$$\mathrm{SFE} \propto \frac{\kappa_0\, \mathrm{T_d^{4+\beta}\, f\, X}}{\frac{\mathrm{M_g}}{\mathrm{M_d}}} \propto \frac{\mathrm{T_d^{4+\beta}}}{\mathrm{A}}\,, \tag{4.14}$$

where $\mathrm{A} \equiv \frac{\frac{\mathrm{M_g}}{\mathrm{M_d}}}{\kappa_0\ \mathrm{f\ X}}$ is introduced for simplification. Equivalently, we have

$$\mathrm{T_d} \propto \mathrm{SFE}^{\frac{1}{4+\beta}}\ \mathrm{A}^{\frac{1}{4+\beta}}\,. \tag{4.15}$$

Eq. (4.15) suggests that the observed $\mathrm{T_d}$ is directly linked to the global SFE in a galaxy, subject to uncertainties in a combination of factors that affect A values: dust mass emissivity (κ_0), additional dust heating (f), SED shape over the full IR/submm spectral region (X), and gas-to-dust ratio.

Numerous studies conducted at UV, optical and FIR wavelengths have shown that gas density is the primary regulating factor of star formation in diverse environments ranging from disks of normal spirals, to their central regions, and to the most extreme circumnuclear starburst regions. A Schmidt (1959) law of the form,

$$\frac{\Sigma_{\mathrm{SFR}}}{\mathrm{M_\odot\ yr^{-1}\ kpc^{-2}}} \propto \left(\frac{\Sigma_{\mathrm{g}}}{\mathrm{M_\odot\ kpc^{-2}}}\right)^{\mathrm{N}}, \tag{4.16}$$

where Σ stands for a surface density, has been universally established across enormous ranges spanning $5-6$ orders of magnitude in gas densities and SFRs, with the best-fitting index $\mathrm{N} \sim 1.4$ and a small scatter $\sigma_{\mathrm{N}} \sim 0.15$ (Kennicutt 1998). It follows

$$\mathrm{SFE} = \frac{\Sigma_{\mathrm{SFR}}}{\Sigma_{\mathrm{g}}} \propto \Sigma_{\mathrm{g}}^{\mathrm{N}-1}\,. \tag{4.17}$$

Assuming l and $\mathrm{m_g}$ are, respectively, the linear scale and gas mass characteristic of the dominant star-formation (and dust heating), we have the simple relation

$$\Sigma_{\mathrm{g}} \sim \frac{\mathrm{m_g}}{\mathrm{l}^2}\,, \tag{4.18}$$

in the region. Note that l, as discussed here, is a *descriptive* parameter that is used to characterize large-scale observational results. Strictly speaking, $\mathrm{m_g} < \mathrm{M_g}$, but $\mathrm{m_g}$ most likely represents the most significant fraction of $\mathrm{M_g}$. The global SFE, being the mass-weighted average of SFEs of all star-forming regions, can thus be approximated by the SFE that governs the dominant star formation. Using Eqs. (4.14), (4.17) and (4.18), we have

$$\mathrm{T_d^{4+\beta}} \propto \mathrm{A} \, (\frac{\mathrm{m_g}}{\mathrm{l^2}})^{\mathrm{N-1}} \, , \tag{4.19}$$

which relates the observed $\mathrm{T_d}$ of a galaxy to the physical scale and gas mass of the bulk star formation. Equivalently,

$$\mathrm{l} \propto \mathrm{m_g^{\frac{1}{2}}} \, \mathrm{A}^{\frac{1}{2\,(\mathrm{N}-1)}} \, \mathrm{T_d}^{-\frac{4+\beta}{2\,(\mathrm{N}-1)}} \, . \tag{4.20}$$

Assuming $\mathrm{N} = 1.4$ and $\beta = 1.5$, we have

$$\mathrm{l} \propto \mathrm{m_g^{0.5}} \, \mathrm{A}^{1.25} \, \mathrm{T_d^{-6.875}} \, . \tag{4.21}$$

Having established the link expected to exist between the observed $\mathrm{T_d}$ and spatial extent of dominant star formation, we now wish to compare it against observational evidence. Fig. 4.7 shows that the high-redshift ULIGs have the observed $\mathrm{T_d}$ values on average $30\% \sim 40\%$ lower than those in the low-redshift and moderate-redshift ULIGs at a given FIR luminosity, e.g. $\mathrm{L_{fir}} \sim 10^{12}\,\mathrm{L_\odot}$. On the other hand, CO observations of high-redshift ULIGs show that they are very massive systems, having at least 4 time more molecular gas than that observed in local ULIGs (Greve et al. 2005). By Eq. (4.21), we thus expect typical physical scales of starbursts in distant ULIGs, relative to those in the more nearby ULIGs, to be

$$\frac{\mathrm{l_{high\ z}}}{\mathrm{l_{lower\ z}}} = 4^{\,0.5} \, (0.6 \sim 0.7)^{\,-6.875} \, (\frac{\mathrm{A_{high\ z}}}{\mathrm{A_{lower\ z}}})^{\,1.25} \sim 50 \, (\frac{\mathrm{A_{high\ z}}}{\mathrm{A_{lower\ z}}})^{\,1.25} \, . \tag{4.22}$$

High-resolution radio observations of the high-redshift dusty galaxies (Chapman et al. 2004a) point to a scenario of spatially extended starbursts on scales of ~10 kpc in these galaxies, while local ULIGs typically show FIR emission as well as gas concentration in compact regions with scales on the order of $0.1 \sim 1$ kpc (Sanders & Mirabel 1996, Young & Scoville 1991). The ratio of spatial scales of star formation as implied by observations is therefore $10 \sim 100$, in good agreement with that derived in Eq. (4.22). The caveat, of course, lies with uncertainties regarding evolution of several factors - dust emissivity, AGN activity and gas-to-dust ratio - with redshift, which would impact systematic changes in the overall ratio of $\mathrm{A} = \frac{\frac{\mathrm{M_g}}{\mathrm{M_d}}}{\kappa_0\ \mathrm{f}\ \mathrm{X}}$ in LIGs/ULIGs.

4.4 Conclusion

We have conducted 350 $\mu\mathrm{m}$ observations of a sample of 36 moderate-redshift ULIGs ($0.1 < z < 1.0$), using the SHARC-II camera at the CSO, and have made 28 detections. The acquired 350 $\mu\mathrm{m}$ data, in combination with the pre-existing IRAS 60 $\mu\mathrm{m}$ and 100 $\mu\mathrm{m}$ data, lead to meaningful estimates for SED properties of these galaxies, i.e. dust temperatures ($\mathrm{T_d} = 40.9 \pm 6.9\,\mathrm{K}$) and FIR luminosities ($\mathrm{L_{fir}} = 10^{12.2\pm0.5}\,\mathrm{L_\odot}$). These moderate-redshift ULIGs appear to host large amount of warm dust ($\mathrm{M_d} = 10^{8.3\pm0.3}\,\mathrm{M_\odot}$) and are experiencing intense starburst activities ($\mathrm{SFR} = 10^{2.5\pm0.5}\,\mathrm{L_\odot\,yr^{-1}}$). The FIR-radio correlation observed in star-forming galaxies in the local Universe ($q \sim 2.52 \pm 0.2$) continues to hold for ULIGs in the more distant Universe over the redshift range of $0.1 < z < 1.0$ ($q = 2.60 \pm 0.2$), suggesting that dust heating originates predominantly from star formation activities. FIR luminosities and dust temperatures derived for dusty galaxy samples at distinct redshifts reveal a general positive relation between theses two quantities. However, there is significant scatter in both axes, due to differing selection biases as well as variations in dust mass and grain properties. We argue that the observed dispersion in the observed $\mathrm{T_d}$ is tied to the difference in the global SFE and the spatial extent of dominant star formation in LIGs/ULIGs.

Table 4.1. FF sources selected for SHARC-II observations (36)

Source Name	RA J2000	Dec J2000	z	S_{60}[a] Jy	S_{100}[b] Jy	$S_{1.4\mathrm{GHz}}$ mJy
FF 0030−0027	00 30 09.099	−00 27 44.40	0.242	0.59	1.11	2.52
FF 0050−0039	00 50 09.806	−00 39 00.96	0.727	0.22	0.49	4.32
FF 0123+0114	01 23 06.973	+01 14 10.03	0.089	0.23	0.55	1.78
FF 0240−0042	02 40 08.576	−00 42 03.56	0.410	0.20	0.69	0.84
FF 0245+0123	02 45 55.355	+01 23 28.40	0.798	0.17	0.32	2.03
FF 0312+0058	03 12 38.445	+00 58 33.86	0.130	0.26	0.61	3.84
FF 0317−0129	03 17 43.635	−01 29 07.33	0.265	0.21	0.34	1.67
FF 0738+2856	07 38 29.856	+28 56 38.74	0.334	0.25	0.64	1.38
FF 0748+3343	07 48 10.591	+33 43 27.13	0.356	0.64	1.18	2.03
FF 0758+2851	07 58 45.956	+28 51 32.76	0.126	0.62	0.92	3.72
FF 0804+3919	08 04 07.399	+39 19 27.63	0.164	0.25	0.48	5.90
FF 0823+3202	08 23 54.616	+32 02 12.03	0.396	0.23	0.52	0.97
FF 0826+3042	08 26 11.644	+30 42 44.17	0.248	0.31	0.88	3.19
FF 0835+3559	08 35 27.440	+35 59 33.07	0.201	0.33	0.51	0.85
FF 0856+3450	08 56 24.852	+34 50 24.82	0.220	0.24	0.75	8.51
FF 0907+3931	09 07 42.264	+39 31 49.47	0.224	0.26	0.47	1.24
FF 1016+3951	10 16 08.616	+39 51 20.46	0.307	0.21	0.39	2.10
FF 1018+3649	10 18 34.539	+36 49 51.75	0.490	0.20	0.56	9.18
FF 1042+3231	10 42 40.815	+32 31 30.99	0.633	0.21	0.44	6.34
FF 1106+3201	11 06 35.716	+32 01 46.39	0.900	0.19	0.64	13.7
FF 1242+2905	12 42 32.497	+29 05 14.75	0.260	0.19	0.50	1.34
FF 1412+3014	14 12 24.952	+30 14 09.78	0.257	0.15	0.53	2.06

Table 4.1 (cont'd)

Source Name	RA J2000	Dec J2000	z	S_{60}[a] Jy	S_{100}[b] Jy	$S_{1.4GHz}$ mJy
FF 1456+3337	14 56 58.427	+33 37 09.98	0.443	0.27	0.60	1.43
FF 1514+3629	15 14 33.118	+36 29 42.36	0.338	0.24	0.54	0.82
FF 1532+3242	15 32 44.052	+32 42 46.73	0.926	0.26	0.50	5.89
FF 1614+3234	16 14 22.105	+32 34 03.66	0.710	0.15	0.20	1.19
FF 1659+3549	16 59 24.669	+35 49 01.74	0.371	0.29	0.33	0.79
FF 1707+3725	17 07 11.795	+37 25 55.32	0.311	0.13	0.45	2.11
FF 1713+3843	17 13 46.085	+38 43 04.77	0.171	0.37	0.79	1.66
FF 2131−0141	21 31 53.490	−01 41 43.35	0.730	0.11	0.47	2.79
FF 2136−0112	21 36 34.229	−01 12 08.38	0.210	0.29	1.11	3.20
FF 2200+0108	22 00 51.859	+01 08 27.08	0.164	0.20	0.72	2.82
FF 2216+0058	22 16 02.721	+00 58 10.65	0.212	0.51	0.85	1.31
FF 2221−0042	22 21 26.066	−00 42 39.08	0.189	0.20	0.37	0.66
FF 2330−0025	23 30 34.920	−00 25 03.98	0.252	0.25	0.72	1.65
FF 2352−0015	23 52 53.171	−00 15 24.69	0.227	0.19	0.61	0.59

[a] The template amplitude of the noise-weighted mean scan (1003), given by IRAS Scan Processing and Integration (SCANPI), Version 5.0.

[b] The template amplitude of the noise-weighted mean scan (1003), given by SCANPI, Version 5.0, except for FF 0123+0114 and FF 2200+0108, for which the 100 μm fluxes are not available from SCANPI and thus values in Stanford et al. (2000) are adopted.

Note. — Three additional FIR/submm flux measurements are available from the literature - FF 1532+3242: $S_{90\mu m}$= 478 mJy, $S_{180\mu m}$= 397 mJy (Verma et al. 2002); FF 1614+3234: $S_{850\mu m}$= 8.47 mJy (Farrah et al. 2002).

Table 4.2. 350 μm flux measurements and derived properties of SHARC-II detected FF sources (28)

Source Name	z	S_{350} mJy	σ_{350} mJy	T_d K	$\sigma(T_d)$ K	$\log L_{fir}$ $L_\odot$	$\log M_d$ $M_\odot$	q
FF 0030−0027	0.242	208	23.5	37.5	2.9	12.28	8.49	2.68
FF 0050−0039	0.727	54.7	12.8	55.2	4.0	12.88	8.27	1.95
FF 0240−0042	0.410	99.0	14.5	40.3	2.5	12.46	8.51	2.82
FF 0317−0129	0.265	118	10.4	35.7	3.3	11.90	8.22	2.39
FF 0738+2856	0.334	76.6	9.08	41.2	2.8	12.25	8.25	2.60
FF 0748+3343	0.356	153	12.7	43.7	3.4	12.65	8.52	2.76
FF 0758+2851	0.126	98.6	10.5	39.1	3.3	11.58	7.69	2.43
FF 0804+3919	0.164	22.7	6.13	45.2	3.8	11.41	7.20	1.81
FF 0823+3202	0.396	97.3	16.1	40.9	2.9	12.40	8.42	2.74
FF 0826+3042	0.248	183	22.8	34.7	2.3	12.16	8.54	2.44
FF 0856+3450	0.220	127	20.9	34.5	2.2	11.93	8.33	1.90
FF 0907+3931	0.224	61.4	9.13	39.5	3.1	11.81	7.90	2.59
FF 1016+3951	0.307	50.5	12.2	42.1	3.2	12.02	7.97	2.27
FF 1018+3649	0.490	90.0	11.5	43.2	2.9	12.60	8.49	1.74
FF 1042+3231	0.633	70.5	8.68	49.7	3.6	12.77	8.37	1.82
FF 1106+3201	0.900	69.1	17.3	57.0	3.6	13.11	8.45	1.46
FF 1242+2905	0.260	96.3	26.3	35.9	2.4	11.96	8.27	2.57
FF 1412+3014	0.257	79.5	16.6	35.5	2.2	11.89	8.22	2.33
FF 1456+3337	0.443	91.0	14.2	43.9	3.1	12.55	8.42	2.61
FF 1532+3242	0.926	62.1	16.3	60.8	4.1	13.14	8.36	1.83
FF 1659+3549	0.371	74.0	13.3	44.0	4.5	12.22	8.08	2.71
FF 1707+3725	0.311	127	19.2	34.0	2.1	12.11	8.54	2.34

Table 4.2 (cont'd)

Source Name	z	S_{350} mJy	σ_{350} mJy	T_d K	$\sigma(T_d)$ K	$\log L_{fir}$ $L_\odot$	$\log M_d$ $M_\odot$	q
FF 1713+3843	0.171	75.6	21.1	38.8	2.9	11.71	7.85	2.63
FF 2131−0141	0.730	82.6	24.2	46.5	2.7	12.86	8.60	2.12
FF 2136−0112	0.210	71.6	25.3	38.7	2.6	11.86	8.00	2.30
FF 2216+0058	0.212	84.2	23.9	41.8	3.4	12.00	7.97	2.82
FF 2221−0042	0.189	52.5	15.7	37.7	2.9	11.55	7.75	2.77
FF 2330−0025	0.252	142	35.0	35.1	2.3	12.08	8.44	2.63

Note. — β =1.5 is assumed in the SED fitting.

Table 4.3. 350 μm flux measurements of FF sources undetected by SHARC-II (8)

Source Name	z	S_{350} mJy	σ_{350} mJy
FF 0123+0114	0.089	(···)	9.43
FF 0245+0123	0.798	(33.6)	26.6
FF 0312+0058	0.130	(26.8)	16.9
FF 0835+3559	0.201	(43.2)	23.2
FF 1514+3629	0.338	(25.5)	12.0
FF 1614+3234	0.710	(33.1)	30.4
FF 2200+0108	0.164	(···)	44.5
FF 2352−0015	0.227	(91.9)	50.3

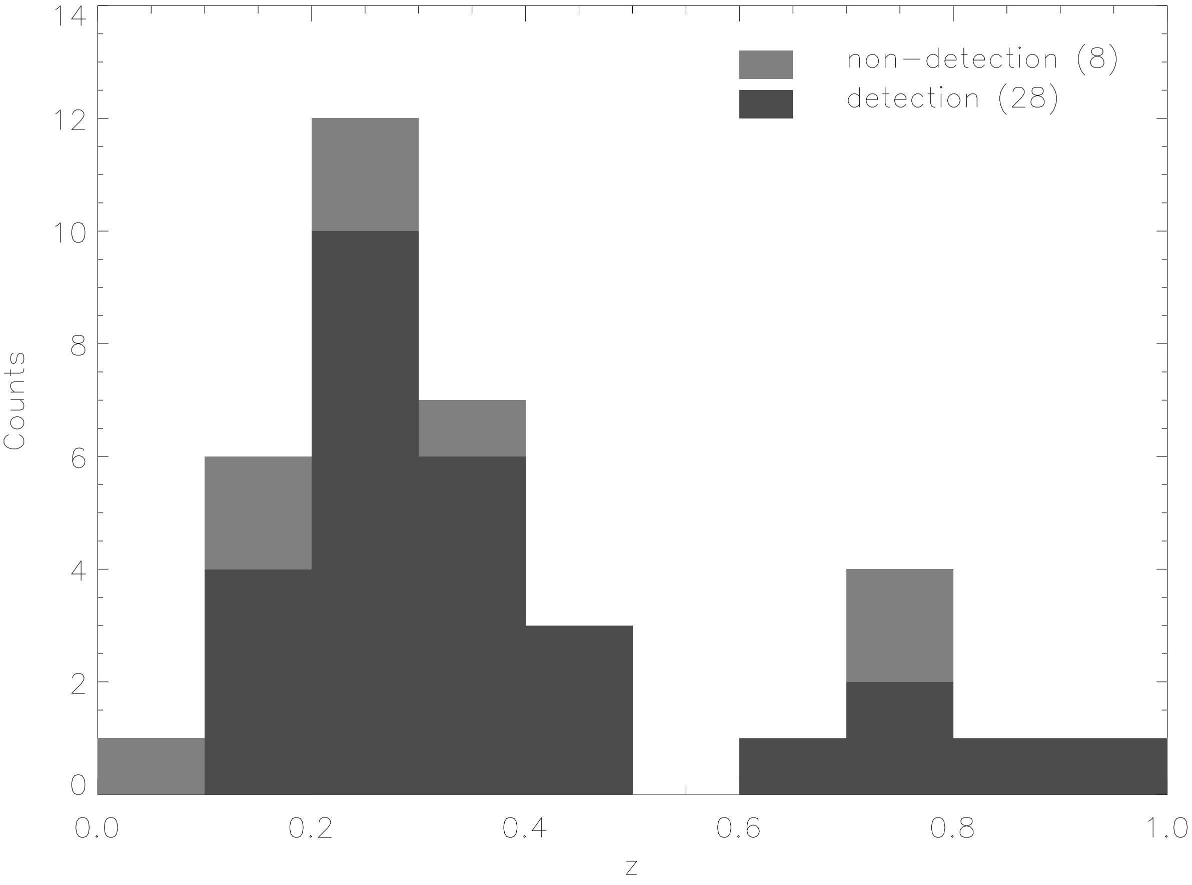

Figure 4.1 The redshift distribution of 36 FF sources selected for SHARC-II observations.

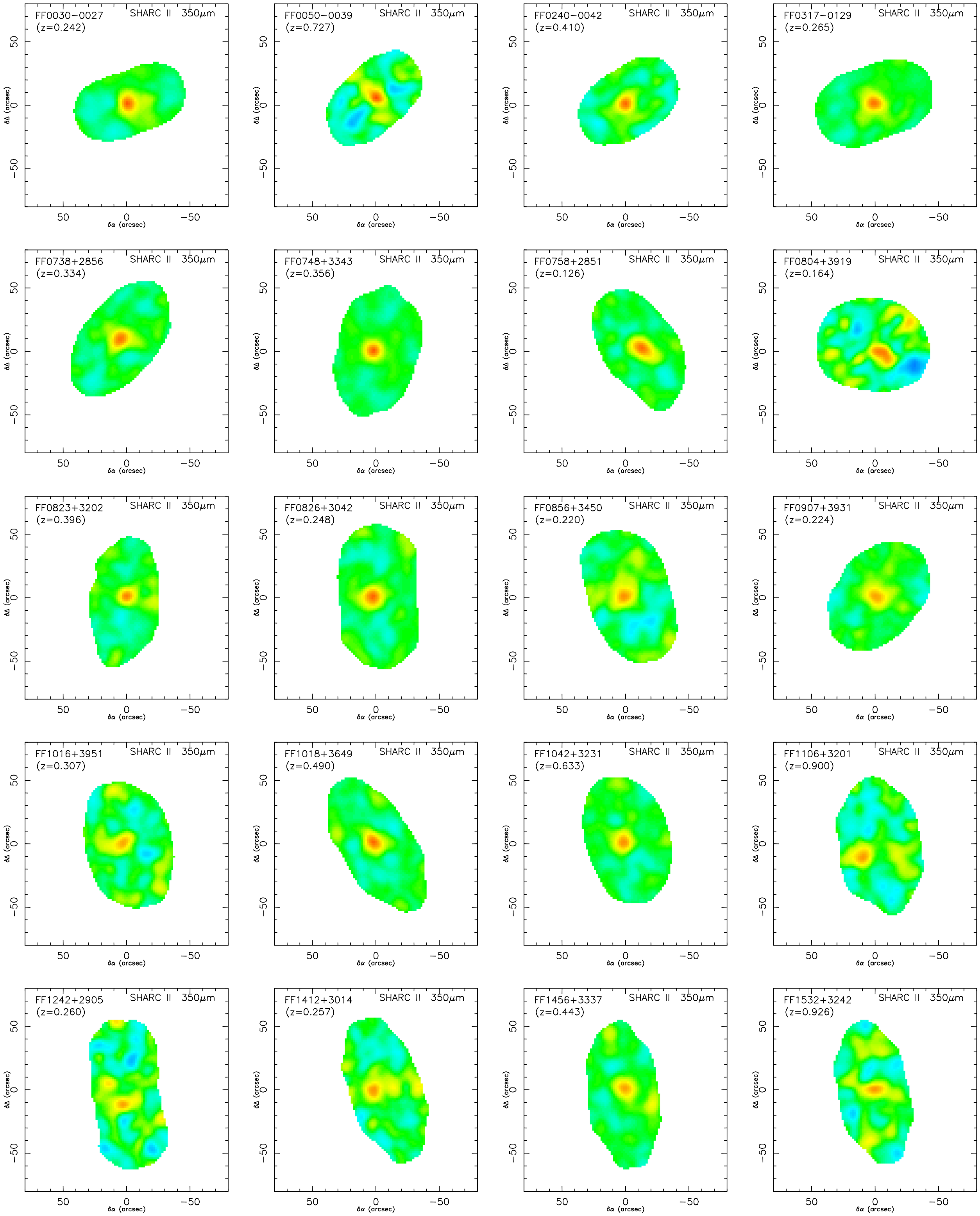

Figure 4.2 350 μm maps of SHARC-II detected FF sources (28).

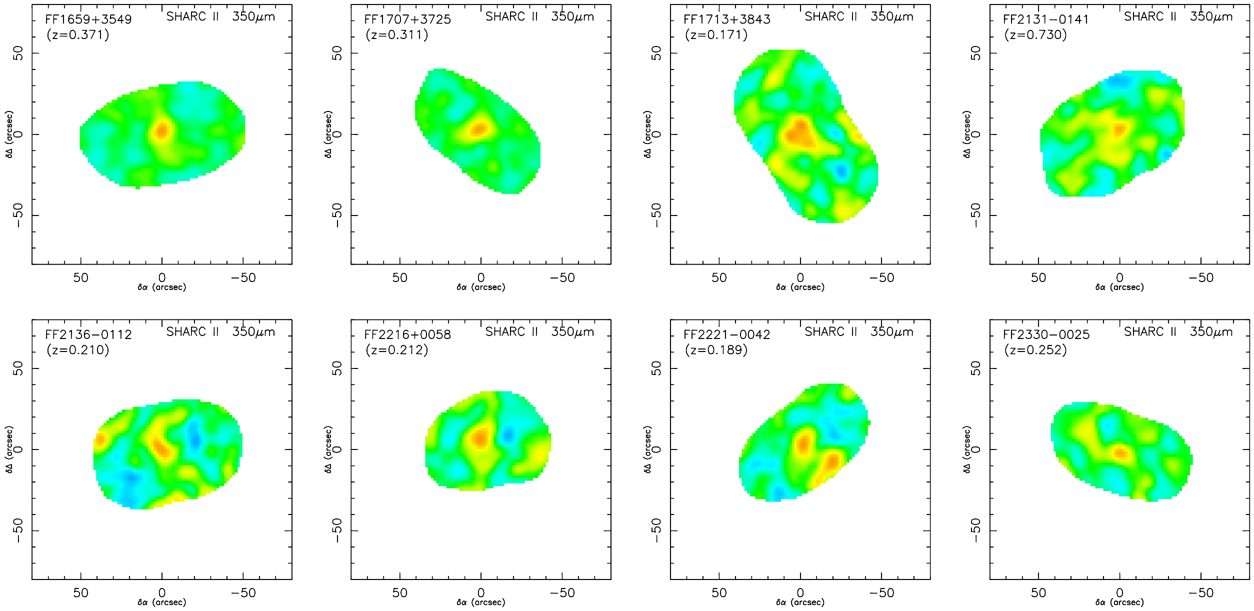

Figure 4.2 Continued

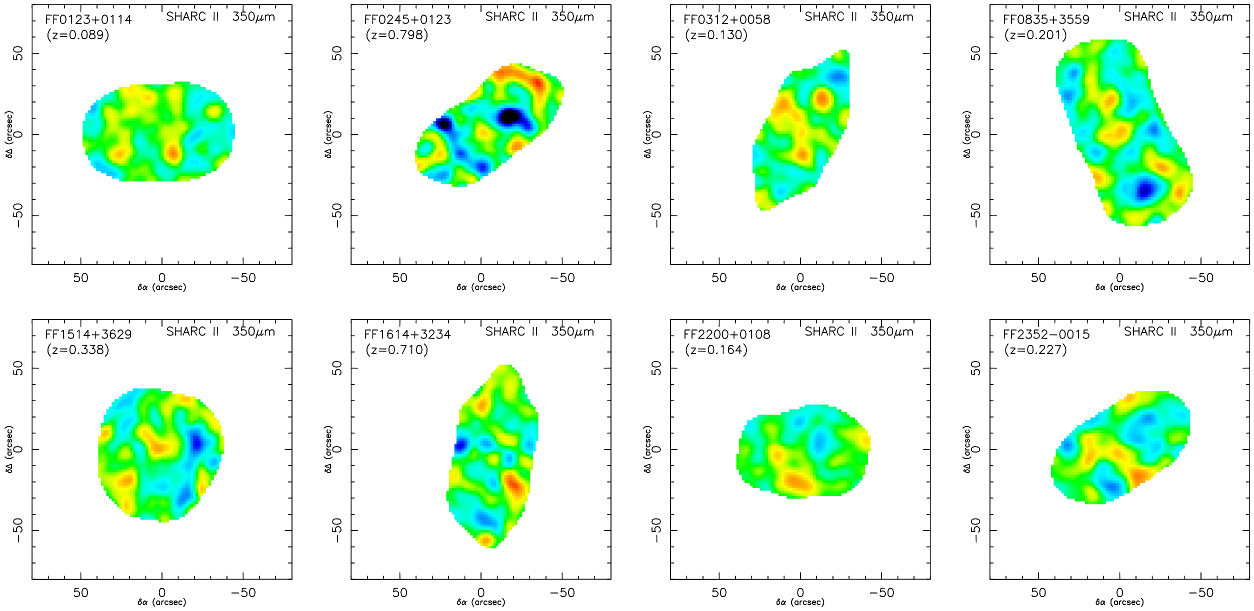

Figure 4.3 350 μm maps of FF sources not detected by SHARC-II (8).

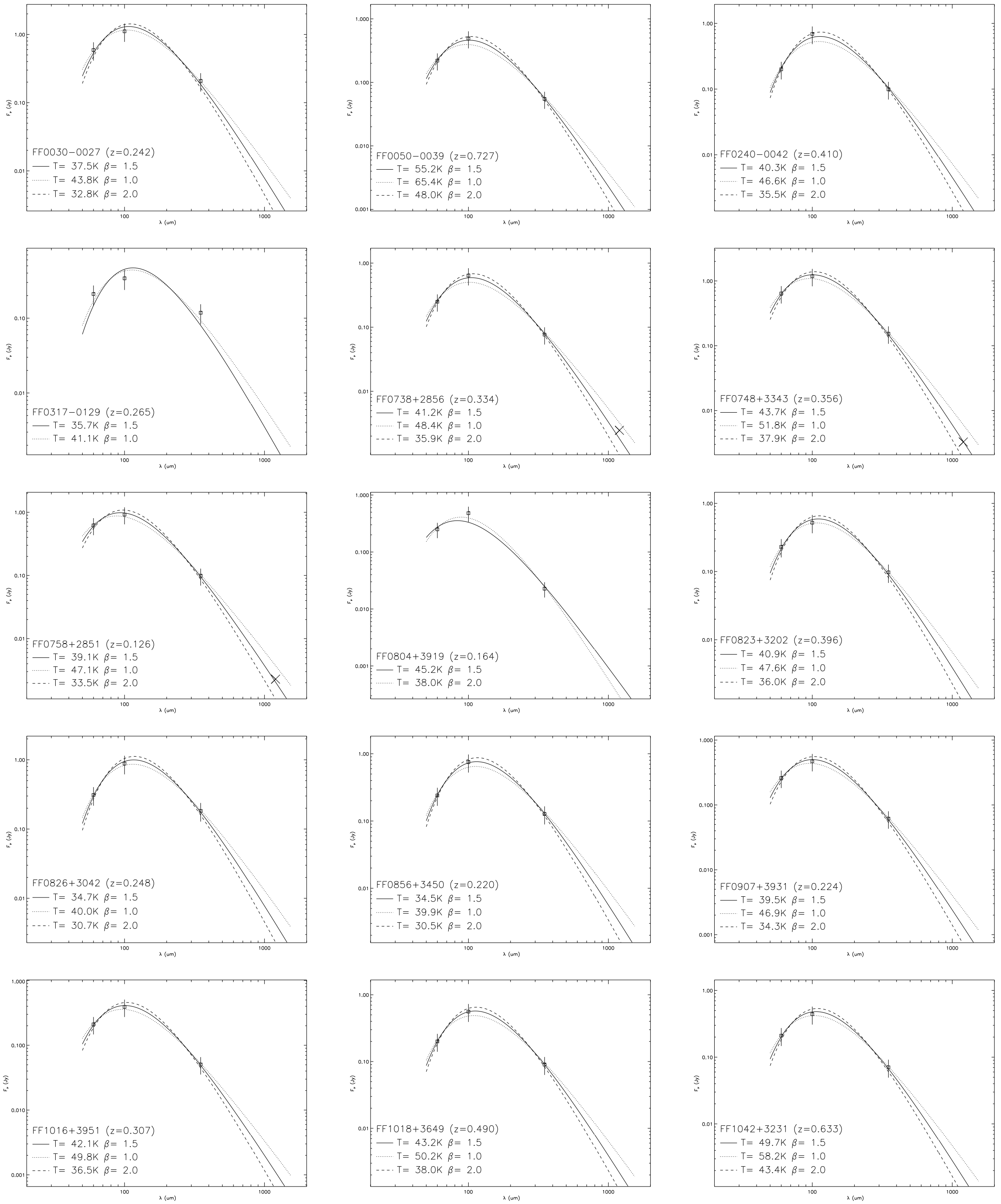

Figure 4.4 FIR/submm SED fits of FF sources detected by SHARC-II.

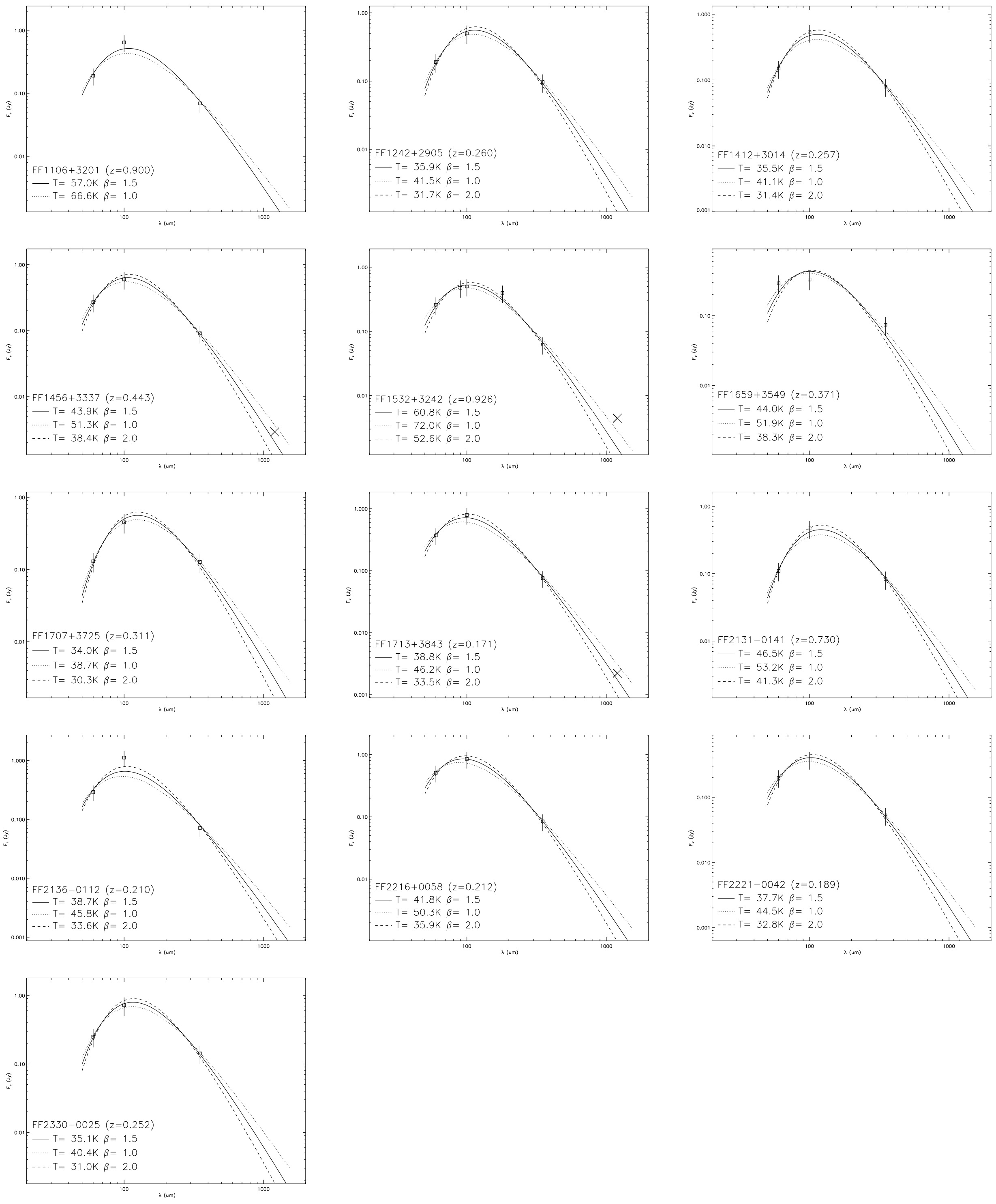

Figure 4.4 Continued

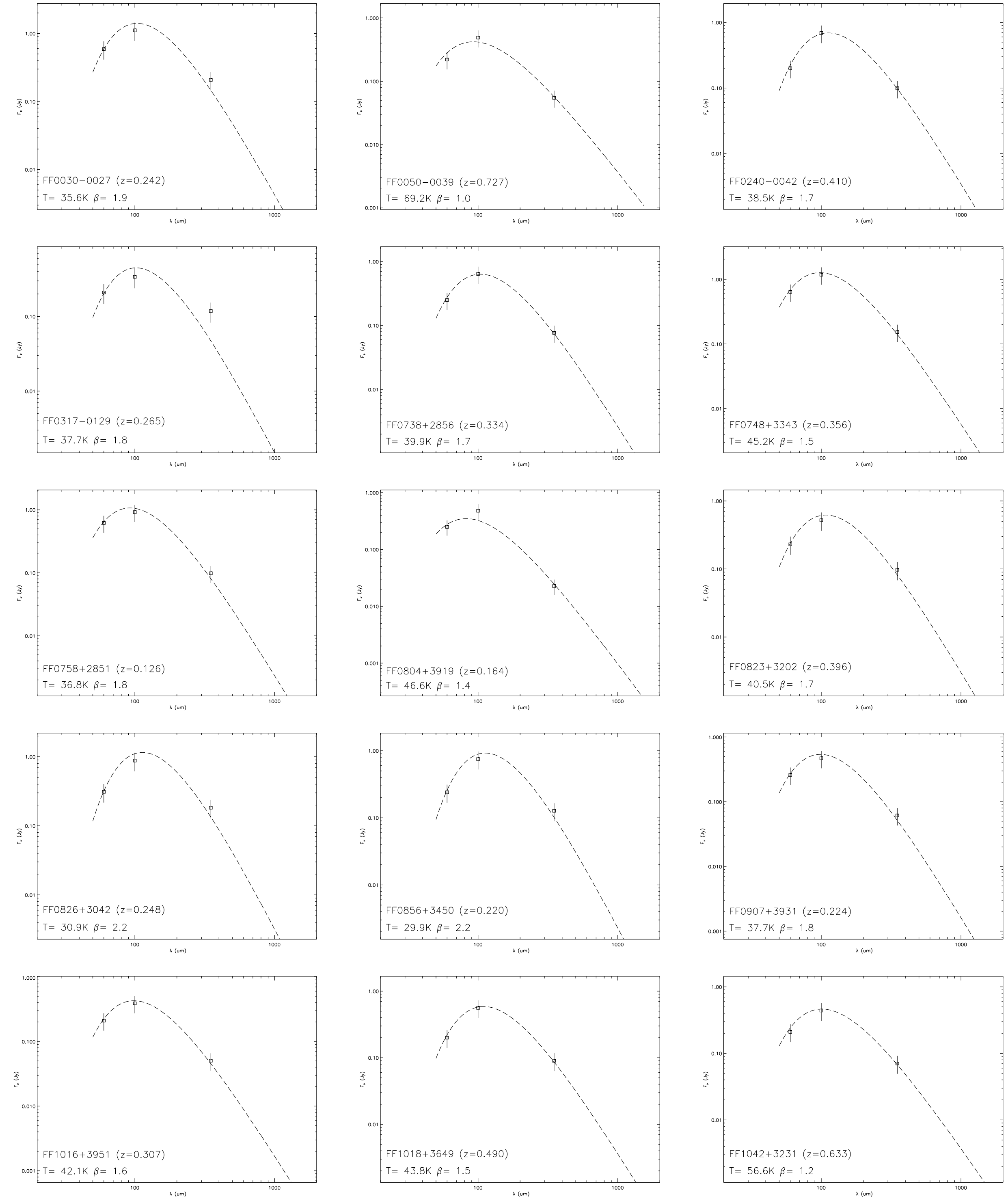

Figure 4.5 FIR/submm SED fits of FF sources detected by SHARC-II, assuming the $\mathrm{T_d}$ -β relation $\mathrm{T_d} = [5.03 \times 10^9]^{\frac{1}{4.46+\beta}}$.

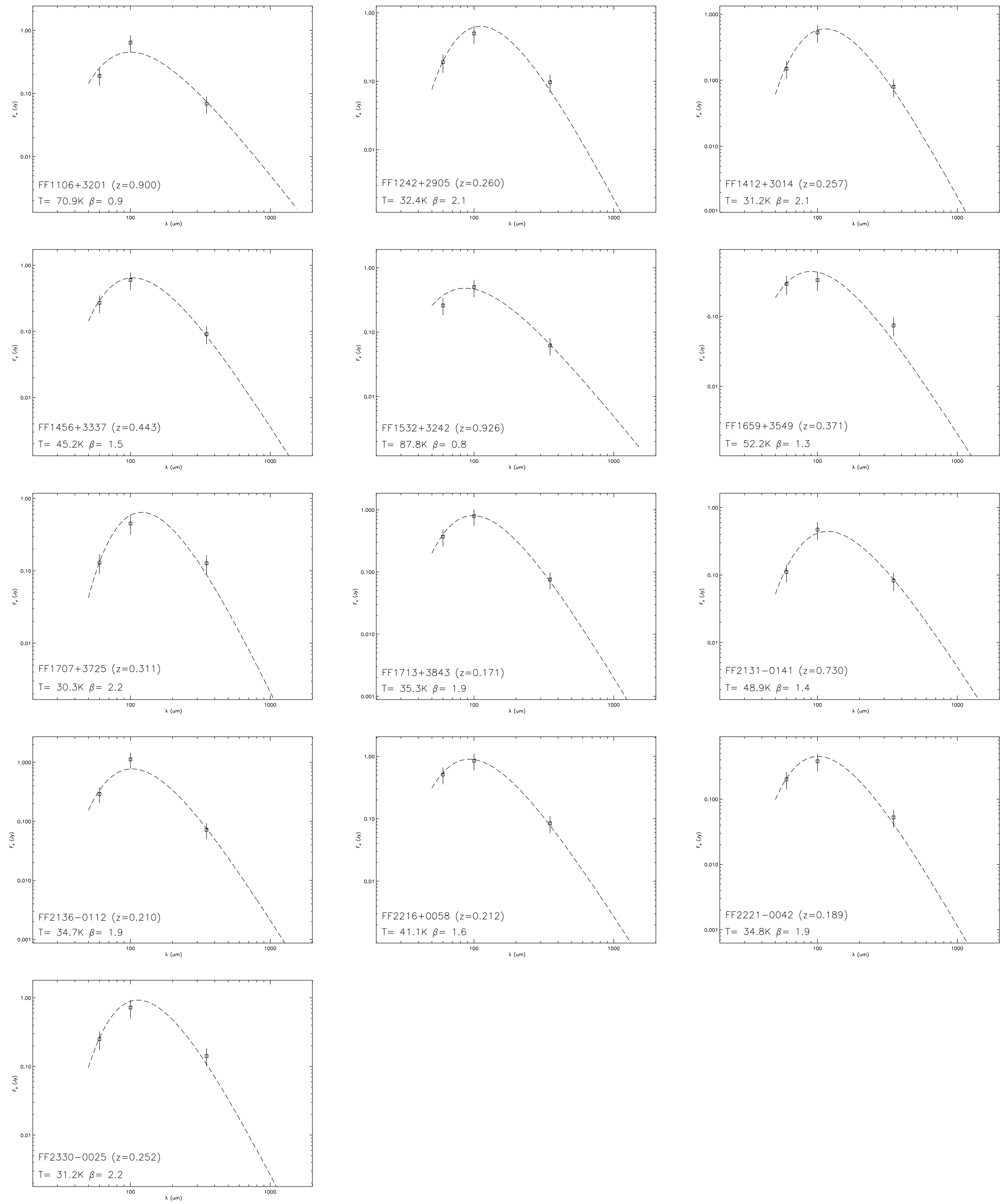

Figure 4.5 Continued

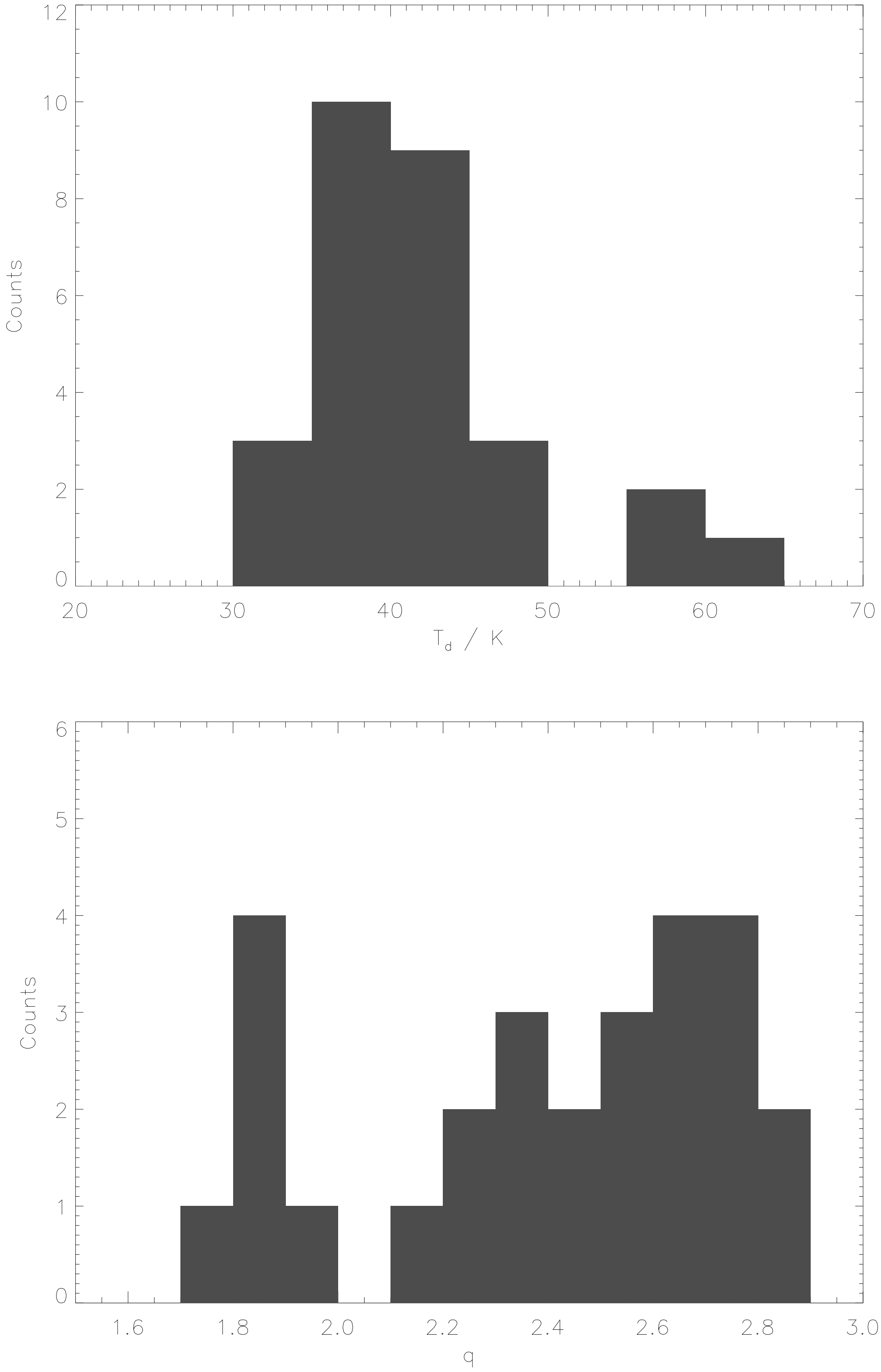

Figure 4.6 Histograms of T_d and q values derived for the SHARC-II detected FF sources.

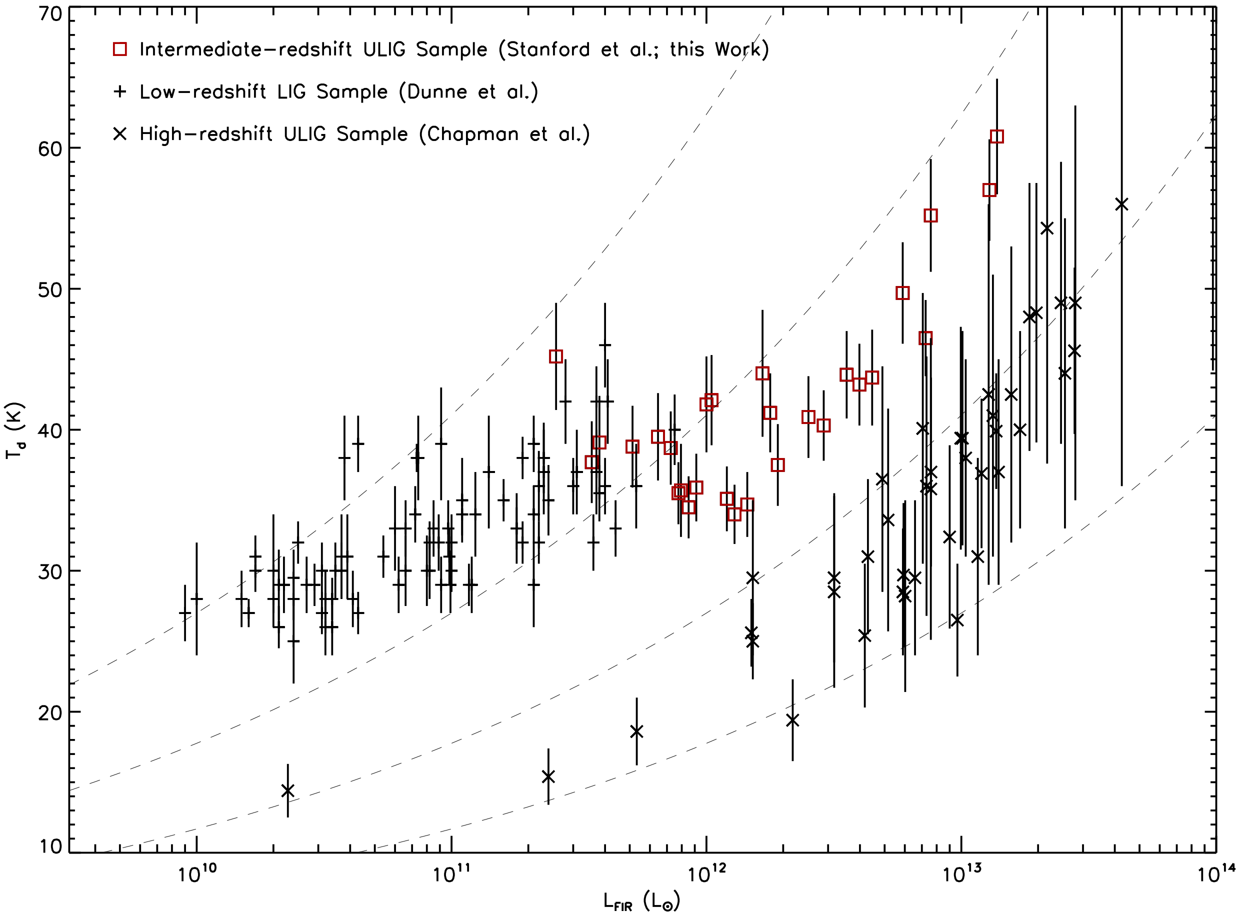

Figure 4.7 L_{fir} and T_d derived for luminous dusty galaxy samples at distinct redshifts. The dashed lines correspond to L_{fir} -T_d relations given by Eq. (4.12), assuming β =1.5 and $\kappa_{125\mu m} = 1.875\,(\mathrm{kg/m^2})^{-1}$, for dust mass spanning over 3 orders of magnitude $M_d = 10^{7-10}\,M_\odot$ (from top to bottom).

Appendix A

Instruments and Data Reduction

A.1 SHARC-II (Dowell et al. 2003)

Recent advancement in microelectronic fabrication techniques has allowed bolometers to be manufactured in very densely packed two-dimensional arrays. SHARC-II is one of such total power bolometer detector arrays, mounted on the 10.4 m telescope of the CSO, sited on Mauna Kea, Hawaii, at about 14,000-ft elevation. With a 32×12 bolometer packing and $\sim 85\%$ of the 384 bolometers functioning, SHARC-II is the largest detector currently in use at submm wavelengths. Optimized for conducting observations at 350 $\mu\mathrm{m}$, SHARC-II is equipped with three waveband filters - 350 $\mu\mathrm{m}$, 450 $\mu\mathrm{m}$, and 850 $\mu\mathrm{m}$ - that can be changed manually. With good focus and pointing, the CSO has a beam size of $\sim 8.5''$ (FWHM) at 350 $\mu\mathrm{m}$, while each SHARC-II pixel has an extent of $4.85''$. The high filling factor ($> 90\%$) in the SHARC-II bolometer array therefore allows approximate Nyquist sampling of the sky. Given its pixel size and two-dimensional pixel counts, SHARC-II has a field of view (FOV) of $2.59' \times 0.97'$.

The SHARC-II bolometer array is placed in a $^3\mathrm{He}$ cryostat, backed by liquid $^4\mathrm{He}$ and liquid N_2 cooled shields. It achieves background-limited performance at 350 $\mu\mathrm{m}$ with the noise equivalent flux density (NEFD) measured to be $\sim 1\,\mathrm{Jy\,s^{1/2}}$ under the conditions of $\tau_{225\,\mathrm{GHz}}$ = 0.05 and airmasses = 1.3. Assuming 50% overhead time loss, this corresponds to $\sigma = 24\,\mathrm{mJy}$ within one hour of observing time, as calculated by

$$\sigma = \frac{\mathrm{NEFD}}{\sqrt{0.5\,\mathrm{t}}}\,. \tag{A.1}$$

The NEFD under general conditions is given by

$$\mathrm{NEFD} \sim 1\,\mathrm{Jy\,s^{1/2}}\exp\left(25 \times \tau_{225} \times \mathrm{airmass} - 1.6\right). \tag{A.2}$$

A.2 The Dish Surface Optimization System (DSOS, Leong et al. 2003)

The 10.4 m CSO primary dish consists of 84 hexagonal segments. As the dish moves in elevation during observations, its surface suffers imperfections and gravitational deformations, leading to deterioration and variation in beam efficiency. The DSOS system is utilized with the goal of overcoming such ill effects.

The DSOS system consists of 99 steel rod standoffs that interface the dish panels to its backing structure. Each standoff is equipped with a heating/cooling assembly, which elongates or shortens the standoff through heating or cooling, resulting in push or pull on the dish panel. The dish surface can therefore be adjusted by collectively applying controlled potentials to the 99 assemblies, while the needed correction for each standoff at a given elevation is retrieved from stored holography maps of the dish surface.

The resulting improvement in aperture efficiency from utilization of the DSOS system is specially useful for SHARC-II observations. The aperture efficiency at 350 μm is measured to improve by a factor of ~ 1.5 when DSOS is correctly applied, leading to reduction in integration time by a factor of ~ 2. Additionally, as the beam efficiency experiences less variation with elevation, calibration estimates become more consistent and reliable.

A.3 SHARC-II Observing Mode

The primary observing mode of SHARC-II is scanning without chopping, though chopping can be occasionally applied for observing faint point sources and when the sky is highly variable. The full-power scanning mode, as compared to chopping, has the advantage of having twice as much on-source integration time, as well as not suffering an increase in noise due to the subtraction of off-source emission. However, the obvious disadvantage of full-power observing is that the task of estimating sky emission becomes much less straightforward from a data reduction point of view.

Two scanning routines - SWEEP and BOX - are supported for SHARC-II observations, which perform linear and curved controlled scans respectively. SWEEP is most appropriate for mapping areas of size comparable to the SHARC-II FOV ($2' \times 1'$) and for observing point sources. In this mode, the telescope, starting from the center of the map, modulates its X and Y position with sine waves following a Lissajous pattern. The offsets - dX and dY - are given by

$$\begin{aligned} \mathrm{dX(t)} &= \mathrm{A_X} \cos\left(2\,\pi\,\mathrm{t}/\mathrm{T_X}\right) && \text{(A.3)} \\ \mathrm{dY(t)} &= \mathrm{A_Y} \sin\left(2\,\pi\,\mathrm{t}/\mathrm{T_Y}\right), && \text{(A.4)} \end{aligned}$$

where $(\mathrm{A_X}, \mathrm{A_Y})$ are amplitudes and $(\mathrm{T_X}, \mathrm{T_Y})$ are periods in the two directions. Ratios of the periods $\frac{\mathrm{T_X}}{\mathrm{T_Y}}$ are irrational numbers to avoid periodic motion of the scans. This is necessary for separating sky noise at frequencies corresponding to $(\mathrm{T_X}, \mathrm{T_Y})$ with true astronomical signal. In contrast, BOX is more suitable for mapping areas of the sky significantly larger than the SHARC-II array size. In this mode, the telescope, starting from the center of the map, scans at an angle of 45° until it hits a boundary of the map, followed by change of direction with the angle of reflection equal to the angle of incidence.

A.4 $\tau_{225\,\mathrm{GHz}}$

Due to the large atmospheric transmission scaling factor between $\tau_{225\,\mathrm{GHz}}$ and $\tau_{350\,\mu\mathrm{m}}$ ($\sim$ 25), any uncertainty in $\tau_{225\,\mathrm{GHz}}$ has a much amplified effect on 350 μm flux estimates. The $\tau_{225\,\mathrm{GHz}}$ meter not only suffers measurement errors, but also scans the sky at the limited frequency of once every 10 minutes, causing large scatters in $\tau_{225\,\mathrm{GHz}}$ measurements. We therefore adopt polynomial fits (John Bird) of $\tau_{225\,\mathrm{GHz}}$ readings over the course of each observing night which are expected to give $\tau_{225\,\mathrm{GHz}}$ estimates more realistic than single measurements.

A.5 Pointing

Pointing corrections are especially important for recovering faint sources, for which long integration time is often required. In reducing data taken from different nights, and sometimes even different runs, inconsistent pointing errors could cause false non-detections or smeared images, thus need to be carefully corrected for. Pointing scans are taken frequently and regularly on bright submm sources over the course of all SHARC-II observing nights. Using pointing data thereby obtained, we adopt a pointing model that accounts for pointing shift as a function of source position (ZA, AZ), focus settings, temperature, and time (UT). Pointing data for science targets are then estimated following this pointing model, and subsequently given to the data reduction code as inputs.

A.6 Calibration

SHARC-II calibration scans are taken consistently on well known submm sources over a very wide range of weather conditions and airmass. Planets - particularly Mars, Uranus, and Neptune - are used as primary calibrators, while 350 μm fluxes of secondary calibrators - solar system objects, evolved stars, blazers and bright Galactic and extragalactic sources - are subsequently derived using calibration given by primary calibrators. Solar system objects have 350 μm fluxes that are highly variable and dependent on the distance from the Earth to the object and the distance from the Sun to the object, as given by

$$\begin{aligned} \mathrm{T_B} &= \frac{\mathrm{T_{1AU}}}{\sqrt{\mathrm{r}}} && \text{(A.5)} \\ \mathrm{S_{350}} &= \Omega\, \mathrm{B_{350}(T_B)}\,, && \text{(A.6)} \end{aligned}$$

where $\mathrm{T_B}$ is the source brightness temperature, $\mathrm{T_{1AU}}$ is the brightness temperature if the source were at heliocentric distance of 1 AU, as derived from SHARC-II measurements, r is the source heliocentric distance in the unit of AU, Ω is the solid angle of the source, and $\mathrm{B_{350}}$ is Planck function evaluated at 350 μm . Ω and r can be obtained from the JPL Horizons System (http://ssd.jpl.nasa.gov/horizons.cgi). Additionally, flux within the $9''$ beam can be significantly less than total flux for a source with large angular diameter. In such cases, the illumination fraction, also available from the JPL Horizons System, needs to be taken into account to estimate its true 350 μm flux.

Having established the true 350 μm fluxes of the calibrators, we reduce calibration scans and estimate their SHARC-II 350 μm fluxes. Comparison between the true fluxes and the instrumental fluxes leads to scaling factors appropriate for application in the data reduction of science scans. Calibration factors thereby obtained are expected to be accurate within 20% margin.

A.7 Comprehensive Reduction Utility for SHARC-II (CRUSH, Kovács 2006)

CRUSH is a java-based tool serving as the the primary data reduction package for the reduction of SHARC-II data. It takes, as inputs, lists of scan numbers and a wide variety of options, to produce a FITS file with four images - signal, noise, weight, and signal/noise. Particularly relevant to work presented in this thesis are the options “-faint” and “-deep”, which are optimal for recovering faint point sources that have 350 μm fluxes on the orders of Jy and 10 mJy respectively.

CRUSH solves for a series of statistical estimators in an iterative approach, with the help of well designed scanning patterns. In each iteration, a model is estimated within the context of more accurate concurrent models, and eventually converges to a self-consistent solution. CRUSH has the property that computation time scales linearly with data size; this is attractive given the large size of typical SHARC-II data files ($\sim 30\,\mathrm{Mb}$ per 10 minutes).

Appendix B

Absorption and Scattering in the Long Wavelength Limit

B.1 Basic Electromagnetic Theory

For monochromatic plane waves, the electromagnetic fields ($\vec{\mathrm{E}}$, $\vec{\mathrm{H}}$) are of the form

$$(\vec{\mathrm{E}}, \vec{\mathrm{H}}) \propto e^{i\,\vec{\mathrm{k}}\cdot\vec{r} - i\,\omega\,t}\,, \tag{B.1}$$

where $\vec{\mathrm{k}}$ is the wave vector. The Maxwell equations require that ($\vec{\mathrm{E}}$, $\vec{\mathrm{H}}$) satisfy the relations

$$\begin{aligned} \nabla^2\vec{\mathrm{E}} + \mathrm{k}^2\,\vec{\mathrm{E}} &= 0 & \text{(B.2)} \\ \nabla^2\vec{\mathrm{H}} + \mathrm{k}^2\,\vec{\mathrm{H}} &= 0\,, & \text{(B.3)} \end{aligned}$$

where $\mathrm{k} = \omega\sqrt{\varepsilon\,\mu}$, ε is the dielectric function, and μ is the permeability.

The Poynting vector, defined as $\vec{\mathrm{S}} \equiv \vec{\mathrm{E}} \times \vec{\mathrm{H}}$, measures the energy transfer rate crossing a surface per unit area. Given that

$$\begin{aligned} \vec{\mathrm{k}} &= \mathrm{k}\,\hat{e}_z & \text{(B.4)} \\ \vec{\mathrm{E}} &= \mathrm{E}_0\,e^{i\,\mathrm{k}\,\mathrm{z} - i\,\omega\,t}\,\hat{e}_x & \text{(B.5)} \\ \vec{\mathrm{H}} &= \frac{1}{i\,\omega\,\mu}\nabla \times \vec{\mathrm{E}} = \frac{\vec{\mathrm{k}} \times \vec{\mathrm{E}}}{\omega\,\mu}\,, & \text{(B.6)} \end{aligned}$$

the average of the Poynting vector over a long time interval varies as

$$\langle \vec{\mathrm{S}} \rangle \propto |\mathrm{E}|^2 \propto e^{-2\,\mathrm{Im}\,(\mathrm{k})\,\mathrm{z}}\,. \tag{B.7}$$

Hence, absorption arises when $\mathrm{Im}\,(\mathrm{k}) > 0$, with $2\,\mathrm{Im}\,(\mathrm{k})$ being the absorption coefficient. In other words, absorption is caused by internal displacements of electrical charges out of phase with the incident field. Extinction, on the other hand, arises from interference between incident and scattered light, i.e.

$$\langle \vec{\mathrm{S}}_{\mathrm{ext}} \rangle = \frac{1}{2}\,\mathrm{Re}\,(\vec{\mathrm{E}}_{\mathrm{i}} \times \vec{\mathrm{H}}^{*}_{\mathrm{scat}} + \vec{\mathrm{E}}_{\mathrm{scat}} \times \vec{\mathrm{H}}^{*}_{\mathrm{i}})\,, \tag{B.8}$$

where ($\vec{\mathrm{E}}_{\mathrm{i}}$, $\vec{\mathrm{H}}_{\mathrm{i}}$) and ($\vec{\mathrm{E}}_{\mathrm{scat}}$, $\vec{\mathrm{H}}_{\mathrm{scat}}$) characterize the electromagnetic fields of the incident and scattered light.

W, defined as $\mathrm{W} \equiv -\int_{\mathrm{A}} \vec{\mathrm{S}} \cdot d\vec{\mathrm{A}}$, measures the rate of electrodynamic energy transfer crossing the boundary of a closed surface A. Cross sections are defined as $\mathrm{C} \equiv \frac{\mathrm{W}}{\mathrm{I}_{\mathrm{i}}}$. Eq. (B.8) and boundary conditions which ensure the continuity of the tangent components of $\vec{\mathrm{E}}$ and $\vec{\mathrm{H}}$ lead to the relation $\mathrm{C}_{\mathrm{ext}} = \mathrm{C}_{\mathrm{abs}} + \mathrm{C}_{\mathrm{scat}}$.

B.2 Optical Theory - Lorenz and Drude Model

The magnetic response is generally negligible at wavelengths $\lambda < 3\,\mathrm{mm}$, magnetization of interstellar dust is thus ignored in the consideration of its thermal emission.

The *Lorentz* classical optical model treats electrons and ions in crystalline dielectrics as simple harmonic oscillators subject to the driving forces of the local field $\vec{\mathrm{E}}_{local}$. $\vec{\mathrm{E}}_{local}$ in general is not the same for all oscillators, but $\vec{\mathrm{E}}_{local} = \vec{\mathrm{E}}_i$ to the first order. A crystalline dielectric material is approximated by a collection of identical, independent, isotropic harmonic oscillators, each of which obeys

$$\ddot{\vec{x}} + \gamma\dot{\vec{x}} + \omega_0^2\vec{x} = e\vec{\mathrm{E}}_i\,, \tag{B.9}$$

where ω_0 is the resonant frequency, and $\gamma \equiv \frac{1}{\tau_0}$ (τ_0 is the damping time). The resonance frequencies of grain material generally lie in the NIR/MIR ($\lambda \leq 20\mu\mathrm{m}$), and damping is attributed to the non-harmonic term of the lattice potential. In the harmonic approximation $\frac{\mathrm{d}}{\mathrm{dt}} \sim (-\mathrm{i}\omega)$, the electric susceptibility is given by

$$\begin{aligned} \chi &= \frac{Ne\vec{\mathrm{x}}}{\varepsilon_0 \vec{\mathrm{E}}_i} && \text{(B.10)} \\ &= \frac{\omega_\mathrm{p}^2}{\omega_0^2 - \omega^2 - \mathrm{i}\gamma\omega}\,, && \text{(B.11)} \end{aligned}$$

where N is the number density and $\omega_\mathrm{p}^2 \equiv \frac{\mathrm{Ne}^2}{\mathrm{m}\varepsilon_0}$ is the plasma frequency. The complex dielectric function is given by

$$\begin{aligned} \epsilon &= 1 + \chi && \text{(B.12)} \\ &= 1 + \frac{\omega_\mathrm{p}^2}{\omega_0^2 - \omega^2 - \mathrm{i}\gamma\omega}\,. && \text{(B.13)} \end{aligned}$$

The real and imaginary parts of the complex dielectric function are

$$\begin{aligned} \epsilon' &= 1 + \frac{\omega_\mathrm{p}^2(\omega_0^2 - \omega^2)}{(\omega_0^2 - \omega^2)^2 + \gamma^2\omega^2} && \text{(B.14)} \\ \epsilon'' &= \frac{\omega_\mathrm{p}^2\gamma\omega}{(\omega_0^2 - \omega^2)^2 + \gamma^2\omega^2}\,. && \text{(B.15)} \end{aligned}$$

In the FIR/submm spectral region, which usually satisfies

$$\omega \ll \omega_0\,, \tag{B.16}$$

Eqs. (B.14) and (B.15) become

$$\begin{aligned} \epsilon' &= 1 + \frac{\omega_\mathrm{p}^2}{\omega_0^2} = \epsilon(0) && \text{(B.17)} \\ \epsilon'' &= \frac{\gamma\omega_\mathrm{p}^2\omega}{\omega_0^4}\,, && \text{(B.18)} \end{aligned}$$

where $\epsilon(0)$ is the dielectric function at 0 frequency. This low frequency behavior of the dielectric function in crystalline dielectrics - ϵ' being nearly constant, $\epsilon'' \propto \omega$, and $\epsilon'' \ll \epsilon'$ - is confirmed by laboratory measurements of lunar rocks and H_2O ice.

By contrast, the optical properties of conducting materials are drastically different from those of dielectrics. Electrons are "free", as they can easily be excited into states that have similar energy levels but different momenta. This effectively removes the "springs" from the oscillators and sets ω_0 to 0 in Eqs. (B.14) and (B.15). This is the so-called *Drude* model, in which Eq. (B.13) becomes

$$\epsilon = 1 - \frac{\omega_{\rm p}^2}{\omega^2 + {\rm i}\gamma\omega} . \tag{B.19}$$

And Eqs. (B.14) and (B.15) become

$$\begin{aligned} \epsilon' &= 1 - \frac{\omega_{\rm p}^2}{\omega^2 + \gamma^2} & \text{(B.20)} \\ \epsilon'' &= \frac{\omega_{\rm p}^2 \gamma}{\omega(\omega^2 + \gamma^2)} , & \text{(B.21)} \end{aligned}$$

where $\gamma \equiv \frac{1}{\tau_{\rm c}}$, $\tau_{\rm c}$ is the mean free time of conducting electrons, and $\omega_{\rm p}$ is the electron plasma frequency. Wooten (1972) estimates $\omega_{\rm p} \sim 1.0 \times 10^{15}$ Hz and $\gamma \sim 1.0 \times 10^{14}$ Hz for typical metals, we thus have $\omega \ll \gamma \ll \omega_{\rm p}$ in the FIR/submm spectral region. Eqs. (B.20) and (B.21) become

$$\begin{aligned} \epsilon' &= 1 - \frac{\omega_{\rm p}^2}{\gamma^2} & \text{(B.22)} \\ \epsilon'' &= \frac{\omega_{\rm p}^2}{\omega\gamma} . & \text{(B.23)} \end{aligned}$$

Note that the real and imaginary parts of the complex dielectric function ϵ are not independent. ϵ' and ϵ'' are connected by the Kramer-Kronig relations (Bohren & Huffman 1983), which are universally applicable for any linear causal response function. If either is known at all frequencies, the other is fully determined.

Appendix C

CO Observation of M83

Here we present observations of carbon monoxide (CO) emission along the inner eastern spiral arm of the barred starburst galaxy M83.

C.1 Background

C.1.1 CO Emission as a Tracer of $\mathrm{H_2}$ Mass

$\mathrm{H_2}$ molecules are symmetric and have no electric dipole moment. The lowest $\mathrm{H_2}$ quadrupole line occurs at the mid-infrared wavelength of 28 $\mu\mathrm{m}$, requiring an excitation temperature $\geq$500 K . Consequently, $\mathrm{H_2}$ molecules simply do not radiate in molecular clouds where the temperature is typically cold at 10$\sim$20 K . Instead, the best tracer is provided by the second most abundant gas molecules in the ISM, i.e. CO. With its small dipole, a CO molecule is easily excited in its rotational lines, which falls in the millimeter wavelength range, corresponding to excitation temperature $\geq$5 K . Observations of CO transitional lines are thus well suited to probe the usually cold environments in molecular clouds. The most commonly used CO lines are generally optically-thick at 2.6 mm ($\mathrm{J} = 1-0$) and 1.3 mm ($\mathrm{J} = 2-1$). However, velocity gradients among individual sub-structures within a giant molecular cloud (GMC) prevent they from hiding one another at any given velocity. Therefore the overall optically depth is not necessarily large in CO observations toward a GMC, allowing estimate of total $\mathrm{H_2}$ mass from its CO luminosity $\mathrm{L_{CO}}$ (or equivalently estimate of $\mathrm{H_2}$ column density from the observed CO brightness $\mathrm{I_{CO}}$).

The theoretical basis for this simple relation is derived as follows.

$$\mathrm{I_{CO}} = \int \mathrm{T_{CO,V}}\,\mathrm{dV} = \mathrm{T_{CO}}\,\Delta\mathrm{V}\,, \tag{C.1}$$

where $\mathrm{T_{CO}}$ is the peak brightness temperature and $\Delta\mathrm{V}$ is the line width. In the simplifying case of a uniform, spherical cloud in virial equilibrium

$$\Delta\mathrm{V} = \sqrt{\mathrm{G\,M_{H_2}/R}}\,, \tag{C.2}$$

where $\mathrm{M_{H_2}} = \rho\,\frac{4}{3}\,\pi\,\mathrm{R}^3$ is the mass of the cloud, R is the radius and ρ is the density of the cloud. Eq. (C.1) becomes

$$\begin{aligned} \mathrm{I_{CO}} &= \mathrm{T_{CO}}\sqrt{\frac{3\,\mathrm{G}}{4\,\pi\,\rho}\,\frac{\mathrm{M_{H_2}}}{\mathrm{R}^2}} & \text{(C.3)} \\ &= \mathrm{T_{CO}}\sqrt{\frac{3\,\pi\,\mathrm{G}}{4\,\rho}}\,\mathrm{N\,m_{H_2}}\,, & \text{(C.4)} \end{aligned}$$

where $\mathrm{m_{H_2}}$ is the unit mass of a hydrogen molecule, and $\mathrm{N} = \frac{\mathrm{M_{H_2}}}{\mathrm{m_{H_2}}\,\pi\,\mathrm{R}^2}$ is the $\mathrm{H_2}$ column density when clouds along a line of sight are not overlapped in space or velocity. Thus

$$\mathrm{N} = \mathrm{I_{CO}} \times \sqrt{\frac{4\,\rho}{3\,\pi\,\mathrm{G}}}\,\frac{1}{\mathrm{T_{CO}\,m_{H_2}}}\,. \tag{C.5}$$

Equivalently,

$$\mathrm{M_{H_2}} = \mathrm{L_{CO}} \times \sqrt{\frac{4\,\rho}{3\,\pi\,\mathrm{G}}}\,\frac{1}{\mathrm{T_{CO}}}\,. \tag{C.6}$$

The conversion factor varies as $\frac{\sqrt{\rho}}{\mathrm{T_{CO}}}$. Although observational evidence indicates the existence of multiple cloud populations that are very different in properties , $\frac{\sqrt{\rho}}{\mathrm{T_{CO}}}$ has been found to remain relatively uniform across these populations (Turner et al. 1990).

The simple relation between $\mathrm{M_{H2}}$ and $\mathrm{L_{CO}}$ has been tested and confirmed by a number of CO observations of GMCs in the Milky Way (Scoville et al. 1987, Solomon et al. 1987) and external galaxies (Vogel et al. 1987, Wilson & Scoville 1990, Wilson & Reid 1990) where high spatial resolution ($\leq$40 pc) have been achieved. An extremely close correlation has been found between $\mathrm{L_{CO}}$ and virial masses of the molecular clouds, and the best-fitting constant of proportionality is estimated to be $\mathrm{X_{Gal}} = 2.8 \times 10^{20}\,\mathrm{cm^{-2}/K\,km\,s^{-1}}$ in Galactic GMCs.

C.1.2 M83

M83 (NGC5236) is one of the nearest barred spiral galaxies with extremely bright molecular emission. With its large angular size, prominent bar, well-defined global spiral structure and high star formation rate, it has been a popular candidate for observers to study and test star-formation and dynamics models. Consequently there exist a wealth of observation data sets in the literature, building upon which we hope to address a few interesting topics. In particular, this project attempts to follow up the results presented by Rand et al. (1999). Global properties of M83 are summarized in Table C.1.

C.2 Observation and Data Reduction

We observed M83 along its inner eastern spiral arm in the $^{12}\mathrm{CO}\,(\mathrm{J}=2-1)$ emission line at the CSO over seven separate runs from June 2000 to April 2002. A Nyquist sampled 9×15 point map was obtained, covering a region of 128″ by 224″ (3.1×5.4 kpc).

At the $^{12}\mathrm{CO}\,(\mathrm{J}=2-1)$ transition line (230 GHz), CSO has a Gaussian beam with 32″ FWHM. The map spacing was 16″ in both the Right Ascension and Declination directions. Pointing was checked about every 1.5 hours, using nearby planets or CO bright stars. System temperatures $\mathrm{T_{sys}}$ ranged from 300 K to 1200 K and were typically below 700 K . The atmospheric conditions were fairly good for most runs, with a typical zenith water vapor of $\tau_{225\,\mathrm{GHz}}$ = 0.05~0.25, wind speeds ~10 mph, and humidities ~10%. The intergration time for each map point ranged from 10 minutes to two hours, depending on the source emission strength. Good signal to noise ratios were achieved in general, ranging from 2 to 70, with 3σ or better detections at 95% of the positions.

The receiver used for the observations was a SIS with a 1024 channel acousto-optical spectrometer providing a frequency coverage of 500 MHz and a velocity resolution of $0.6\,\mathrm{km\,s^{-1}}$. Spectral emission within the LSR velocity range of $300{\sim}700\,\mathrm{km\,s^{-1}}$ were analyzed, using the software package CLASS. Each spectrum was baseline subtracted, by using a 2nd or 3rd order polynomial fit to the line-free channels. For each position, all baseline-subtracted spectra were co-added, weighted by noise. We noticed an anomalous velocity shift in the spectra taken during last run (April 2002), and a sky frequency offset was present in the data. The occurrence of frequency offset had been noticed before at the CSO. We determined, through repeated observations of the central position of M83 during each run, that the $\mathrm{V_{cen}} = 506\,\mathrm{km\,s^{-1}}$, which is also in good agreement with similar observations (Crosthwaite et al. 2002). We determined that only during the April 2002 run was the frequency offset present, and corrected for it accordingly, shifting all spectra obtained in April 2002 by $8.5\,\mathrm{km\,s^{-1}}$ to the blue before averaging. The telescope beam efficiency for the 230 GHz receiver was measured to be 0.7 at CSO in March 2001; during other runs, the beam efficiency varied 20% from this value. The main beam efficiency η_{mb} on average equals to 0.7, although we found out it varied over different runs. This variation was corrected for the observations made in each run, as described below. Therefore, observed intensity at the galaxy center in March 2001 was used as the reference point; spectra from all other runs were then scaled to match the same intensity ($\mathrm{T_{peak}} = 1.23\,\mathrm{K}$) at the central position during the March 2001 run. After averaging spectra for each position, baselines of 1st order were subtracted a second time and the rms noise values were recorded. We determined the integrated flux, 1st-moment velocity (centroid), and line width (FWHM) within each spectral line. The integrated fluxes, on average, carry a 20% uncertainty, due to uncertainties in baseline substractions. The results are tabulated in Table C.2. Column 1 is the offset position from the center, in unit of arcsec; the coordinates used for the center are RA = $13^h37^m00.7^s$, Dec = $-29^\circ51'58''$ (J2000).

We also obtained data at $^{12}\mathrm{CO}\,(\mathrm{J}=3-2)$ (345 GHz) and $^{13}\mathrm{CO}\,(\mathrm{J}=2-1)$ (230 GHz) for certain selected positions during the runs of June 2001 and April 2002. CSO has a resolution of 24″ and a main beam efficiency of η_{mb} = 0.75 at 345 GHz. At the $^{13}\mathrm{CO}\,(\mathrm{J}=2-1)$, the main beam efficiency is essentially the same as that for $^{12}\mathrm{CO}\,(\mathrm{J}=2-1)$. Similar $\mathrm{T}_{\mathrm{sys}}$ and atmospheric conditions applied for these two additional lines, except that much lower $\tau_{225\,\mathrm{GHz}}$ conditions were utilized for the $^{13}\mathrm{CO}\,(\mathrm{J}=2-1)$ observations, due to its relative weakness. The same data reduction procedures were followed for these two data sets, and beam efficiency variations were likewise corrected using repeated observations of the central position. No anomalous velocity shift was encountered during $^{12}\mathrm{CO}\,(\mathrm{J}=3-2)$ observations in April 2002. The $^{12}\mathrm{CO}\,(\mathrm{J}=3-2)$ and $^{13}\mathrm{CO}\,(\mathrm{J}=2-1)$ results are tabulated in Tables C.3 and C.4.

Throughout Tables C.2 and C.4, $\mathrm{F}^{*}_{\mathrm{int}}$ and $\mathrm{T}^{*}_{\mathrm{peak}}$ are given without being corrected by η_{mb} ; true $\mathrm{F}_{\mathrm{int}}$ = $\mathrm{F}^{*}_{\mathrm{int}}$ $/\eta_{\mathrm{mb}}$ and true $\mathrm{T}_{\mathrm{peak}}$ = $\mathrm{T}^{*}_{\mathrm{peak}}$ $/\eta_{\mathrm{mb}}$.

C.3 Results

C.3.1 $^{12}\mathrm{CO}\,(\mathrm{J}=2-1)$

Fig. C.1 plots the observed $^{12}\mathrm{CO}\,(\mathrm{J}=2-1)$ spectra normalized to unity height; emission is detected everywhere in the observed regions of M83. This is the most sensitive CO map of M83 taken to date at a sensitivity $\mathrm{T}^{*}_{\mathrm{r}}$ $\leq$20 mK in a 32″ beam. Fig. C.2 shows the $^{12}\mathrm{CO}\,(\mathrm{J}=2-1)$ integrated flux map. A bright nucleus is evident, as well as the northeastern half of the stellar bar. The eastern spiral arm starts at the northeastern bar end and is traced fully for 2.7 kpc to the south. The spiral arm is very well-formed, extending about 0.5′ in width. There are variation in brightness along the arm, and there exists a bridge-like structure connecting the galaxy nucleus and the far southern end of the arm. One of the primary results of our observations is the spatially resolved mapping of arm and interarm, and CO emission was detected throughout the interarm regions at $\geq 3\sigma$ level for the first time in M83. Between the central bar and the eastern arm, the interarm region opens up to a width of ∼48″ . With CSO 32″ beam (FWHM) at 230 GHz, we are able to resolve and map arm and interarm regions. The arm-interarm $^{12}\mathrm{CO}\,(\mathrm{J}=2-1)$ emission contrast is seen to be in the range of 2∼3.

C.3.2 $^{12}\mathrm{CO}\,(\mathrm{J}=3-2)$ and $^{13}\mathrm{CO}\,(\mathrm{J}=2-1)$

Fig. C.3 (top panel) displays $^{12}\mathrm{CO}\,(\mathrm{J}=3-2)$ spectra normalized to unity height at the 14 observed positions, with beam locations shown by the side of the spectra. $^{12}\mathrm{CO}\,(\mathrm{J}=3-2)$ line was detected at all positions. The nucleus and the bar positions are seen to be bright; $\mathrm{F_{int}}$ = 177 K kms^{-1} is seen at the nucleus. In addition to positions centered on the nucleus and the spiral arm, we mapped a strip of positions crossing the eastern arm, sequenced interarm→arm→outer-arm, following offset positions: (48″ , -64″), (64″ , -80″), (80″ , -96″) and (96″ , -112″). There are strong detections ($\geq 3\sigma$) all along this strip, except at (96″ , -112″), where a 2σ detection is achieved. Interarm emission is clearly detected, and the $^{12}\mathrm{CO}\,(\mathrm{J}=3-2)$ emission arm-interarm contrast is estimated to be 2∼3, similar to that found for the $^{12}\mathrm{CO}\,(\mathrm{J}=2-1)$ line. Since the interarm region has a scale of 48″ , and at 345 GHz the CSO beam (FWHM) width is 24″ , we can rule out the possibility that the interarm detection is largely due to contamination from arm emission, and we argue that the interarm is effectively resolved. Moreover, the similarity between the arm vs. interarm contrast seen at $^{12}\mathrm{CO}\,(\mathrm{J}=3-2)$ and $^{12}\mathrm{CO}\,(\mathrm{J}=2-1)$ suggests that arm emission contamination is unlikely to be an important factor at 230 GHz either. $^{12}\mathrm{CO}\,(\mathrm{J}=3-2)$ vs. $^{12}\mathrm{CO}\,(\mathrm{J}=2-1)$ flux ratios at individual positions range from 0.7 to 1.6, with the lower ratios (≤1) seen in the interarm, the intermediate ratios (∼1) seen in the spiral arm, and the higher ratios (≥1) seen at the nucleus and at the bar end.

We observed the galaxy center and the bar end at the $^{13}\mathrm{CO}\,(\mathrm{J}=2-1)$ transition line. Fig. C.3 (bottom panel) shows the spectra normalized to unity height at these two positions. The $^{13}\mathrm{CO}\,(\mathrm{J}=2-1)$ line is detected ($\geq 6\sigma$) at each position. The

^{12}CO$\,(\mathrm{J}=2-1)$ vs. ^{13}CO$\,(\mathrm{J}=2-1)$ flux ratio is estimated to be 10$\sim$15, with a higher ratio seen at the nucleus than at the bar end.

C.3.3 Fraction of Single-dish Flux Recovered Interferometrically

We compare our ^{12}CO$\,(\mathrm{J}=2-1)$ single-dish flux with ^{12}CO$\,(\mathrm{J}=1-0)$ interferometer flux (Rand et al. 1999), assuming line intensity ratio $\mathrm{L}_{\mathrm{CO}_{2-1}}/\mathrm{L}_{\mathrm{CO}_{1-0}}\sim 1$. The interferometer data have been convolved to match the 32″ resolution before division. Fig. C.4 displays the ratio contours, and the average ratio has a value of $\sim$5%, in good agreement with fraction estimated by Rand et al. (1999). Such an unusually low overall fraction of CO flux picked up by interferometric observations suggests that the distribution of H_2 gas in M83 is fairly smooth and extended. The relative nearness of M83 also contributes to its molecular distribution being ″resolved-out″ by interferometer maps lacking zero spacing. Rand et al. (1999) estimate a ^{12}CO$\,(\mathrm{J}=1-0)$ arm-interarm contrast greater than 2.3, and we estimate that arm-interarm emission contrasts in both ^{12}CO$\,(\mathrm{J}=2-1)$ and ^{12}CO$\,(\mathrm{J}=3-2)$ fall within the range of 2$\sim$3. The very similar arm-interarm contrasts seen at these three transitional lines suggest that the bulk of the ISM in M83 is warm and diffuse - a scenario also supported by the detected interarm emission in all these three lines. We notice that the ratios are higher in the northern part of the arm than in the southern part, suggesting clumpier gas distribution in the northern segment of the arm.

C.3.4 Comparison with Other Tracers

In Fig. C.5 (top panel) we plot contours in other tracers - HI 21 cm , Hβ (Tilanus & Allen 1993) and 20 cm nonthermal radio continuum emission (Deutsch & Allen 1993) - superimposed on our ^{12}CO$\,(\mathrm{J}=2-1)$ map. The original 12″ HI map, 4″ Hβ map and 10″ nonthermal radio continuum map are convolved to match the CSO single-dish resolution of 32″ at the ^{12}CO$\,(\mathrm{J}=2-1)$ line.

HI emission coincides extremely well with CO emission throughout the observed region, except that HI is depleted at the galaxy center despite peak CO brightness. Moreover, HI peak emission lays slightly downstream from CO peak emission along the spiral arm. An arm-interarm HI emission contrast is estimated to be 2∼3. Hβ emission and non-thermal emission both coincide well with CO emission. It seems that HII arm, like HI arm, lays slightly downstream from CO spiral arm. We acknowledge that morphological features seen at a resolution of 32″ can be oversimplified.

C.4 Discussion

C.4.1 Molecular and Atomic Hydrogen; Photo-dissociation

Photodissociation scenario described by Tilanus and Allen (1993) suggests that molecular hydrogen dominates in number over atomic hydrogen in the dust lanes; hydrogen molecules get partly dissociated into HI by UV radiation near HII regions, thus from a HI ridge downstream. Our data support such a scenario in M83. Ratio map of L_{HI}/L_{CO}, both single-dish fluxes, is plotted in Fig. C.5 (bottom panel). Except near the galaxy center and downstream from the southern segment of the eastern arm, most regions have similar L_{HI}/L_{CO} ratios, including arm and interarm regions. Under the assumption that L_{HI} and L_{CO} respectively trace atomic gas density and molecular gas density, smooth L_{HI}/L_{CO} ratios suggests the relative abundance of atomic and molecular hydrogen M_H/M_{H_2} remains relatively uniform throughout most of the ISM in the observed regions of M83, and these two gas components mix well in large scale. Gas in the spiral arm is almost certain to be molecular, thus hydrogen gas is probably predominantly molecular throughout most of the ISM, including the interarm regions. The occurrence of peak M_H/M_{H_2} ratios downstream from the CO arm is expected from the photodissociation model. Active star-formation activity of OB stars in the arm, manifested by bright Hβ emission, emits strong UV radiation to partly dissociate hydrogen molecules into hydrogen atoms as molecular clouds pass through the arm and move downstream, causing $\mathrm{M_H/M_{H_2}}$ ratios to peak downstream. The very low $\mathrm{M_H/M_{H_2}}$ ratios near the galaxy center, on the other hand, can be understood by the extremely high gas density at the center that makes hydrogen preferentially stay in molecular form rather than atomic form.

C.4.2 Heating; Interpretation of Observed CO Brightness

Observed CO emission brightness $\mathrm{L_{CO}}$ is commonly assumed to be a fair tracer of molecular gas column density N(H_2), namely N(H_2) = $\mathrm{X\,L_{CO}}$ (X: the X factor, in unit of $\mathrm{cm^{-2}/K\,km\,s^{-1}}$). However, this simple relationship is not free of uncertainty. Deutsch and Allen (1993) suggested that heating provided by cosmic rays penetrating the ISM can greatly enhance CO emission brightness, thus $\mathrm{L_{CO}}$ does not reflect N(H_2), but rather effects of cosmic-ray heating. Lord and Kenny (1991), in attempt to explain observed deviation of CO peak emission from the dust lane, suggested UV heating from newly formed stars can also highlight CO emission. To what extend CO emission is affected by heating mechanisms (e.g. cosmic rays and UV photons) in relevance to gas density poses an interesting question. In the case of M83, we investigate the effects of cosmic-ray heating and UV heating on observed CO brightness by comparing nonthermal radio emission and Hβ emission relative to CO emission. Flux ratios of Hβ and nonthermal radio emission vs. CO emission, $\mathrm{L_{H\beta}/L_{CO}}$ and $\mathrm{L_{NT}/L_{CO}}$, are shown in Fig. C.5 (bottom panel). The very different characteristics shown in the flux ratio maps indicate fundamentally different ways in which UV radiation and cosmic rays affect excitation of CO molecules in the ISM of M83.

$\mathrm{L_{H\beta}/L_{CO}}$ brightness ratio peaks along the spiral arm of M83, which is understood by enhanced star formation efficiency in dense regions. UV radiation from star-formation sites suffers high extinction by dust grains, thus heating by UV photons, if significant at all, is probably limited and spatially restricted.

By contrast, flux ratio $\mathrm{L_{NT}/L_{CO}}$ appears almost uniform with the exceptions of the galactic center and southern end of the spiral arm, suggesting a strong correlation between L_{NT} and L_{CO} in a large part of the ISM of M83. The observed ubiquitousness of nonthermal radio emission, and by implication cosmic rays, throughout the ISM of M83, is also supportive of our previous assertion that the ISM in M83 is warm and diffuse. The abundance of cosmic rays in the ISM of M83 is not surprising. M83 - a late-type starburst spiral galaxy - has been frequently observed to have supernovae explosions, in which enormous amount of cosmic ray particles are released. These cosmic rays, subject to influence by interstellar magnetic fields, usually escape their SNRs and fill the disk and halo. Consequently nonthermal radio emission is smoothed and spread throughout the ISM, while discrete SNRs emit a negligible fraction of nonthermal radio flux. We argue that CO emission is excited by the combined contributions from molecular gas density and cosmic-ray heating, with $N(H_2)$ generally being the more likely dominant factor based on theoretical consideration and empirical evidence. However, in the ISM of M83 and possibly other late-type starburst galaxies, the observed CO brightness is probably enhanced considerably by comic-ray heating. In such cases, conversion factors lower than the Galactic value X_{gal} should be adopted to derive the mass of the molecular gas from the observed CO brightness. The relative importance of molecular gas density and cosmic-ray heating in principle depends on the virialization states of GMCs and the physical environments, particularly supernova activities and magnetic fields. Future high-resolution CO line and radio continuum observations of GMCs in a representative sample would further our understanding on this issue.

C.5 Conclusion

We have obtained a high sensitivity ^{12}CO $(J = 2-1)$ map of M83 along its inner eastern spiral arm. Molecular gas is detected in between the well defined spiral arms at $3\geq\ \sigma$ level for the first time. An arm-interarm contrast is estimated to be 2$\sim$3. Interarm emission is also detected in the ^{12}CO $(J = 3-2)$ transition line, showing a similar arm-interarm contrast.

Table C.1. Physical parameters of M83

		Reference
Type	SAB(s)c	1
Right Ascension(2000.0)	$13^h37^m00.7^s$	2
Declination(2000.0)	$-29^\circ51'58''$	2
Heliocentric systemic velocity[1]	$505\,\mathrm{km\,s^{-1}}$	3
Distance[2]	5.0 Mpc	4
Linear scale	$1'' = 24$pc	
Inclination	24°	5
Position angle of major axis	45°	5

References. — (1)de Vaucouleurs et al. 1991; (2)Cowan et al. 1994; (3)Comte 1981; (4)Kennicutt 1988; (5)Talbot et al. 1979.

We compare our single-dish CO fluxes with CO fluxes detected by interferometers. The overall fraction of single-dish flux detected by interferometric observations is unusually low at ∼5% level, suggesting a fairly smooth distribution of the ISM in M83.

We compare the CO line emission with other tracers observed in M83. The HI arm is displaced downstream from the CO arm, as can expected from the photodissociation model. The relative abundance of atomic and molecular hydrogen $\mathrm{M_H/M_{H_2}}$ remains almost constant throughout most of the ISM, including in the interarm regions.

The CO emission correlates better with the nonthermal radio continuum emission than with the Hβ emission. In particular, there appears a strong positive linear correlation between $\mathrm{L_{NT}}$ and $\mathrm{L_{CO}}$ throughout most of the ISM, leading to conclusion that the observed CO brightness is probably enhanced considerably by comic-ray heating in M83, thus a lower conversion factor X should be favored in this case.

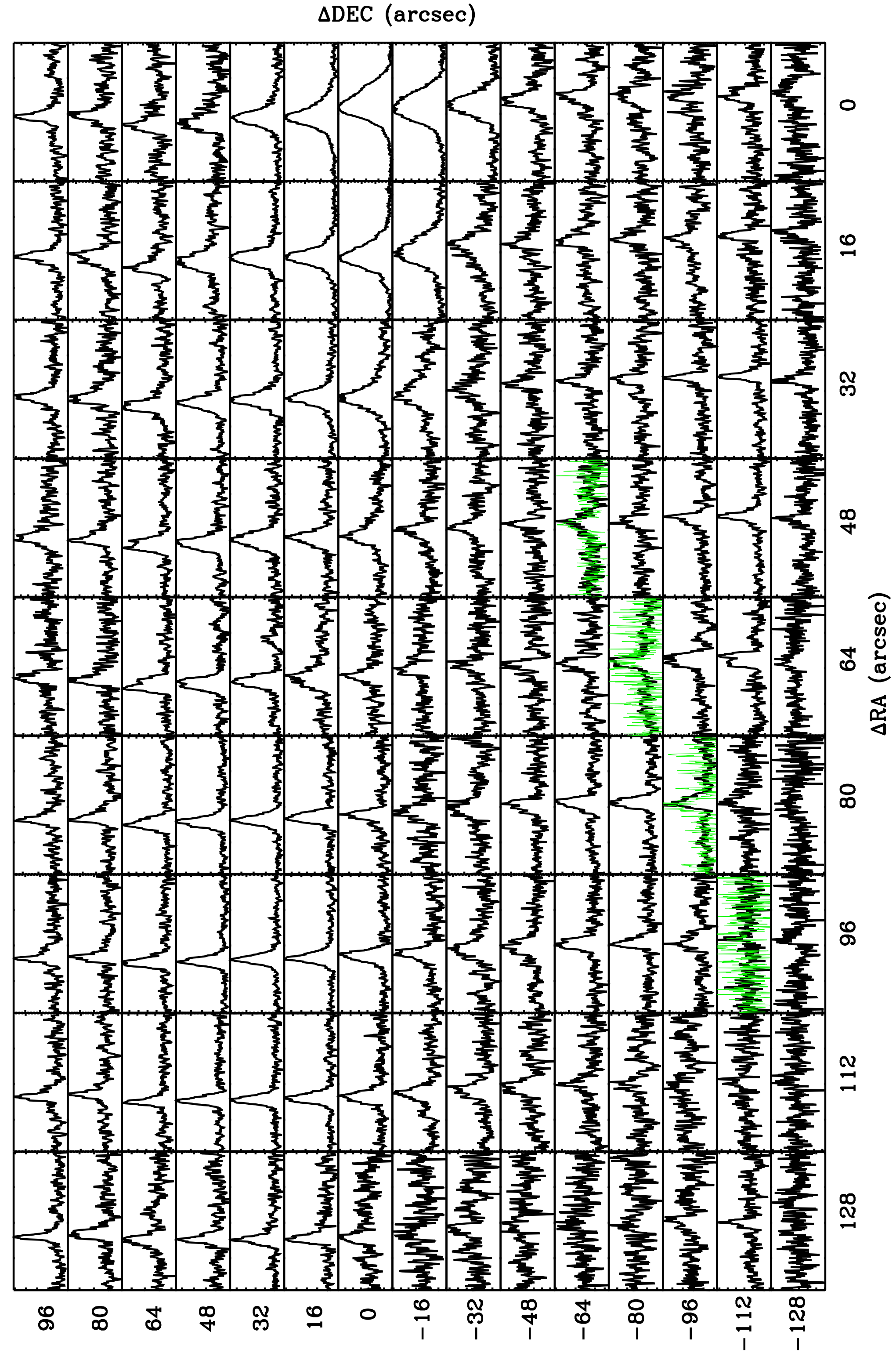

Figure C.1 Observed ^{12}CO$\,(\mathrm{J}=2-1)$ spectra within $\mathrm{V_{LSR}}$ range of 310∼700 $\mathrm{km\,s^{-1}}$ with ^{12}CO$\,(\mathrm{J}=3-2)$ spectra overplotted (green) at four positions. All spectra are normalized to unity height.

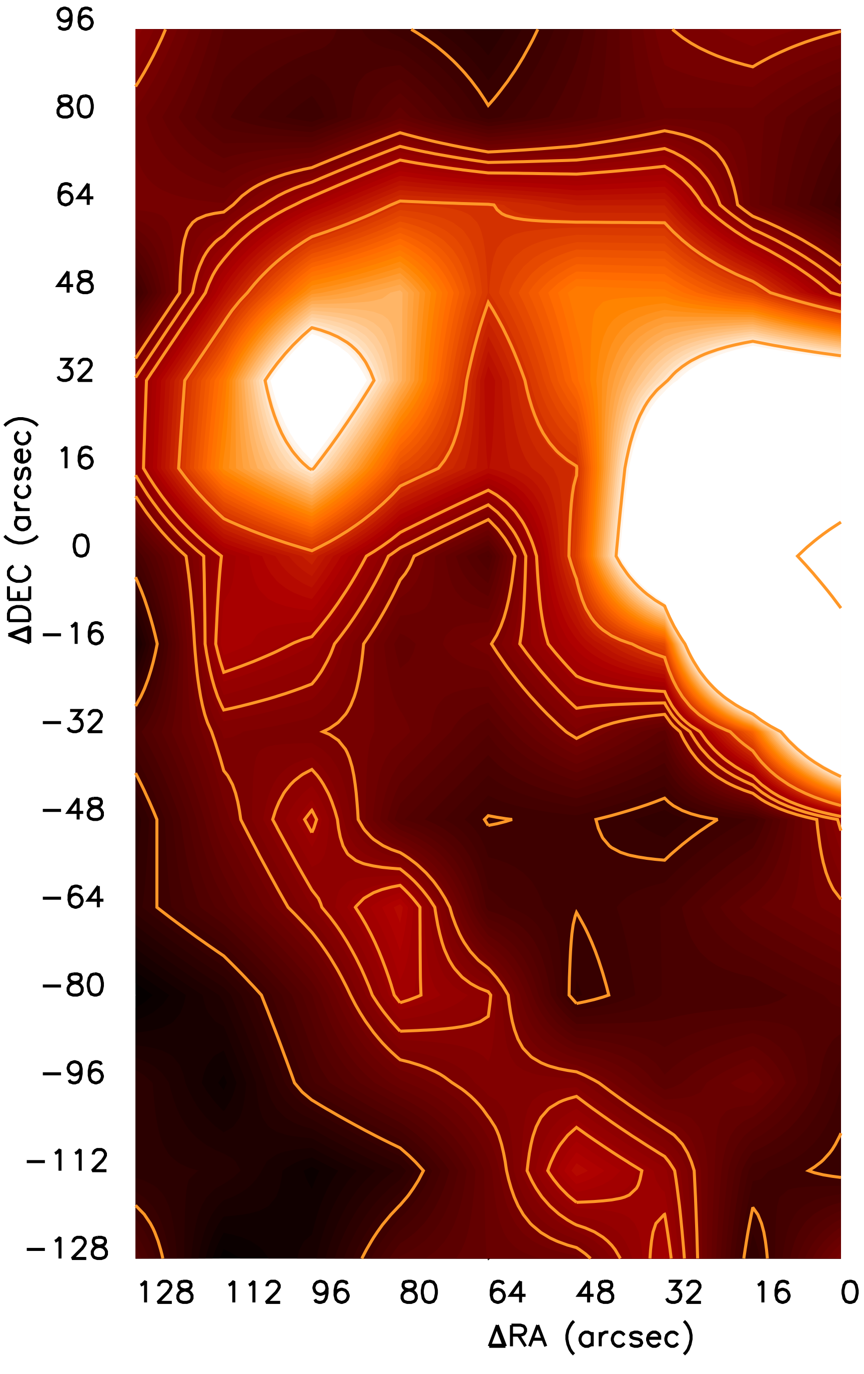

Figure C.2 Contourmap of the ^{12}CO $(\mathrm{J}=2-1)$ integrate flux detected in M83. The plotted contour levels are 3.5, 7.0, 8.0, 9.0, 12, 20 and 100 K kms^{-1} ; 1σ noise level is 1.1 K kms^{-1} .

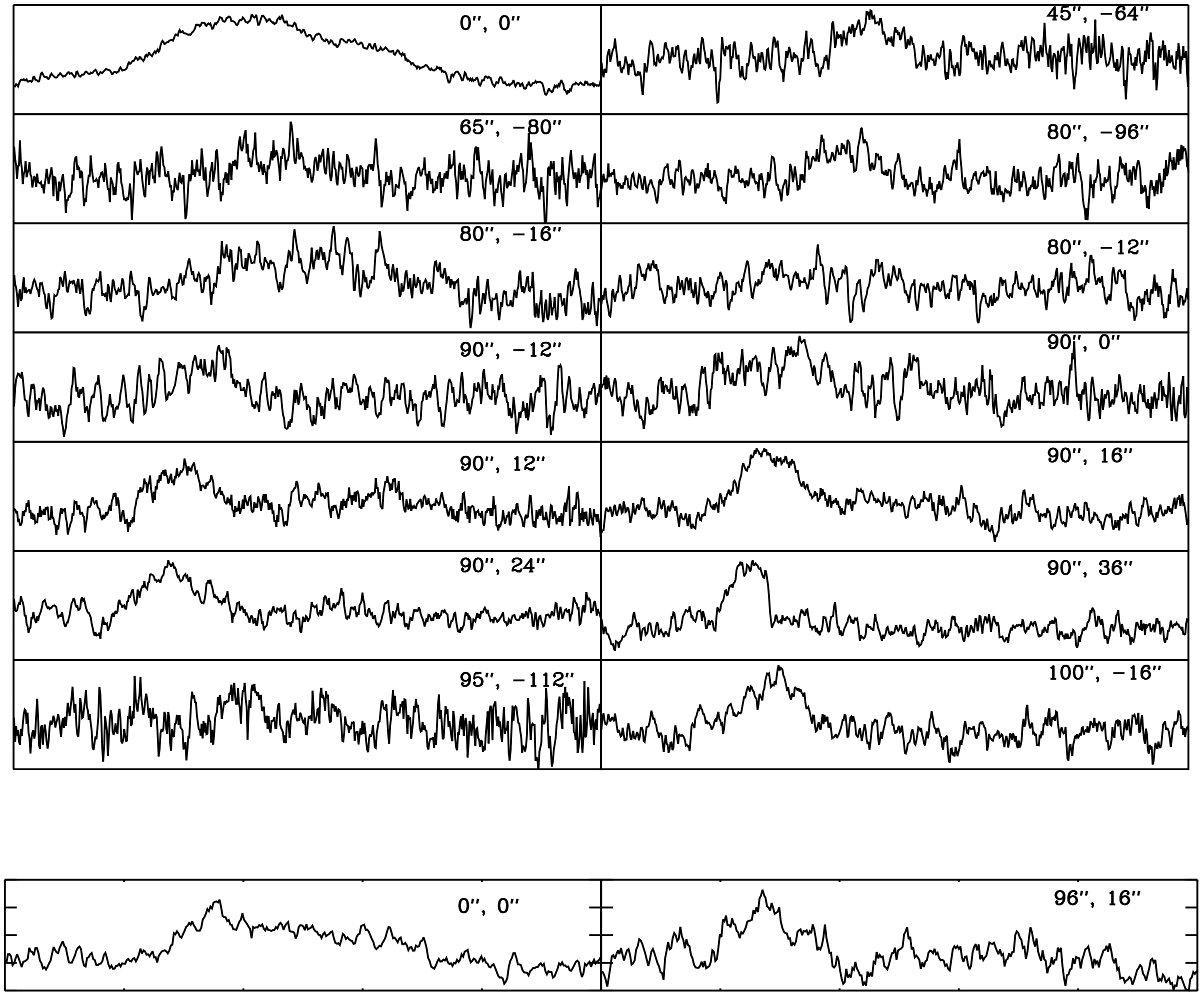

Figure C.3 Observed ^{12}CO (J = 3 − 2) and ^{13}CO (J = 2 − 1) spectra within V_{LSR} range of 420∼620 $km\,s^{-1}$. All spectra are normalized to unity height.

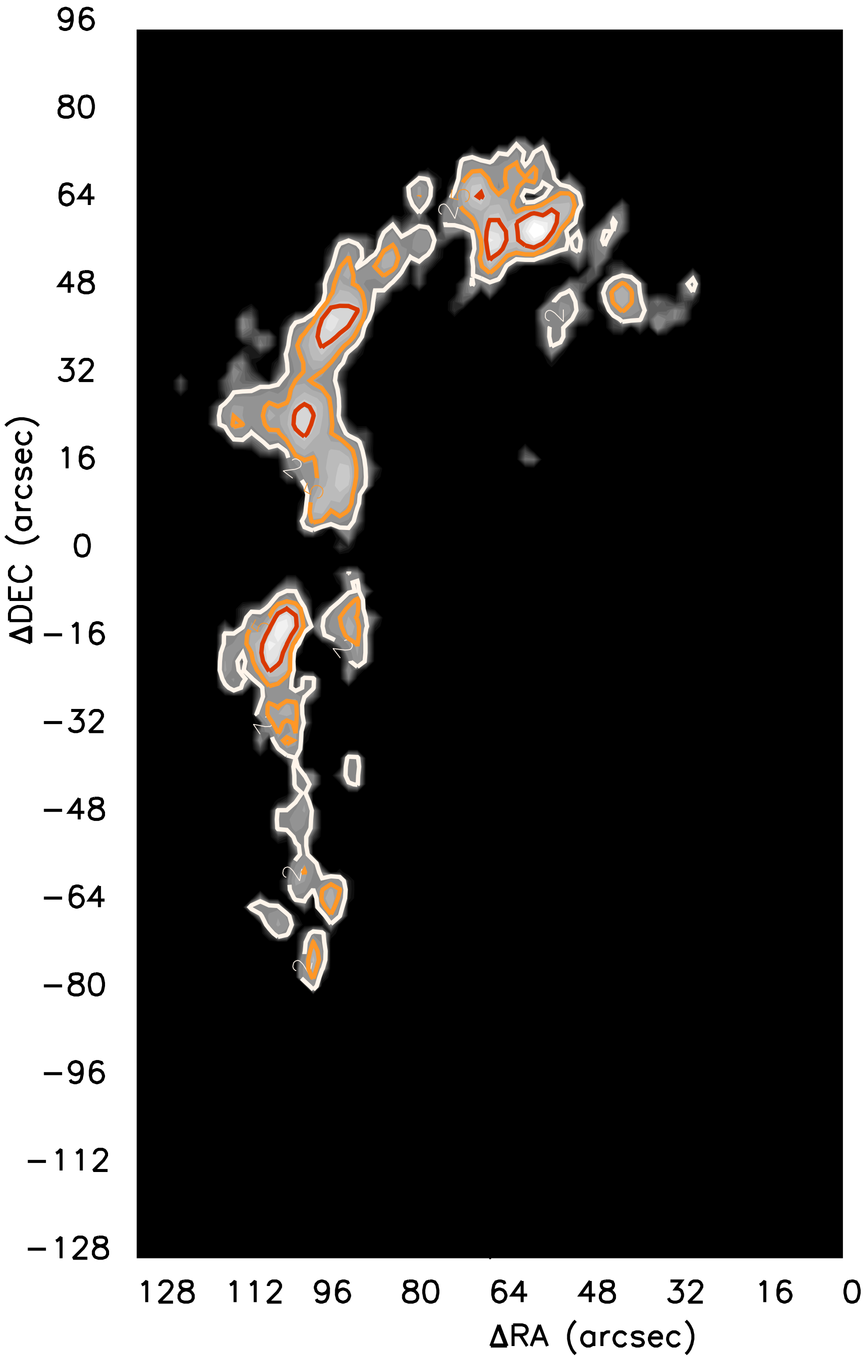

Figure C.4 Contour plot of the fraction of single-dish CO flux recovered by interferometric observations. The plotted contour levels are 2%, 5% and 10%.

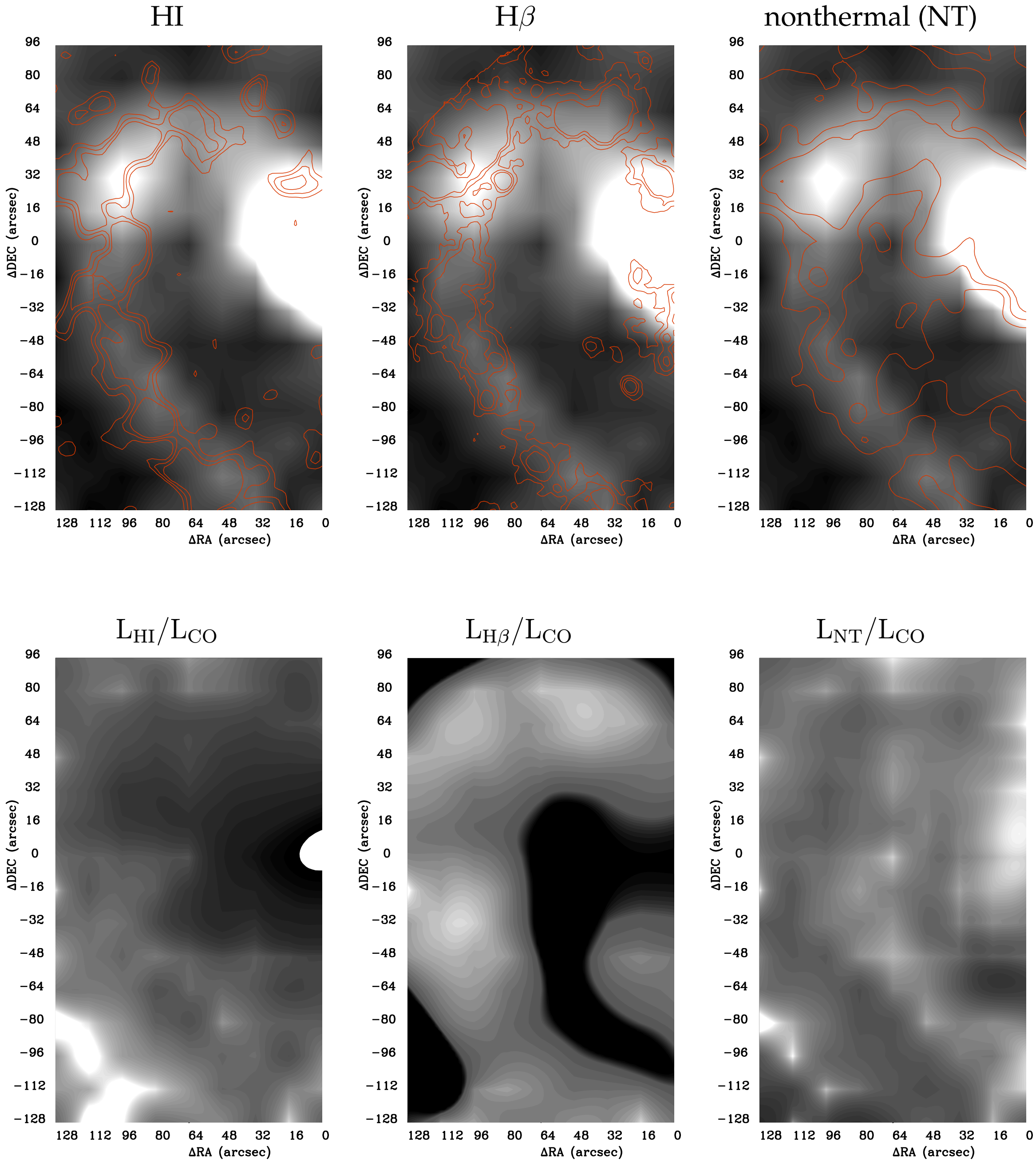

Figure C.5 Top panel: contours of HI, Hβ , and nonthermal (NT) radio continuum emission superimposed on ^{12}CO $(J = 2 - 1)$ map; bottom panel: flux ratios L_{HI}/L_{CO}, $L_{H\beta}/L_{CO}$ and L_{NT}/L_{CO}.

Table C.2. ^{12}CO $(\mathrm{J} = 2 - 1)$ observations of M83

ΔRA , ΔDec ″ ,″	$\mathrm{F}^{*}_{\mathrm{int}}$ ^{a} K kms^{-1}	$\mathrm{V}_{1\mathrm{st}}$ ^{b} km s^{-1}	FWHM km s^{-1}	$\mathrm{T}^{*}_{\mathrm{peak}}$ K	r.m.s. K
0, -128	5.0686	560.05	54.210	0.11	0.045
0, -112	2.1782	556.32	30.040	0.08	0.012
0, -96	1.9821	558.18	29.359	0.08	0.018
0, -80	3.3854	555.10	36.141	0.09	0.023
0, -64	4.0188	551.73	32.897	0.13	0.020
0, -48	5.5038	542.78	42.811	0.12	0.020
0, -32	23.855	530.13	66.742	0.33	0.021
0, -16	62.566	524.06	90.524	0.63	0.019
0, 0	85.965	506.31	101.06	0.86	0.013
0, 16	51.537	497.51	83.376	0.75	0.021
0, 32	17.129	495.50	56.824	0.34	0.018
0, 48	6.0815	488.33	52.966	0.14	0.020
0, 64	3.3761	471.06	28.590	0.12	0.019
0, 80	3.4601	472.48	33.026	0.12	0.018
0, 96	5.0080	471.68	28.698	0.18	0.020
16, -128	3.4855	550.43	27.249	0.15	0.042
16, -112	2.2815	550.72	18.609	0.10	0.019
16, -96	3.1005	542.10	43.389	0.11	0.021
16, -80	3.5211	543.79	41.281	0.11	0.020
16, -64	2.7973	536.81	23.758	0.10	0.020
16, -48	3.3176	534.24	30.763	0.11	0.021
16, -32	9.4158	513.21	68.328	0.16	0.023
16, -16	30.117	506.62	82.416	0.38	0.019
16, 0	58.171	492.10	85.506	0.74	0.018
16, 16	38.575	490.43	65.440	0.67	0.018
16, 32	18.830	488.75	49.824	0.39	0.021
16, 48	8.7960	479.07	42.290	0.18	0.023
16, 64	4.6518	465.54	36.179	0.17	0.020

Table C.2 (cont'd)

ΔRA , ΔDec ″ ,″	$F^{*}_{\rm int}$ [a] K kms^{-1}	$V_{\rm 1st}$ [b] km s^{-1}	FWHM km s^{-1}	$T^{*}_{\rm peak}$ K	r.m.s. K
16, 80	4.2898	464.35	37.925	0.12	0.016
16, 96	5.9493	464.29	36.225	0.19	0.016
32, -128	6.7715	537.06	25.203	0.30	0.049
32, -112	5.6982	546.00	25.518	0.24	0.021
32, -96	3.4905	538.52	23.736	0.16	0.020
32, -80	2.4871	535.88	22.111	0.11	0.020
32, -64	2.7856	534.79	33.630	0.11	0.017
32, -48	2.2691	527.98	26.670	0.10	0.019
32, -32	3.7249	508.07	53.887	0.10	0.021
32, -16	8.5290	499.42	66.380	0.14	0.019
32, 0	20.826	489.67	80.517	0.30	0.020
32, 16	18.692	482.72	57.553	0.40	0.020
32, 32	14.591	479.12	43.910	0.32	0.019
32, 48	11.518	471.88	44.990	0.28	0.022
32, 64	8.1581	464.34	52.696	0.18	0.018
32, 80	4.3080	460.50	44.299	0.11	0.017
32, 96	4.8521	459.25	33.643	0.16	0.017
48, -128	3.8103	531.46	24.234	0.19	0.046
48, -112	7.6017	539.33	32.514	0.28	0.021
48, -96	5.2356	532.84	31.131	0.22	0.022
48, -80	2.2029	528.90	29.799	0.10	0.017
48, -64	2.4693	522.54	41.948	0.09	0.018
48, -48	2.5092	512.25	35.658	0.12	0.021
48, -32	2.8493	506.48	41.592	0.13	0.024
48, -16	5.8328	487.38	39.945	0.18	0.027
48, 0	8.9615	491.21	59.646	0.19	0.018
48, 16	8.4985	478.46	36.224	0.24	0.019
48, 32	10.178	474.30	41.681	0.23	0.020

Table C.2 (cont'd)

ΔRA , ΔDec ″ ,″	$F^*_{\rm int}$ [a] K kms^{-1}	$V_{\rm 1st}$ [b] km s^{-1}	FWHM km s^{-1}	$T^*_{\rm peak}$ K	r.m.s. K
48, 48	10.313	464.29	36.042	0.26	0.021
48, 64	7.9351	460.60	33.750	0.24	0.018
48, 80	3.9759	456.23	38.192	0.14	0.016
48, 96	3.2680	455.01	35.895	0.10	0.017
64, -128	3.1134	523.73	30.486	0.15	0.047
64, -112	3.6035	526.98	30.443	0.11	0.013
64, -96	5.1506	527.02	30.542	0.14	0.020
64, -80	4.5215	521.22	28.213	0.15	0.020
64, -64	2.7070	515.62	26.241	0.10	0.018
64, -48	2.2709	508.97	28.914	0.08	0.018
64, -32	2.5698	504.19	28.809	0.09	0.020
64, -16	3.5707	492.47	25.768	0.13	0.026
64, 0	3.5827	481.45	29.182	0.14	0.019
64, 16	6.8229	475.30	43.052	0.17	0.018
64, 32	7.0738	464.35	32.135	0.20	0.019
64, 48	8.7945	458.97	31.426	0.24	0.022
64, 64	7.9452	455.36	32.162	0.25	0.019
64, 80	2.7250	448.92	30.573	0.09	0.014
64, 96	2.0698	450.57	23.695	0.08	0.015
80, -128	3.9126	515.97	59.102	0.08	0.042
80, -112	1.7418	522.71	34.937	0.05	0.018
80, -96	4.1599	517.77	27.194	0.15	0.018
80, -80	6.1855	515.12	26.667	0.21	0.019
80, -64	5.8533	513.47	29.486	0.18	0.021
80, -48	3.4774	506.64	27.036	0.14	0.017
80, -32	4.1860	489.26	38.638	0.11	0.022
80, -16	3.6080	479.27	34.019	0.11	0.027
80, 0	5.3941	474.94	36.053	0.18	0.017

Table C.2 (cont'd)

ΔRA , ΔDec $''$, $''$	$F^{*}_{\rm int}$ [a] $\rm K\,kms^{-1}$	$V_{\rm 1st}$ [b] $\rm km\,s^{-1}$	FWHM $\rm km\,s^{-1}$	$T^{*}_{\rm peak}$ K	r.m.s. K
80, 16	9.4133	472.14	30.309	0.29	0.019
80, 32	11.863	465.11	31.181	0.39	0.018
80, 48	11.965	460.52	30.400	0.38	0.021
80, 64	8.9856	454.71	32.208	0.28	0.018
80, 80	4.4187	450.35	36.507	0.15	0.017
80, 96	2.9625	443.70	27.142	0.12	0.016
96, -128	1.4508	519.29	21.514	0.09	0.039
96, -112	0.5699	512.63	16.328	0.04	0.017
96, -96	2.9015	514.11	38.817	0.11	0.016
96, -80	4.1953	511.36	26.943	0.16	0.018
96, -64	5.5626	508.09	40.878	0.14	0.017
96, -48	6.0796	496.42	51.808	0.14	0.019
96, -32	5.1056	495.66	52.834	0.09	0.021
96, -16	6.2663	477.78	38.318	0.16	0.022
96, 0	8.7005	472.86	30.995	0.27	0.017
96, 16	14.312	468.73	34.100	0.47	0.021
96, 32	17.564	464.23	31.703	0.62	0.027
96, 48	11.598	458.60	27.945	0.43	0.020
96, 64	6.8907	455.79	26.974	0.24	0.019
96, 80	3.1767	447.43	28.080	0.14	0.016
96, 96	3.6318	446.97	35.399	0.14	0.016
112, -128	2.1592	509.44	26.652	0.13	0.048
112, -112	0.8028	509.03	26.108	0.06	0.019
112, -96	1.3366	503.79	38.237	0.04	0.017
112, -80	1.8027	498.79	34.977	0.06	0.019
112, -64	2.9073	504.99	33.111	0.11	0.021
112, -48	3.7583	494.30	33.986	0.10	0.022
112, -32	4.7495	483.22	39.455	0.14	0.017

Table C.2 (cont'd)

ΔRA , ΔDec $'' , ''$	$F^*_{\rm int}$ [a] K kms^{-1}	$V_{\rm 1st}$ [b] km s^{-1}	FWHM km s^{-1}	$T^*_{\rm peak}$ K	r.m.s. K
112, -16	7.4380	466.56	59.868	0.17	0.021
112, 0	6.8494	467.18	34.689	0.20	0.017
112, 16	11.114	463.37	28.434	0.36	0.020
112, 32	10.740	458.41	26.937	0.38	0.022
112, 48	6.8180	456.41	21.142	0.29	0.020
112, 64	4.6736	454.13	22.032	0.23	0.019
112, 80	3.6835	449.65	32.104	0.15	0.018
112, 96	3.9389	438.82	42.042	0.14	0.014
128, -128	0.8832	515.28	25.040	0.11	0.055
128, -112	1.2909	501.16	19.011	0.07	0.014
128, -96	1.3978	503.93	29.864	0.05	0.016
128, -80	0.8825	499.31	29.751	0.05	0.018
128, -64	1.2156	499.91	27.702	0.05	0.018
128, -48	1.4405	498.32	32.201	0.05	0.019
128, -32	1.7032	483.41	24.718	0.07	0.022
128, -16	1.7642	475.54	31.121	0.08	0.025
128, 0	2.0720	460.27	22.922	0.08	0.019
128, 16	5.4240	460.17	26.518	0.21	0.021
128, 32	5.6353	456.43	28.671	0.24	0.018
128, 48	3.8010	455.71	23.831	0.17	0.022
128, 64	4.0027	452.70	27.883	0.14	0.020
128, 80	4.1057	447.56	28.002	0.14	0.018
128, 96	4.8075	437.92	34.157	0.21	0.018

[a] $F^*_{\rm int} = \sum T^*_i \Delta v$.

[b] $V_{\rm 1st} = \frac{\sum T^*_i \cdot V_i}{\sum T^*_i}$.

Note. — T^*_i and $T^*_{\rm peak}$ are not corrected for the main beam efficiency of $\eta_{\rm mb}$ = 0.7.

Table C.3. ^{12}CO $(J = 3 - 2)$ observations of M83

ΔRA , ΔDec ″ ,″	F^*_{int} [a] K kms^{-1}	V_{1st} [b] km s^{-1}	FWHM km s^{-1}	T^*_{peak} K	r.m.s. K
0, 0	132.63	505.39	102.78	1.3	0.060
48, -64	1.7729	520.94	22.909	0.08	0.025
64, -80	4.8649	521.14	37.85	0.15	0.063
79, -12	3.0134	488.88	44.372	0.13	0.056
80, -96	4.0398	510.85	23.608	0.19	0.050
80, -16	4.1753	494.72	42.880	0.15	0.058
91, -12	5.6942	477.85	39.233	0.23	0.062
91, 0	6.9116	472.68	35.926	0.24	0.065
91, 12	10.376	470.96	24.418	0.37	0.087
91, 16	10.594	472.51	27.589	0.32	0.048
91, 24	11.991	468.39	25.964	0.47	0.078
91, 36	13.799	462.09	13.662	0.85	0.097
96, -112	1.8044	512.75	38.119	0.07	0.035
101, -14	9.3953	471.07	32.051	0.36	0.056

[a] $F^*_{int} = \sum T^*_i \Delta v$.

[b] $V_{1st} = \frac{\sum T^*_i \cdot V_i}{\sum T^*_i}$.

Note. — T^*_i and T^*_{peak} are not corrected for the main beam efficiency of η_{mb} = 0.7.

Table C.4. ^{13}CO $(\mathrm{J}=2-1)$ observations of M83

ΔRA , ΔDec ″ ,″	$\mathrm{F}^{*}_{\mathrm{int}}$ [a] $\mathrm{K\,kms^{-1}}$	$\mathrm{V_{1st}}$ [b] $\mathrm{km\,s^{-1}}$	FWHM $\mathrm{km\,s^{-1}}$	$\mathrm{T}^{*}_{\mathrm{peak}}$ K	r.m.s. K
0, 0	6.4313	513.44	72.00	0.115	0.013
96, 16	1.2616	469.17	28.49	0.053	0.009

[a] $\mathrm{F}^{*}_{\mathrm{int}}=\sum \mathrm{T}^{*}_{\mathrm{i}}\Delta \mathrm{v}$.

[b] $\mathrm{V_{1st}}=\frac{\sum \mathrm{T}^{*}_{\mathrm{i}}\cdot \mathrm{V_i}}{\sum \mathrm{T}^{*}_{\mathrm{i}}}$.

Note. — $\mathrm{T}^{*}_{\mathrm{i}}$ and $\mathrm{T}^{*}_{\mathrm{peak}}$ are not corrected for the main beam efficiency of η_{mb} = 0.7.

Bibliography

Aannestad P., 1975, ApJ, 200, 30

Agladze N., Sievers A., Jones S., Burlitch J., Beckwith S., 1996, ApJ, 462, 1026

Andriesse C., 1974, A&A, 37, 257

Becker R., White R., Helfand D., 1995, ApJ, 450, 559

Blain A., Barnard V., Chapman S., 2003, MNRAS, 338, 733

Blain A., Chapman S., Smail I., Ivison R., 2004, ApJ, 611, 52

Blake G., Mundy L., Carlstrom J., Padin S., Scott S., Scoville N., Woody D., 1996, ApJ, 472, L49

Bohren C., Huffman D., 1983, *Absorption and Scattering of Light by Small Particles*

Calzetti D., 2001, PASP, 113, 1449

Chapman S., Blain A., Ivison R., Smail I., 2003, Nature, 422, 695

Chapman S., Smail I., Windhorst R., Muxlow T., Ivison R., 2004, ApJ, 611, 732

Chapman S., Smail I., Blain A., Ivison R., 2004, ApJ, 614, 671

Condon J., 1992, ARA&A, 30, 575

Dowell C., Allen C., Babu R., Freund M., Gardner M., Groseth J., Jhabvala M., Kovács A., Lis D., Moseley S., Phillips T., Silverberg R., Voellmer G., Yoshida H., 2003, SPIE, 4855, 73

Draine B., 2002, *The Cold Universe, Astrophysics of Dust in Cold Clouds*

Dunne L., Eales S., Edmunds M., Ivison R., Alexander P., Clements D., 2000, MNRAS, 315, 115

Dupac X., Bernard J., Boudet N., Giard M., Lamarre J., Mény C., Pajot F., Ristorcelli I., Serra G., Stepnik B., Torre J., 2003, A&A, 404, L11

Egami E., Dole H., Huang J., Prez-Gonzalez P., Le Floc'h E., Papovich C., Barmby P., Ivison R., Serjeant S., Mortier A., and 17 coauthors, 2004, ApJS, 154, 130

Farrah D., Serjeant S., Efstathiou A., Rowan-Robinson M., Verma A., 2002, MNRAS, 335, 1163

Fitzpatrick E., 1986, AJ, 92, 1068

Genzel R., Lutz D., Sturm E., Egami E., Kunze D., Moorwood A., Rigopoulou D., Spoon H., Sternberg A., Tacconi-Garman L., Tacconi L., Thatte N., 1998, ApJ, 498, 579

Genzel R., Lutz D., Moorwood A., Rigopoulou D., Spoon H., Sternberg A., Sturm E., Tran D., 2000, LNP, 548, 199

Greenberg J., 1971, A&A, 12, 240

Greenberg J., 1978, in McDonnell J. (ed.), *Cosmic Dust*

Greve T., Bertoldi F., Smail I., Neri R., Chapman S., Blain A., Ivison R., Genzel R., Omont A., Cox P., Tacconi L., Kneib J., 2005, MNRAS, 359, 1165

Hauser M., Arendt R., Kelsall T., Dwek E., Odegard N., Weiland J., Freudenreich H., Reach W., Silverberg R., and 9 coauthors, 1998, ApJ, 508, 25

Helou G., Soifer B., Rowan-Robinson M., 1985, ApJ, 298, L7

Hogg D., 1999, astro-ph/9905116

Hogg D., Baldry I., Blanton M., Eisenstein D., 2002, astro-ph/0210394

Hildebrand R., 1983, QJRAS, 24, 267

Kennicutt R., 1998, ARA&A, 36, 189

Kittel C., 1976, *Introduction to Solid State Physics*

Knapp G., Sandell G., Robson E., 1993, ApJS, 88, 173

Kovács A., Chapman S., Dowell C., Blain A., Ivison R., Smail I., Phillips T., 2006, astro-ph/0604591

Kovács A., 2006, Caltech Ph.D. Theses

Leong M., Houde M., Peng R., Yoshida H., Chamberlin R., Phillips T., 2003, AMOS Conference

Li A., Draine B., 2001, ApJ, 554, 778

Lis D., Serabyn E., Keene J., Dowell C., Benford D., Phillips T., Hunter T., Wang N., 1998, ApJ, 509, 299

Martin P., 1978, *Cosmic Dust*

Mennella V., Brucato J., Colangeli L., Palumbo P., Rotundi A., Bussoletti E., 1998, ApJ, 496, 1058

Mie G., 1908, Ann. Phys., 25, 377

Mitra S., 1969, in Nudelman S., Mitra S. (eds.), *Optical properties of solids*

Moshir M., Kopman G., Conrow T., 1992, *IRAS Faint Source Survey, Explanatory supplement version 2*

Phillips W., 1987, RPPh, 50, 1657

Puget J., Abergel A., Bernard J., Boulanger F., Burton W., Desert F., Hartmann D., 1996, A&A,308, L5

Sanders D., Mirabel I., 1996, ARA&A, 34, 749

Schwartz P., 1982, ApJ, 252, 589?1983?

Schmidt M., 1959, ApJ, 129, 243

Schlömann E., 1964, PhRvA, 135, 413

Scoville N., Kwan J., 1976, ApJ, 206, 718

Seaton M., 1979, MNRAS, 187, 73

Seki J., Yamamoto T., 1980, Ap&SS, 72, 79

Sellgren K., Allamandola L., Bregman J., Werner M., Wooden D., 1985, ApJ, 299, 416

Soifer B., Sanders D., Neugebauer G., Danielson G., Lonsdale C., Madore B., Persson S., 1986, ApJ, 303, L41

Soifer B., Sanders D., Madore B., Neugebauer G., Danielson G., Elias J., Lonsdale C., Rice W., 1987, ApJ, 320, 238

Soifer B., Neugebauer G., 1991, AJ, 101, 354

Stanford S., Stern D., van Breugel W., De Breuck C., 2000, ApJS, 131, 185

Steidel C., Giavalisco M., Pettini M., Dickinson M., Adelberger K., 1996, ApJ, 462, L17

Tielens, Allamandola, 1987

Trumpler R., 1930, PASP, 42, 214

Verma A., Rowan-Robinson M., McMahon R., Efstathiou A, 2002, MNRAS, 335, 574

Yun M., Reddy N., Condon J., 2001, ApJ, 554, 803

Wynn-William C., Becklin E., 1993, ApJ, 412, 535

Wright E., 1987, ApJ, 320, 818

Young J., Scoville N., 1991, ARA&A, 29, 581

Comte G., 1981, A&A, 44, 441

Cowan J., Roberts D., Branch D., 1994, ApJ, 434, 128

Crosthwaite L., Turner J., Buchholz L., Ho P., Martin R., 2002, AJ, 123, 1892

de Vaucouleurs G., de Vaucouleurs A., Corwin H., Buta R., Paturel G., Fouque P., 1991, *Third Reference Catalogue of Bright Galaxies*

Deutsch E., Allen R., 1993, AJ, 106, 5

Kennicutt R., 1988, ApJ, 334, 144

Lord S., Kenney J., 1991, ApJ, 381, 130

Rand R., Lord S., Higdon J., 1999, ApJ, 513, 720

Scoville N., Yun M., Sanders D., Clemens D., Waller W., 1987, ApJS, 63, 821

Solomon P., Rivolo A., Barrett J., Yahil A., 1987, ApJ, 319, 730

Talbot R., Jensen E., Dufour, R., 1979, ApJ, 229, 91

Tilanus R., Allen R., 1993, A&A, 274, 707

Turner J., Martin R., Ho P., 1990, ApJ, 351, 418

Vogel S., Boulanger F., Ball R., 1987, ApJ, 321, L145

Wilson C., Scoville N., 1990, ApJ, 363, 435

Wilson C., Reid I., 1990, BAAS, 22, 1329